One-dimensional zinc oxide nanostructures and devices

Yang, Yi

2008

Yang, Y. (2008). One-dimensional zinc oxide nanostructures and devices. Doctoral thesis, Nanyang Technological University, Singapore.

https://hdl.handle.net/10356/41804

https://doi.org/10.32657/10356/41804

ONE-DIMENSIONAL ZINC OXIDE NANOSTRUCTURES AND DEVICES

YANG YI

School of Electrical & Electronic Engineering

A thesis submitted to the Nanyang Technological University
in fulfillment of the requirement for the degree of
Doctor of Philosophy

2008

To my beloved parents and

grandfather

ACKNOWLEDGEMENTS

I would like to take this opportunity to express my deepest and special gratitude to my supervisor Prof. Tay Beng Kang, who offered me this opportunity to pursue my PhD degree, and my co-supervisor Prof. Sun Xiaowei, who was also my supervisor on Undergraduate Research Opportunity Program (UROP, 2003) and Final Year Project (FYP, 2004). I really appreciate their invaluable efforts, endless patience and kind encouragement in guiding me to be a real researcher throughout the past three years. Their enthusiasm, willingness, commitment, and determination to research inspired me. I also learn from them the disciplines in research, self-management, and leadership, which will benefit my whole life.

I would also like to express my sincere thanks to Dr. Wang Jianxiong from the bottom of my heart, for his enthusiasm, encouragement, patience and guidance in both of my experimental and theoretical explorations, and for his critical and invaluable advices.

I would like to express my sincere thanks to Prof. Dong Zhili, Prof. Tim White, Dr. Cristiano Ferraris, and Ms. Guo Jun, School of Materials Engineering, for teaching and supporting me in the field-emission scanning electron microscopy and transmission electron microscopy characterizations.

I am also grateful to Dr. Zhang Xinhai, Institute of Materials Research and Engineering, for the low-temperature photoluminescence measurements and discussions.

Table of Contents

LIST OF FIGURES

LIST OF TABLES

SUMMARY

As a multifunctional oxide semiconductor, ZnO has attracted substantial interest for a wide range of applications, including transparent conductors, UV light-emitting diodes (LEDs) and laser diodes, chemical and biochemical sensing, field emitting devices, dye-sentitized solar cells and host for diluted magnetic semiconductor. On the other hand, nanostructures made of various materials including ZnO, such as nanowires (NWs), nanobelts, nanoribbons, etc, are an emerging class of one-dimensional and quasi-one-dimensional materials that have been extensively studied as fundamental building blocks for nano-scale science and technology in the last period. This thesis focuses on the fabrication of various high quality crystalline ZnO nanostructures by using the vapor-phase transport (VPT) method and their subsequent characterizations. The emphasis is devoted to the enhancement of photoluminescence properties by plasma immersion ion implantation (PIII) surface modification, the application of ZnO NWs as templates for growth of other oxide materials, and applications in *p-n* homojunction LEDs.

Two new morphologies, microraft with diamond-shaped cross section and resistor-shaped NW composed of a pair of crystallites, have been successfully fabricated by VPT method from ZnO and graphite powder at atmosphere pressure. Although the growth conditions are similar for both morphologies, by varying the partial pressure of the growth species and the amount of Cu and water during growth, the end products are totally different. The experimental details, characterization and analysis results of the microraft

and resistor-shaped NWs are presented in Chapters 3 and 4, respectively. Growth mechanisms have been proposed to explain the formation of these two morphologies.

Controlled synthesis and repeatability are important in nanostructure fabrication. We have achieved the controlled synthesis of nanocombs (NCBs), random nanowires (RNWs) and aligned nanowires (ANWs) by varying the oxygen partial pressure, as is presented in detail in Chapters 5 to 8. However, due to the large surface-to-volume ratio, the defect luminescence becomes dominant as size reduces. In Chapter 5 and 6, we shall demonstrate UV photoluminescence enhancement by PIII surface modification. By implanting Ti/Ni ions into the shallow surface of the nanostructure, the recombination of surface excitons (SXs) we observed at low temperature can be quenched and hence the UV emission is improved at room temperature (Chapter 5); the defect emission (or green emission) can be completely quenched as well (Chapter 6). The surface passivation by PIII has been discussed in both Chapters. We have also demonstrated that PIII can be a useful tool to directly probe the native surface defect depth in terms of the ion implantation depth, which is also closely related to the surface-sensitive properties (field emission, gas sensing etc.) and applications of metal oxides.

With the success in fabricating RNWs, Chapter 7 presents the application of single-crystalline ZnO NWs as a template to fabricate ternary Zn_2TiO_4 spinel NWs, through the solid-state reaction of Ti and ZnO from a ZnO/Ti core/shell structure. The fabrication consists of three steps: (1) fabricating ZnO NWs, (2) coating them with an amorphous layer of Ti by magnetron sputtering, and (3) thermal annealing at 800°. Detailed TEM investigations revealed the twinned structure of Zn_2TiO_4. The origin of the twinned structure of Zn_2TiO_4 spinel NWs is discussed.

With the success in fabrication ANWs, Chapter 8 presents the application of ZnO NWs in *p-n* homojunction LEDs. The *p-n* junctions were formed by As^+ ion implantation into the top layer of ANWs followed by thermal annealing. These As-doped single NW LEDs were probed using a nanomanipulator, and showed good rectification *I-V* characteristics. Strong electroluminescence in red region has been observed. Distinct EL emissions in red region were observed at room temperature under forward bias, where the emission intensity increases exponentially with injected current, suggesting high efficiency of these LEDs.

COMMON ABBREVIATIONS

1D	One dimensional
ANW	Aligned nanowire
CCD	Charge coupled device
EDX	Energy dispersive x-ray spectroscopy
EL	Electroluminescence
FESEM	Field emission scanning electron microscopy
FWHM	Full width at half maximum
FX	Free exciton
GB	Green band
HRTEM	High-resolution transmission electron microscopy
LED	Light-emitting diode
NBE	Near band-edge
NCB	Nanocomb
NR	Nanorod
NW	Nanowire
PIII	Plasma immersion ion implantation
PL	Photoluminescence
RNW	Random nanowire
RSNW	Resistor-shaped nanowire
SAED	Selected-area electron diffraction

Sccm	Standard cubic centimeter per minute
SEM	Scanning electron microscopy
SRIM	the stopping and ranges of ions in solids
SX	Surface exciton
TEM	Transmission electron microscopy
UV	Ultraviolet
VLS	Vapor liquid solid
VPT	Vapor-phase transport
VS	Vapor solid
XPS	X-ray photoelectron spectroscopy
XRD	X-ray diffraction

Chapter 1 INTRODUCTION

Nanotechnology refers broadly to a field of applied science and technology with a unified theme of control of matter and fabrication of devices at the nanometer scale. It is a highly multidisciplinary field, drawing from fields such as applied physics, materials science, colloidal science, device physics, supramolecular chemistry, and even mechanical and electrical engineering. Much speculation exists as to what new science, technology and application may result from researches in this direction.

A widely accepted definition of a nanostructure is a system in which at least one dimension is $\leq$ 100 nm.[1] Two-dimensional (2D) quantum wells, one-dimensional (1D) quantum wires, and zero-dimensional (0D) quantum dots are the typical structural forms. Quantum effects due to size confinement in nanostructures occur when the characteristic size of the object is comparable to the critical lengths (typically 1-10 nm) of the corresponding physical processes, such as the mean free path of electrons, the coherence length, or the screening length.

1.1 Study on 1D nanostructures

Nanoscale 1D and quasi-1D materials, such as wire, rods, belts, and tubes have stimulated great interest due to their importance in basic scientific research and potential technology applications.[2] It is generally accepted that 1D nanostructures provide a good system to investigate the dependence of electrical, thermal transport, and mechanical properties on dimensionality and size reduction (or quantum confinement). Many unique

and fascinating properties have been proposed and demonstrated for this class of materials, such as metal-insulator transition, superior mechanical roughness, higher luminescence efficiency, enhancement of thermoelectric figure of merit, lowered lasing threshold, size-dependent excitation or emission, quantized (or ballistic) conductance, Coulomb blockade (or single-electron tunneling, SET), etc.[3-6] 1D materials can also be used as both interconnects and functional units in fabricating electronic, optoelectronic, electrochemical, electromechanical, bioelectrical and photonic crystal devices.[2, 7-11] The field of nanomaterials and nanotechnology represents an exciting and rapidly expanding research area crossing the borders between the physical, chemical, life and engineering sciences.

1.2 Requirement for an ideal semiconductor nanostructure

The main requirements for an ideal semiconductor nanostructure are listed below. In practice the relative importance of these requirements will be dependent upon the precise application being considered:

Size: An ideal semiconductor nanostructure should have small size dispersion with at least one dimension ≤ 100 nm.

Optical and structural quality: Semiconductors produce light when an electron in the conduction band recombines with a hole in the valence band – a radiative process. However, electron-hole recombination may also occur without the emission of a photon in a non-radiative process. Such processes are enhanced by the presence of certain defects which form states within the band gap. If non-radiative processes become significant then the optical efficiency – the number of photons produced for each injected electron and

hole – decreases. For optical applications, nanostructures with low defect density are therefore required. Poor structural quality may also degrade the carrier mobility.

Uniformity: Typical devices contain a large number of nanostructures. Ideally each nanostructure should have the same shape, size, and composition.

Doping: Realization of stable, repeatable, reliable, and conductive *n*- and *p*-type doping is necessary for practical applications

Assembly: Following the "bottom-up" fabrication strategy, achieving the capability to manipulate single 1D nanostructures, as well as the ability of industrial-scale fabrication and assembly are important for practical applications.

1.3 Controlled Growth of 1D Nanostructures

An important issue in the study and application of 1D materials is how to assemble individual atoms into 1D nanostructures in an effective and controllable way. In comparison with quantum dots and wells, the advancement of 1D nanostructures has been slow until recently, as hindered by the difficulties associated with the synthesis and fabrication of these nanostructures with well-controlled dimensions, morphology, phase purity, chemical composition, and assembly of them. Various methods have been developed for making nanostructures. Generally, there are two philosophically distinct approaches for creating small objects, which can be categorized as top-down and bottom-up approaches. The biggest problem with top-down approaches, such as X-ray or extreme-UV lithography,[12] electron-beam (e-beam) or focused-ion-beam (FIB) writing,[13, 14] and proximal-probe patterning,[15, 16] is that these processes generally are slow and the cost is high. The bottom-up approach, in which functional electronic structures are

assembled from chemically synthesized, well-defined nanoscale building blocks, much like the way nature uses proteins and other macromolecules to construct complex biological systems, represents a powerful alternative approach to conventional top-down methods.[17, 18] The bottom-up approach has the potential to go far beyond the limits of top-down technology by defining key nanometer scale metrics through synthesis and subsequent assembly. They might provide an alternative and intriguing strategy for generating 1D in terms of material diversity, cost, throughput, and the potential for high-volume production.[19, 20]

The essence of 1D nanostructure formation by a bottom-up approach is crystallization, a process that has already been investigated for hundreds of years.[21, 22] Growth of a solid from a vapor, liquid, or solid phase involves two fundamental steps: *nucleation* and *growth*. As the concentration of the building blocks (atoms, ions, or molecules) of a solid becomes sufficiently high, they aggregate into small clusters (or nuclei) through homogeneous nucleation or heterogeneous nucleation when the surface is another material. With a continuous supply of the building blocks, these nuclei can serve as seeds for further growth to form larger structures. Although crystallization has been studied for a long time, very little is quantitatively known. Neither is it trivial to achieve a complete control over this process. It is generally accepted that the formation of a perfect crystal requires a reversible pathway between the building blocks on the solid surface and those in a fluid phase (i.e., vapor, solution, or melt).[21-23] This condition allows the building blocks to adopt correct positions in developing the long-range-ordered, crystalline lattice. In addition, the building blocks also need to be supplied at a well-controlled rate in order to obtain crystals having a homogenous composition and uniform morphology.[20] In the past several years, a variety of chemical and physical methods have been reexamined as

the "bottom-up" approach for generating anisotropic 1D growth.[7, 23] Two kinds of well-accepted spontaneous growth mechanisms through a gas-phase reaction have been involved: the vapor-solid (VS) and the vapor-liquid-solid (VLS) processes, respectively.

1.3.1 Some basics of vapor-phase crystal growth

Vapor-phase transport (VPT) is a widely available technique. It has been extensively used in the literature by a number of different groups to deposit a variety of nanostructure morphologies. In order to understand the growth mechanism which is critical in controlling and designing nanostructures, some basics of the vapor-phase growth mechanism are briefed in this section. The growth of a nanostructured crystal is affected by many factors, such as adsorption and desorption of the growth species onto and from the growing surface, surface diffusion of adsorbed growth species, irreversible surface growth in a system with high concentration growth species, and desorption of by-products.[23] The rate-limiting step is either adsorption-desorption of growth species on the surface or surface growth. In a growth system where the growth rate is limited by the adsorption and desorption of the growth species (i.e., the supersaturation or concentration of growth species is low), the growth rate is determined by the condensation rate J (atoms/cm^2 sec), which is given by:

$$J = \frac{\alpha \sigma P_0}{\sqrt{2\pi m k T}} \qquad (1.1)$$

where α is the accommodation coefficient, which is surface-specific property, $\sigma = (P-P_0)/P_0$ is the supersaturation of the growth species in the vapor in which P_0 is the equilibrium vapor pressure of the crystal at temperature T, and P is the partial vapor pressure, m is the

atomic weight of the growth species and k is the Boltzmann constant. The growth rate is directly proportional to P, α, and σ. A significant difference in α in different facets would result in anisotropic growth.

On the other hand, in a growth system where the growth rate is limited by the irreversible surface growth (i.e., the growth specie concentration is high), the growth rate becomes independent on the concentration of growth species. However, a high concentration or vapor pressure of growth species in the vapor phase would increase the probability of defect formation, such as impurity inclusions and stacking faults. It may also result in a secondary nucleation on the growth surface or even homogeneous nucleation,[23] which would effectively terminate the epitaxial or single crystal growth.

It should be noted that in order to realize anisotropic growth to obtain 1D nanostructures, a low supersaturation is required. Ideally, the concentration is higher than the equilibrium concentration (saturation) of the growth surface, but equal or lower than that of other non-growth surfaces. In comparison, a medium supersaturation supports bulk crystal growth, and a high supersaturation results in secondary or homogeneous nucleation leading to polycrystalline structure or powder formation.

1.3.2 Kinetics of anisotropic growth via VS growth mechanism

The VS process is also referred to as evaporation-condensation process, which is a catalyst- and template-free method. Chemical reactions among various precursors may be involved to produce desired materials. The driving force for the synthesis of nanowires (NWs) by spontaneous growth is a decrease in Gibbs free energy, which arises from either recrystallization or a decrease in supersaturation. Compared with solution methods and

thin film growth techniques, the NWs growth by VS methods are commonly single crystals with fewer imperfections. The formation of 1D nanostructures through the VS process is due to anisotropic growth, which results from several factors, such as the difference in growth rates of different crystal facets, presence of imperfections in specific crystal directions, and preferential accumulation of specific facets etc.[23]

The nucleation and growth of nanostructures by the VS process can be explained as follows. The vapor of growth species is firstly formed either by physical or chemical reaction of source materials. Nucleation of the growth species on substrate occurs due to supersaturation of the vapor in the gas phase. For condensation of the vapor phase species, the critical nuclei diameter, d_c, depends on the supersaturation by the relation[24]

$$d_c = \frac{4\sigma\,\Omega}{kTln(P/P_0)} \tag{1.2}$$

where σ is the interfacial or surface energy, Ω is the molar volume, T is the temperature of the substrate, P is the partial pressure of the growth species, and P_0 is the vapor pressure of the growth species at equilibrium. Both P and P_0 are functions of temperature. Therefore, as the temperature increased, the P/P_0, which is the supersaturation ratio (usually >1), remains constant, and the critical nuclei diameter is inversely proportional to the temperature.

We have shown in Equation (1.2), the diameter of the nanostructure is mainly determined by temperature; in addition, the site where growth species prefer to stay determines the shape of nanostructure. Briefly, the morphology of the nanostructure in VS process is controlled by the crystal growth kinetics. The probability of nuclei formation is given by[25]

$$P_N = B \exp\left(-\frac{\pi\sigma^2}{k^2 T^2 \ln(P/P_0)}\right) \tag{1.3}$$

where B is a constant, T is the growth temperature, and the rest of the parameters were defined previously at Equation (1.2). The surface energy is related to the crystal plane; a low-index crystal plane is of lower surface energy. According to Equation (1.3), the lower the surface energy, the larger the nucleation probability on the crystal faces. On the other hand, an atom adsorbed on a low-energy surface has low binding energy and a high probability of desorption. Competition and coordination of the two processes are responsible for the formation of the low-index crystal planes enclosing the nanostructure. The temperature and the supersaturation ratio are two parameters controlled by processing conditions. Lower temperature and lower supersaturation ratio promote the growth of wire-like structures. Therefore, in the VS method, the temperature and the supersaturation ratio are the two dominant processing factors in controlling the morphology of the products.

This method has been intensively studied to grow various 1D nanostructured material and most of the work have been done since 2000, such as metals (W,[26] Zn,[27] Sn,[28]), III-V semiconductors (AlN,[29-31] InN[32]), II-VI semiconductors (CdS[33], ZnS[34, 35]) IV semiconductors (SiC[36]), and metal oxides (ZnO,[37, 38] CuO,[39] SiO$_2$,[40] Fe$_2$O$_3$,[41] TiO$_2$,[42] In$_2$O$_3$[43]). However, this method is limited due to relatively high evaporation temperature needed.

1.3.3 VLS growth mechanism: catalyst-assisted growth

In the VLS growth, a second phase material, commonly referred to as either impurity or catalyst, is purposely introduced to direct and confine the crystal growth to a specific orientation and within a confined area. Wagner *et al.*[21] first proposed the VLS theory over 40 years ago to explain the experimental results and observations in the growth of Si micrometer-sized whiskers. The theory and models were further elaborated by Givargizov,[22] and recently reexamined by Lieber,[44] Yang,[20] Wang,[45] and many other research groups.[46] The VLS process has now become a widely used method for growing 1D nanostructures from a rich variety of inorganic materials that include elemental semiconductors (Si, Ge, and B),[44, 47, 48] III-V semiconductors (AlN,[49] GaN,[50, 51] InN,[52] GaP,[53, 54] GaAs,[54-56] InP,[54, 57] InAs[56, 58]), II-VI semiconductors (ZnS,[54, 59, 60] ZnSe,[54, 61] CdS,[54, 62] CdSe[54, 63]), and most of the oxides (ZnO,[64] Ge$_2$O$_3$,[65] In$_2$O$_3$,[65] SnO,[65-67] MgO,[68, 69] SiO$_2$,[70-72] Al$_2$O$_3$[73]). The NWs produced using the VLS approach are remarkably uniform in their diameter, which is usually of the order of tens or hundreds of nanometer and >1 μm in length.

Growth species diffuse and dissolve into a liquid droplet.

Vapor

Supersaturation

Nucleation

Liquid alloy droplet having a large surface accommodation coefficient.

Growth species precipitation at the substrate-liquid interface

Unidirectional axial growth
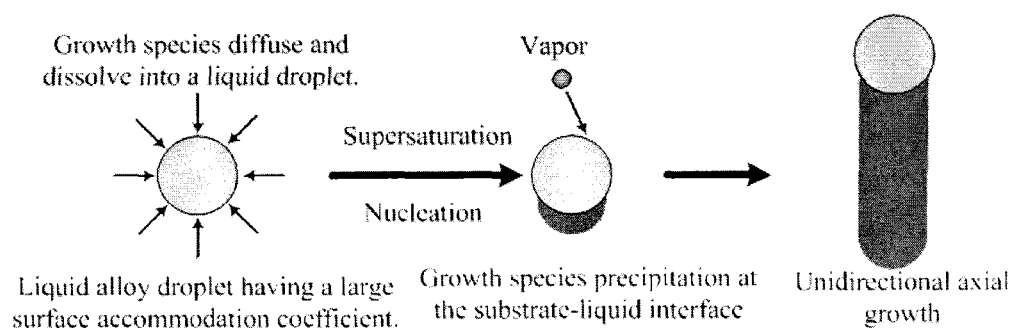
Figure 1.1 Schematic diagram showing the principle steps of the vapor-liquid-solid growth technique: (a) initial nucleation between vapor and catalyst (Au usually), (b) incorporation of growth species into crystal structures, (c) continuous anisotropic growth of crystal.[23]

In a typical VLS growth, the process can be simply described as sketched in Figure 1.1. The growth species are evaporated firstly, then they diffuse and dissolve into a liquid droplet. Ideally, the growth species and catalyst should be able to form eutectic compounds. The surface of the liquid has a large accommodation coefficient, and is therefore a preferred absorption site for incoming vapor reactants. Saturated growth species in the liquid droplet will diffuse to and precipitate at the interface between the substrate and the liquid. The precipitation will first follow nucleation and then crystal growth. Continued precipitation or growth will separate the substrate and the liquid droplet, resulting in the growth of NWs (See Figure 1.2).[7, 21, 23] The 1D growth is mainly induced and dictated by the liquid droplets, which is analogous to a catalyst in a chemical reaction; the sizes of the liquid droplets remain essentially unchanged during the entire process of wire growth. In this sense, each liquid droplet serves as a soft template to strictly limit the lateral growth of an individual wire, and thus the density and diameter of the wire could be controlled.
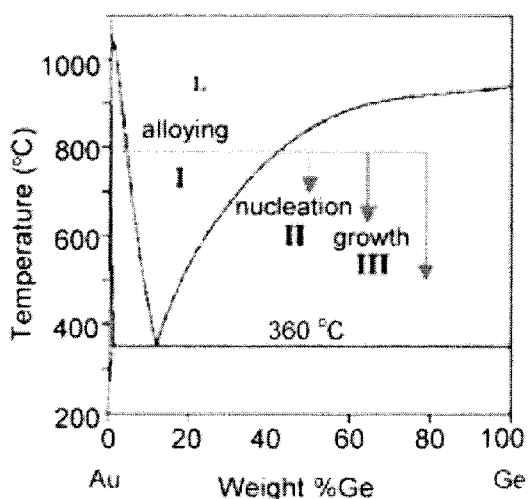
Figure 1.2 The compositional and phase evolution during the NW growth process.[20]

10
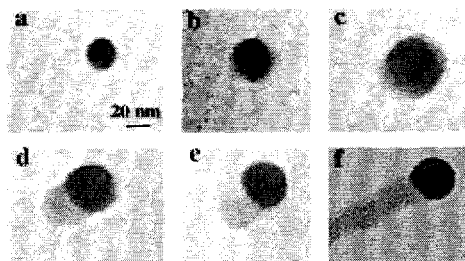
Figure 1.3 *In situ* TEM images recorded during the process of a Ge NW.[74]

Recently, real-time observation of Ge, Si, In$_2$Se$_3$,[74-76] etc., NW growth was conducted in high-resolution *in situ* transmission electron microscopy (TEM), identifying typical VLS growth processes. The *in situ* TEM images of a growing Ge NW with Au catalyst are shown in Figure 1.3. Figure 1.3 (a-c) shows the alloying process where the Ge and Au form an alloy and liquidity with increasing amount of Ge vapor condensation and dissolution. Figure 1.3 (d) and (e) show the nucleation occurs in a supersaturated alloy liquid. Figures 1.3 (d-f) show the axial growth of the Ge NW, where the incoming Ge species prefer to diffuse to and condense at the existing solid/liquid interface, and the existing interface will then be pushed forward to form a NW.

Although this growth model has been widely accepted, improvement is necessary to explain the experimental observations for some specific materials. Several accompanied growth models, such as oxide-assisted growth,[48] epitaxial growth[7] etc, have been suggested to complement the conventional VLS theory. The oxide-assisted growth emphasizes that it is essential to form a thermodynamically unstable oxide phase. At low temperature, decomposition of the unstable oxide provides the nucleus for NW formation and temperature gradient provides the driving force for NW growth. The epitaxial growth emphasizes the function of a lattice-matched substrate in forming epitaxially grown

11

aligned NWs. It is worth mentioning that these approaches also work without the presence of a metal catalyst in some circumstances,[52, 53, 55] which simplifies the process for the purification and subsequent applications of the NWs. It is also suggested by Wang *et al*[45] that the VLS could be more probably described by a vapor-solid-solid (VSS) mechanism. In their experiments, no eutectic phase of Zn and Au could be detected in the as-grown ZnO nanowires. They also suggest that the growth of ZnO proceeds by surface diffusion rather than bulk diffusion.

1.3.4 Other nanostructure growth methods

1.3.4.1 Wet-chemical method

Wet-chemistry is the most successful technique for shape-selective synthesis of quantum dots, wires, tetrapods and multi-branched heterostructures. A great advantage of this approach is that it does not require an expensive experimental set-up, as well as low temperature growth. However, the nanocrystals length typically does not exceed a few hundred nanometers, which limit their suitability for some applications. Also, these methods usually result in poor crystal quality compared with VPT grown crystals, due to ion impurities involved and the formation/presence of an amorphous phase inherent for depositions carried out at low temperatures. In addition, selective growth of the nanostructures in defined positions on a substrate is difficult, and therefore requires post-deposition handling. Only recently, ZnO NWs selectively grown on lithographically patterned Si has been realized via a solution method.[77]

1.3.4.2 Template-based synthesis

The template-based synthesis of nanostructured materials is a very general method and can be used in fabrication of nanorods (NRs), NWs, and nanotubes made of polymers, metals, semiconductors and oxides. The most commonly used and commercially available templates are anodized alumina membrane (AAO),[78] and radiation track-etched polymer membranes.[79] The pores are arranged in a regular hexagonal array and densities as high as 10^{11} pores/cm^2 can be achieved. Pore size ranging from 10 nm to 100 μm can be created.

The template can be applied to wet-chemical and vapor-phase depositions, such as electrochemical, electrophoretic, chemical vapor deposition etc.; direct filling of the template to synthesize nanostructures using colloids, melt and solutions have also been reported.[80] Although oxides synthesized by these methods can be 10 nm thick and tens micromenter long, they are usually polycrystalline, and the growth is not site selective as well.

1.4 Surface modification by plasma immersion ion implantation

When the size of a crystal structure decreases, the surface area increases, resulting in more surface-related defects. Therefore, the properties of a nanostructure, such as gas-sensing, field emission and PL, etc, are much more sensitive to its surface states than that of bulk material. By quenching these surface states, surface modification allows us to improve those surface-related properties. Plasma immersion ion implantation (PIII) is a well developed surface modification technique,[81-84] which was initially developed by Conrad[84] in 1987 as an alternative to overcome some limitations of conventional ion implantation. It is a simple, non-line-of-sight process, as opposed to conventional

beamline ion implantation; non-planar samples can be implanted with good conformality and uniformity without special sample manipulation. Compared to conventional ion implanters, this technique is able to reduce processing times for a larger area and at a lower cost, and it has been mostly applied to conductive or semi-conductive materials. During PIII, the substrate is immersed in plasma and negative voltage pulses can be applied to implant ions from the plasma to the surfaces. The modification depth can be well controlled by the bias voltage, which is suitable for surface modification of thin films and nanostructures with complicate morphologies.[81, 85] Current research of the PIII is focused on modification of polymer and diamond-like carbon film, and impurity doping, etc.[82, 83, 86, 87] However, the surface modification of nanostructures by PIII has been much less investigated in the previous literatures.

1.5 ZnO 1D nanostructures-focus of this thesis

1.5.1 Motivation

Due to its distinguished performance in electronics, optics and photonics, fabrication of ZnO thin films has been an active field for their applications in sensors, transducers, and catalysts, ever since 1960s. The interest in ZnO structures has increased drastically in recent years, as can be seen from a surge of relevant number of publications since 2000, including numerous conferences, workshops, and symposia by more than 2000 records since year 2005, compared to slightly beyond 100 in 1970 (sources: INSPEC, Web of Science).

The nanostructured ZnO is a multifunctional material with great potential for a variety of practical applications, such as piezoelectric transducers,[88] optical waveguides, surface

acoustic wave devices, varistors, phosphors, transparent conductive oxides, functional spin-electronic devices, field emissions,[89, 90] and UV-light emitters/detectors.[91-95] Its wide band gap ($\approx$3.37 eV at room temperature) makes ZnO a promising material for photonic applications in the UV or blue spectral range, while the high exciton-binding energy (60 meV)[91] allows efficient excitonic emission even at room temperature. This binding energy increases further in ZnMgO/ZnO/ZnMgO quantum wells.[96] The bandgap of ZnO could also be turned from 3.37 eV (at room temperature) to 4 eV by alloying with Mg[96] and to 2.9 eV for the ZnCdO alloys.[91, 97] Bandgap tuning by transition metals, such as Mn, Co, and Ni, etc.,[98] has also been reported. ZnO based quantum wells are of type I, thus ideal for optoelectronic devices which need electrical and optical confinement. In addition, ZnO doped with transition metals shows great promise for spintronic applications.[91, 99] It has also been demonstrated that ZnO nanostructure-based gas sensors for H_2, CO, NH_3, etc, are suitable for sensing applications.[8] Also, ZnO is biocompatible which makes it suitable for biomedical applications.[100] Last but not least, ZnO is chemically stable, bio-compatible, and has abundant mineral sources.

1.5.2 Properties of ZnO

1.5.2.1 Crystal structures

ZnO has three possible crystal structures: wurtzite-type, cubic zinc blend-type and rock salt structures, respectively. Under most circumstances, it crystallizes in the hexagonal wurtzite-type structure (Figure 1.4). In this structure, it has a polar hexagonal axis, the c-axis, chosen to be parallel to z. The point group is 6 *mm* or C_{6v}, the space group $P6_3mc$ or C_{6v}^4. One Zn ion is surrounded tetrahedrally by four O ions and viceversa. In

contrast to other II^b-VI semiconductors, which exist both in the cubic zinc blende and the hexagonal wurtzite-type structures (such as ZnS, which gave the name to both structures), ZnO crystallizes with great preference in the wurtzite-type structure. The cubic zinc blende-type structure can, to some extent, be stabilized by epitaxial growth of ZnO on suitable cubic substrates, while the rock salt structure is stable only under pressure.[101]

The lattice constants of wurtzite ZnO at room temperature determined by various experimental measurements and theoretical calculations are in good agreement. The lattice constants mostly range from 3.2475 to 3.2501 Å for the *a* parameter and from 5.2042 to 5.2075 Å for the *c* parameter. It has been reported that free charge is the dominant factor responsible for expanding the lattice proportional to the deformation potential of the conduction-band minimum and inversely proportional to the carrier density and bulk modulus.[91] The point defects such as zinc antisites, oxygen vacancies, and extended defects, such as threading dislocations, also increase the lattice constants, albeit to a lesser extent in the heteroepitaxial layers.[91]

The tetrahedrally coordinated wurtzite-type crystal structure is a characteristic for covalent chemical binding with sp^3 hybridisation. The bonding nature between Zn and O ions is right between covalent and ionic binding, while the Group IV element semiconductors like diamond, have completely covalent bonding , and group Group II^a-VI and I^a-VIII insulators like MgO or NaCl have completely ionc binding. Due to this fraction of ionic binding of ZnO, the bottom of the conduction band is formed essentially by the $4s$ levels of Zn^{2+} and the top of the valence band by the $2p$ levels of O^{2-}. The band gap of ZnO between the conduction band and the highest valence band is about 3.437 eV at low temperatures.
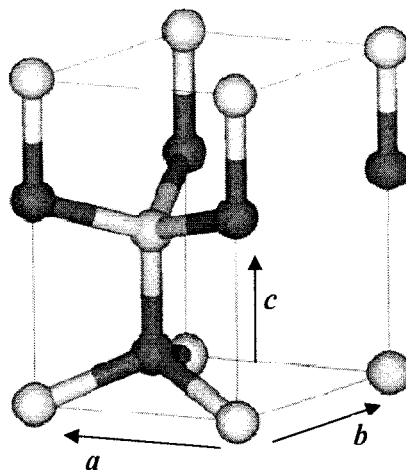
Figure 1.4 Unit cell of the crystal structure of ZnO. The light grey/yellow spheres correspond to oxygen, the dark/blue ones to zinc. The primitive translation vectors *a* and *b* include an angle of 120° and are situated in the base plane. *c* is orthogonal to them.[101]

The fact that ZnO has partial ionic bonding and lacks a center of inversion results in piezoelectricity. As shown in Figure 1.4, the hexagonal unit cell contains two formula units (A formula unit is the empirical formula of an ionic or covalent network solid compound for stoichiometric calculations. In ZnO unit cell, it is Zn_2O_2) and the crystal exhibits basal polar planes [oxygen terminated $(000\bar{1})$ faces and tetrahedron corner-exposed Zn faces (0001) as well as two types of low-index faces consisting of non-polar faces $(\bar{1}000)$ and C_{6v} symmetric ones]. The low-symmetry non-polar faces, with 3-fold coordinated atoms are the most stable ones. Additionally, there is no center of inversion in the wurtzite structure and thus, an inherent asymmetry along the *c*-axis is present allowing the growth of anisotropic crystallites and nanostructures. In addition to the inherent anisotropy along the *c*-axis, the wurtzite structure shows piezoelectric activity, which is currently being studied for building nano-scale electro-mechanically coupled sensors and transducers[88] due to a large and permanent electric dipole moment, which have been

17

observed experimentally to scale with the volume of the nanocrystal.[102] The unique polar surfaces in ZnO: the basal plane, $\pm$ (0001), as well as $\{01\bar{1}1\}$ planes, induce a dipole moment and spontaneous polarization, as well as a divergence in surface energy. The spontaneous polarization dominated by $\pm$ (0001) polar surfaces was the main driving force in forming nanosprings and nanorings, while $\{10\bar{1}1\}$-type polar surfaces have been observed in a nanohelical structure.[88] Due to the absence of inversion symmetry in wurtzite structure, second-order dipole moments are of even greater amplitude compared to other (homo)polar crystals.[103] The three coefficients of the piezoelectric tensor, d_{15}, d_{31}, and d_{33}, are rather large, with values around -10, -5, and 12×10^{-12} mV^{-1}, respectively.[91]

1.5.2.2 Electrical properties of undoped ZnO

There has been an intense study on the electrical properties of undoped ZnO material (films, single crystals and 1D nanostructures), both experimentally and theoretically.[91] The un-doped ZnO is an intrinsic n-type semiconductor, which is related to the oxygen vacancies, i.e., higher oxygen vacancy density results in a higher electron density.[104] Table 1.1 below summaries the electrical parameters of wurtzite ZnO crystal.

Table 1.1 Electrical properties of wurtzite ZnO.[105-107]

Parameters	Value
Zero-frequency dielectric constant	$\varepsilon_0^{\parallel}=8.8\pm0.4$, $\varepsilon_0^{\perp}\pm0.3$
Static dielectric constant	$\varepsilon^{\parallel}=11$, $\varepsilon^{\perp}=8.5$
Bulk dielectric constant	$\varepsilon_r=3.7$
Static relative permittivity	$\varepsilon_{st}=6.51$
Energy gap	3.37 eV, direct
Intrinsic carrier concentration	$<10^6$ cm^{-3} (max n-type doping $>10^{20}$ cm^{-3} electrons; max p-type doping $<10^{17}$ cm^{-3} holes
Electron effective mass	0.24
Electron Hall mobility at 300 K for low n-type conductivity	200 cm^2/Vs
Electron effective mass of quantum sized clusters	0.24-0.28
Hall effective mass	0.59
Hole Hall mobility at 300 K for low p-type conductivity	5-50 cm^2/Vs
Hole effective mass of quantum sized clusters	0.45-0.59
Resistivity with electron concentration of 10^{17}/cm^3	7.06 Ωcm
Mobility (NW)	8.85 cm^2/Vs

1.5.2.1 *n*- and *p*-type doping of ZnO

The main problem for the application of ZnO for electro-optic devices is ambipolar doping. This problem is frequently found in wide-band-gap materials and occurs when doping of one type (e.g. *n*-type conductivity due to electrons in the CB) is easily up to high densities, while the opposite type (in this case due to holes in the VB) is hardly

achievable. The semiconductors ZnO, ZnSe, CdS or GaN are, for example, generally *n*-type while ZnTe is generally *p*-type.

Similar to the *n*- and *p*-type doing of elemental Si semiconductor, one would choose to substitute Zn or O with atoms which have one electron more in the outer shell than the atom (Group III elements Al, Ga, and In) which they replace for *n*-type doing, and vice versa (Group I elements Li, Na, or K, Group I^b elements Cu and Ag, Group V elements N, P, or As) for *p*-type doing. Basically, good donors or acceptors should have an ionic radius close to that of the host ion in order to retain the lattice structure, and must also have close electronegativity to make energetically favorable its incorporation into the lattice. Table 1.2 summarizes the valence and ionic radii of candidate dopant atoms for ZnO.

It has been demonstrated that Al, Ga, and In are good shallow and efficient donors when they replace Zn according to the equation:

$$D^o \leftrightarrow D^+ + e^-, \tag{1.4}$$

where D^o and D^+ are the neutral and ionized donors, respectively, and the equilibrium at room temperature is essentially on the right-band side of Equation (1.4). Electron concentrations beyond 10^{20} cm^{-3} are obtained in ZnO:Al or ZnO:Ga, which even at room temperature result in a degenerate electron gas in the conduction band.[108]

The problem of *p*-type doping of ZnO with Li, Na, K, Cu, and Ag is that they are usually deep acceptors with ionization energies around a few hundred eV, that is, much larger than $k_B T$ at room temperature. As shown in Equation (1.5) below, the equilibrium at room temperature is on the left-hand side:

$$A^o \leftrightarrow A^- + \text{hole} \tag{1.5}$$

Table 1.2 Valence and ionic radii for candidate donors and acceptors of ZnO.

Atom	Valence	Ionic radius (Å)
Zn	2+	0.60
Al	3+	0.39
Ga	3+	0.47
In	3+	0.62
Li	1+	0.59
Na	1+	1.13
K	1+	1.51
Cu	2+	0.71
Ag	1+	1.00
P	3+, 5+	0.58, 0.34
As	3+, 5+,	0.58, 0.47
Mn	2+	0.80
Co	2+	0.38
Ni	2+	0.55
Fe	2+, 3+	0.77, 0.63
O	2-	1.38
N	3-	1.46
P	3-	2.12
As	3-	2.22
F	1-	1.31

Therefore, ZnO doped with those acceptors usually shows rather low p-type conductivity. However, successes using codoping methods have resulted in some shallow acceptor complex in ZnO,[109-111] which uses either two different acceptors simultaneously or by combining a moderate concentration of donors with a higher concentration of acceptors. Experimental results also show that N could incorporated into the lattice in the form of single atoms or ions, and form a shallow acceptor with small ionization energy (about 100 meV), whereas the doping level is limited to only 10^{17} cm^{-3}.[112] In addition, both As and P

has been reported as among the very few *p*-type dopants of ZnO recently.[91, 113-120] The As

or P doped ZnO film shows highly *p*-type conduction, which does not rise from the simple

substitution of O with P. Since there is large size mismatch between As^{3-} and O^{2-} but a

good match between As^{3+} and Zn^{2+} (see Table 1.2), and the electronegativity of As (2.0) is

closer to Zn (1.6) than that of O (3.5), the incorporation of As as dopant in ZnO in Zn site

is energetically favorable to be incorporated on Zn sites. This discovery might open the

door to reliable and highly conductive *p*-type ZnO fabrication.

1.5.2.2 Optical properties of ZnO

The application of semiconductors in electroptical devices relies on their ability to

efficiently emit or detect light.[93, 121, 122] If photons of energy greater than or equal to the

band gap are incident on a semiconductor, they may excite an electron from the valence

band to the conduction band. In this process, the photon is absorbed and an electron and a

hole are created. In the reverse process an electron in the conduction band may return to

the valence band and recombine with a hole; the energy lost by the electron creating a

photon. As the energies of the electron and hole will generally be very close to the bottom

of the conduction band and the top of the valence band respectively, the emitted photon

will have energy approximately equal to the bandgap of the semiconductor.

The optical properties of a semiconductor are connected with both intrinsic and

extrinsic effects. They have been studied by several methods, such as photoluminescence

(PL), cathodoluminescence (CL), electroluminescence (EL), etc. Among them, continuous

wave (cw) PL is a suitable tool to determine the crystalline quality and the presence of

impurities in the material as well as exciton fine structure. PL spectra of ZnO

nanostructures measured at room temperature and low temperature have been intensively

studied.[93, 121, 123-137] In particular, 1D ZnO nanostructures have attracted a great attention with a possibility to develop nanoscale electronic and optoelectronic devices.[93, 121, 125, 131] The PL spectrum of ZnO nanostructures typically consists of a UV emission and possibly one or more visible bands due to defects and/or impurities.

1.5.2.2.1 UV emission of ZnO nanostructures

Low-temperature PL measurements of single crystals, films, and different nanostructures, such as NW/nanowall systems, nanosheets, nanowalls, NWs, nanoparticles, etc, have been reported. [123, 126, 133, 138-142] The low-temperature PL spectra of ZnO measured at 10 K or below typically exhibit free-exciton (FX) and bound-exciton peaks. The intrinsic FX transition at low-temperature could be observed from high quality ZnO single crystals and some of the nanostructures, and free excitonic fine structure could be resolved from the spectrum. An example of the FX emission is shown in Figure 1.5. The A-FX and its first excited state emission are observed at $FX_A^{n=2}$=3.3771 eV (3.3757 eV for Γ_6) and $FX_A^{n=1}$=3.4220 eV for Γ_5 (3.4202 eV for Γ_6) band symmetry, respectively. The energy difference of about 45 meV gives an A-free exciton binding energy of 60 meV and corresponding band gap energy of 3.4371 eV at 10 K. The weak emission centered at 3.3898 eV is assigned to the B-FX transition.
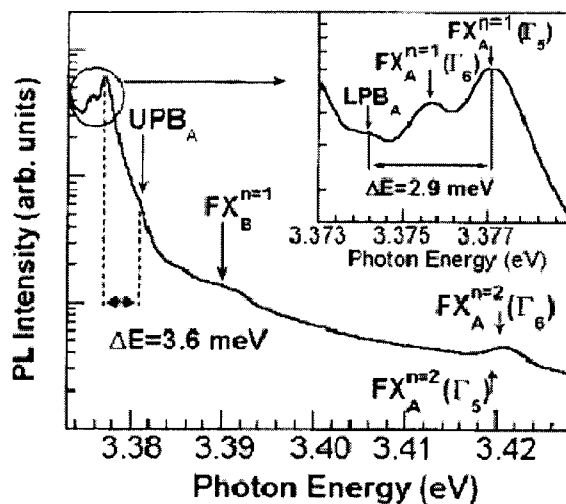
Figure 1.5 Free excitonic fine structure region of the PL spectrum at 10 K for the

forming gas annealed ZnO single crystal.[123]
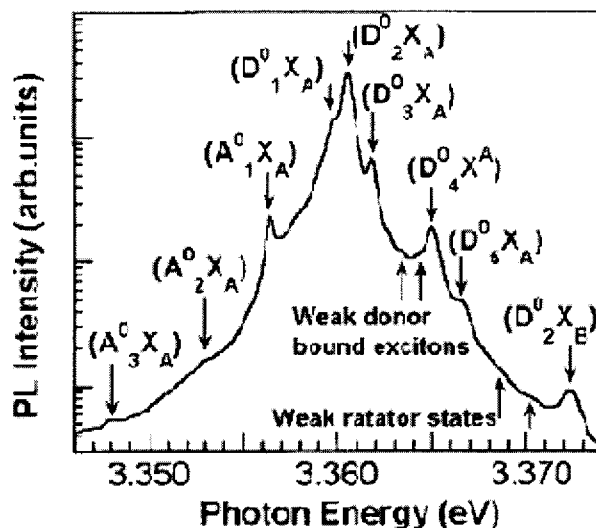
Figure 1.6 Bound excitonic region of the 10 K PL spectrum for the forming gas

annealed ZnO single crystal.[123]

The extrinsic properties are related to dopents or defects, which usually create discrete

electronic states in the band gap, corresponding to bound-exciton peaks observed at low

temperature, in the range from 3.348 to 3.374 eV for ZnO single crystal (Figure 1.6). The

bound exciton states for neutral shallow donors (DBE) and acceptors (ABE) are the dominant couplings in most of the ZnO samples.

In addition to free- and bound exciton emissions, the UV spectra of ZnO at low temperature can also contain donor-acceptor pair transitions and longitudinal optical (LO) phonon replicas, with up to third-order LO phonon replicas can be typically observed. The LO phonon energy can be determined from the separation between the exciton peaks and their LO phonon replicas, and for ZnO it is 71-73 meV.[123]

1.5.2.2.2 Visible emissions of ZnO

Room-temperature PL spectra from ZnO usually exhibit a broad peak in the visible spectrum, corresponding to the deep-level energy levels of ZnO, which is also referred to as defect emission. The peak positions can vary from blue, green, yellow to red, depending on the fabrication conditions, such as growth temperature, source material, as well as post-treatment conditions. Green emission is the most commonly observed and intensively studied defect emission in ZnO nanostructures and single crystals, centered ~2.3 eV.[128, 129, 134, 135, 143-145] Several different hypotheses have been proposed, including antisite oxygen, Cu impurities, zinc vacancy, and surface defects, etc,[145] and it is commonly attributed to singly ionized oxygen vacancies ($V_O^\bullet$).[128, 129]

1.5.3 *p-n* junctions-the way to realize light-emitting devices

The majority of semiconductor devices incorporate at least one *p-n* junction, which is formed at the interface between two regions, doped *n*-type and *p*-type, respectively. If equilibrium, a potential step is formed at the interface which prevents the net movement

of electrons from the n-type region into the p-type region, and vice versa for holes. In addition, free carriers are absent from regions on either side of the junction, forming a depletion region. A schematic diagram of a p-n junction under equilibrium conditions is shown in Figure 1.7. If an external voltage of the correct sign is applied, the potential step is reduced, allowing electrons and holes to move across the junction, a process known as injection. In a p-n junction designed for optical application, an undoped or intrinsic region may be placed between the n- and p-type regions to form a p-i-n structure. Electrons and holes meet in the intrinsic region, where they recombine to produce photons. A nanostructure may be incorporated within the intrinsic region, providing a convenient and efficient mechanism for injection of electrons and holes into the nanostructure. The bias condition for current injection is referred to as forward bias. Changing the polarity of the applied voltage produces reverse bias. In reverse bias, the potential step is increased and there is negligible current flow. However, electrons and holes created in the intrinsic region by photon absorption may be swept out into the n- and p-type regions, respectively, resulting in an electrical current that can be measured by an external circuit. This process allows a semiconductor to act as a photodetector.
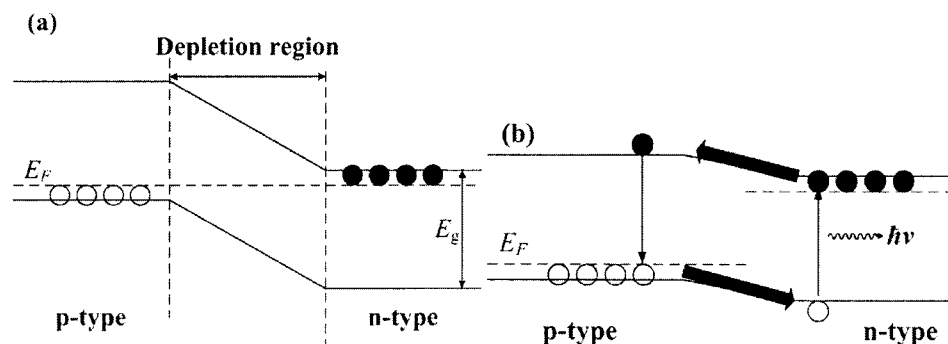
Figure 1.7 Schematic band diagrams of a p-n junction (a) under equilibrium conditions and (b) with an external voltage applied to reduce the potential step, resulting in easier injection across the junction.

There has recently been an increasing interest in ZnO for applications in optoelectronics such as light-emitting diode (LEDs), UV lasers, and UV light detectors because of its wide direct band gap. In comparison with GaN, ZnO has some obvious advantages for optoelectronic applications due to the availability of single crystal substrates, relatively low growth temperature and a large exciton binding energy (~60 meV), as demonstrated by efficient excitonic lasing on optical excitation as well as random lasing at elevated temperature.[93, 146, 147]

1.6 Major contributions

The main contributions in this thesis are as follows:

1. Controlled growth of various ZnO nanostructures has been achieved, including nanocombs (NCBs), random nanowires (RNWs), aligned nanowires (ANWs), diamond-shaped microrafts and beads, and resistors-shaped nanowires (RSNWs). The growth mechanisms have been studied; large area, uniform size, and repeatable synthesis have been achieved.

2. Detailed nanostructure characterization and analysis using scanning electron microscopy (SEM), transmission electron microscopy (TEM), Raman, PL, etc., have been conducted. The crystalline, morphological, optical, magnetic, and chemical properties have been studied.

3. Enhancing the optical properties of ZnO NCBs and NWs has been achieved by PIII surface modification. The UV emission has been enhanced and the visible emission has been completely quenched. The modification effect on the UV and visible emission has been studied in detail.

4. Synthesis of ternary oxide (Zn_2TiO_4) NWs has been achieved using ZnO NWs as template. Detailed characterization of the twinned spinel NWs has been conducted; formation mechanism has been studied.

5. ZnO aligned NR based *p-n* homojunction LED device has been fabricated and characterized. Strong red electroluminescence (EL) has been observed.

1.7 Organization

In Chapter 1, the thesis begins by giving a brief introduction on the nanotechnology and growth of various 1D nanostructures by vapor-phase method, followed by the motivation to study ZnO nanostructure as the focus of this thesis, as well as a brief review on ZnO (crystalline, electrical and optical) properties and the applications of ZnO in growth of ternary oxide NWs and optoelectronics. The main contributions and organization of the thesis are also presented in this chapter.

Chapter 2 describes the VPT fabrication methods for ZnO nanostructures adopted throughout this work (Chapters 3-8), the surface modification method adopted in Chapters 5 and 6, and the characterization approaches adopted in this work.

Chapter 3 presents the fabrication and characterization of Cu-doped ZnO diamond-shaped microraft. The optical and magnetic properties, as well as the formation mechanism of the diamond shape have also been studied.

Chapter 4 presents the fabrication and characterization of high purity RSNWs grown in a similar environment as that of diamond-shaped microraft, with an increased growth species vapor pressure. The role of Cu and water vapors in forming the RSNWs has been

discussed. The special paired-crystalline structure of RSNWs has been studied by high-resolution TEM (HRTEM).

The uniformity and repeatability of ZnO nanostructures are further improved by applying both vacuum and controlled flow of O_2 and Ar to the high temperature growth at 950°C. However, due to the large surface area of nanostructures, the PL spectrum usually has a low UV/visible-emission ratio. Chapter 5 presents the efficient PIII surface modification and enhancement in UV emission of NCBs that grown in oxygen-rich environment. The modified crystal surface has been studied by HRTEM, while the UV emission has been characterized by both room temperature and low-temperature PL.

Chapter 6 presents the efficient surface modification by PIII and complete green band luminescence quenching for various ZnO nanostructures (NCBS, RNWs, and ANWs) grown in either oxygen-rich or oxygen-deficient environments. The modified crystal surface has been studied by HRTEM. Room temperature and low-temperature PL in the visible region has been studied in detail.

Chapter 7 presents the fabrication and characterization of twinned spinal Zn_2TiO_4 ternary oxide NWs from solid-state reaction of ZnO/Ti core/shell nanostructure. ZnO NWs are used as the template for formation of Zn_2TiO_4 NWs. Detailed SEM and HRTEM analysis revealed the twinned nature of the product.

Chapter 8 presents the device fabrication of a *p-n* homojunction LEDs based on ZnO ANWs. The *I-V* characteristics of single and bulk ZnO *p-n* junctions have been analyzed. Strong red EL emission (~650 nm) has been achieved.

Chapter 9 summarizes the work presented in this thesis, as well as given recommendations for future work in related areas.

Chapter 2 EXPERIMENTAL AND METHODOLOGY

2.1 Experimental

2.1.1 Growth of ZnO nanostructure by using the VPT method

VPT is a widely available technique. In principle, it combines the advantages of both wet-chemical and molecular beam techniques, and generally the growth mechanisms by VPT method can be either VS (without catalyst) or VLS (with catalyst or self-catalyzed), as briefed in Chapter 1. The growth of ZnO by VPT is typically affected by the temperatures of both the source and the substrate, the heating rate, the gas flow rate, tube diameter, the source content, and the substrate. The influence of these factors on ZnO morphology has been reported recently, but the effects of these factors on morphology control, crystal quality, and optical properties of fabricated nanostructures are not fully understood. Post-annealing or surface modification has been investigated to improve the crystal quality and optical properties.

The horizontal tube furnace is one of the simplest and most popular equipments used to implement VPT. The program controlled tube furnace used in this thesis was developed by Hefei Risine Heateck Co., Ltd., China. Figure 2.1 shows the schematic diagram of the tube furnace. In general, a thin (2-20 nm) Au film is first sputtered onto a (111) Si

substrate. The growth source, ZnO and graphite powders are well mixed with weight ratio of 1:1. Both the source and the Si substrate are loaded into a small quartz tube 2 cm in diameter. Then the whole set is manually pushed to the center of the furnace, where the source is at the heating point of the furnace, and the substrate was put at the downstream side. The growth temperature is maintained at either 1100° or 950° for fabrication of various nanostructures in this thesis.

In order to improve the uniformity and repeatability of the synthesized nanostructures while at the same time decrease the size of nanostructures, and uniformly grow on a large substrate area (1.5 cm^2), vacuum was applied. The furnace is pumped down immediately to a base vacuum level of $\sim 1 \times 10^{-2}$ Torr after the small quartz tube has been loaded into the furnace. The gas flows of Ar and O_2 (99.999%) are varied to synthesize different morphologies of nanostructures, such as NCBs (Chapter 5), random NWs (Chapter 6 and 7) and aligned NWs (Chapter 6 and 8).
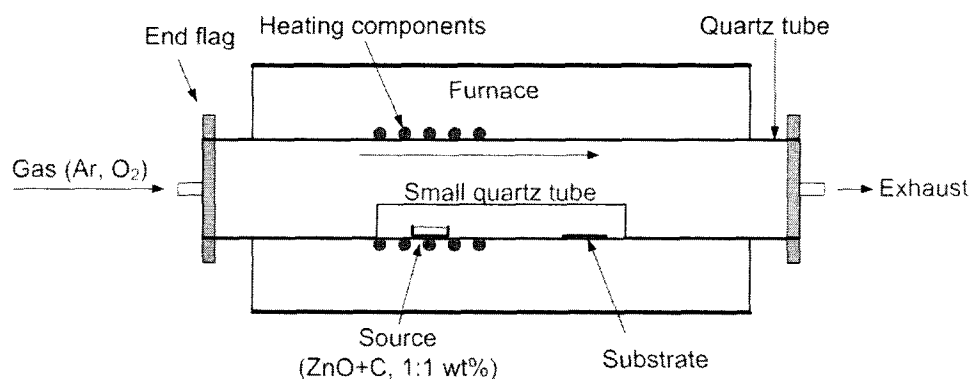
Figure 2.1 Schematic diagram of the horizontal tube furnace used in this work.

2.1.2 Surface modification by PIII

In our work, the PIII technique has been combined with condensable plasmas from a filtered cathodic arc source. Modification by the PIII technique is accompanied with Ar plasma, results in ion implantation in all directions into the exposed sample surface. Thus, this technique can efficiently modify the sample surface while reserving the morphology of the nanostructure.

Figure 2.2 shows the schematic diagram of this PIII (HV Pulser) system used in this thesis, which was developed by the Australian Nuclear Science and Technology Organization (ANSTO). It has a power supply which is capable of delivering negative voltage pulses up to 30 kV with varying frequencies and pulse duration. The high-voltage pulsed source enables both ion implantation and deposition with controlled portion. In our experiments, the pulsed voltage affecting the implantation depth is varied, and the
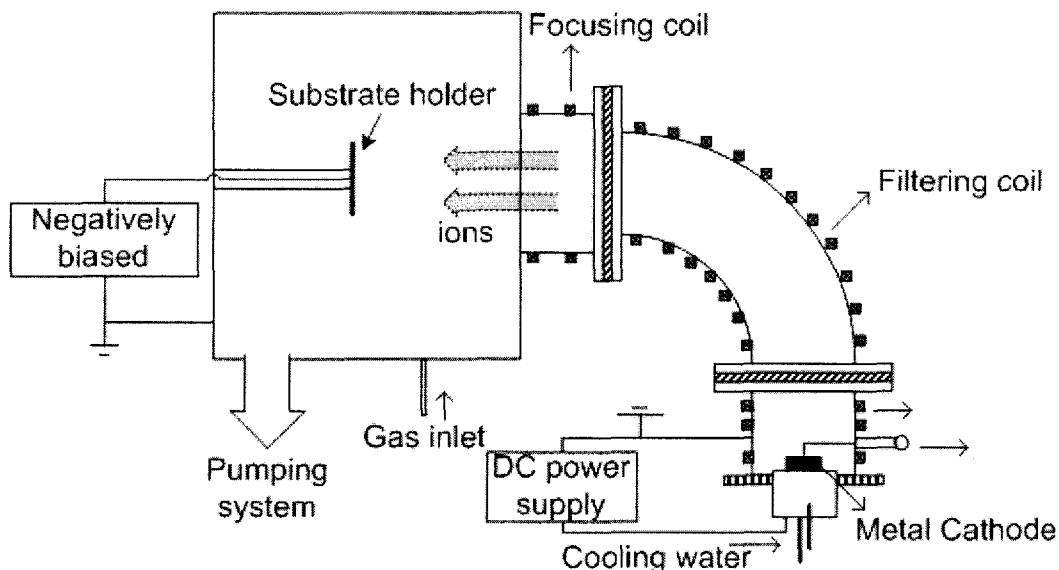
Figure 2.2 Schematic diagram of the plasma immersion ion implantation system equipped with a filtered metal cathodic arc system and a high voltage pulsing system.

pulse voltage and frequency were optimized to achieve the highest ion implantation portion instead of deposition. The ion implantation depth was simulated using commercially available software SRIM.[148]

2.2 Sample characterization and methodology

2.2.1 X-ray diffraction techniques

X-ray Diffraction (XRD) techniques are a family of non-destructive analytical techniques which reveal information about the crystallographic structure, preferred orientation, strain, crystal quality, chemical composition, and physical properties of materials and thin films. These techniques are based on observing the scattered intensity of an X-ray beam hitting a sample as a function of incident and scattered angle, polarization, and wavelength or energy.

The reflection of an X-ray from the surface of the sample follows Bragg's law:

$$n\lambda = 2d\sin\theta \qquad (2.1)$$

where λ is the wavelength of the x-ray, θ is the angle between the incident X-ray and the surface of the crystal, also referred to as Bragg angle, n is an integer, and d is the spacing between the parallel lattice planes. Constructive interference occurs when n is an integer; the reflected waves from different lattice planes are in phase and produce sharp peaks in the spectrum.

In this thesis, all the measurements were carried out by XRD in 2θ geometry with a Siemens D5005 diffractometer using Cu $K_{\alpha 1}$ ($\lambda = 0.154$ nm) radiation under the

accelerating voltage of 40 kV. The data were collected over a scattering angle range of 25°-80° in 0.05-0.01° intervals.

2.2.2 Scanning electron microscope

The scanning electron microscope (SEM) is a type of microscope capable of producing high-resolution images of a sample surface. Due to the manner in which the image is created, SEM images have a characteristic 3D appearance and are useful for judging the surface structure of the sample. The instrument was first invented by Manfred von Ardenne in the 1930s, and was further developed by Charles Oatley. It was first commercialized by Cambridge Instruments.[149]

In a conventional SEM, such as the JSM-5910LV used extensively in the thesis, electrons are thermionically emitted from a tungsten cathode and accelerated towards an anode operated at 15 or 20 kV. Tungsten is used because it has the highest melting point and lowest vapor pressure of all metals, thereby allowing it to be heated for electron emission. It is also much cheaper compared with lanthanum hexaboride (LaB_6). It operated at low vacuum with a resolution of 3 nm. In addition, due to the large working distance of 15 mm, the sample stage can be easily tilted by 20-30°. A tilted view is useful for observing aligned NW samples.

Another SEM (JSM-6340F) also used in this thesis is a cold field emission scanning electron microscope (FESEM) with advanced high resolution imaging operated at low voltage. The electron is emitted via field emission (FE) from LaB_6 cathode. The device is highly suitable for low voltage microscopy, which makes it much easier to observe details

34

on the outer surface of the material. In this thesis work, the FESEM is operated at 5 kV with a resolution of about 2 nm.

2.2.3 Energy dispersive X-ray spectroscopy

Energy dispersive X-ray spectroscopy (EDX/EDS) is an analytical tool predominantly used for chemical characterization. It relies on the investigation of a sample through interactions between X-rays and mater. Its characterization capabilities are due in large part to the fundamental principle that each element of the periodic table has a unique electronic structure and a unique response to electromagnetic waves.

In this thesis, we used the EDX installed with the SEM (JSM-5410LV), where tungsten cathode is used as the electron source with accelerating voltage of 15-20 keV. The quantitative X-ray analysis is conducted using Link ISIS 300 software.

2.2.4 Transmission electron microscopy

Transmission Electron Microscopy (TEM) is lattice level high resolution electron microscopy technique whereby a beam of electrons is transmitted through a specimen, forming an amplified image on a fluorescent screen, or a layer of photographic film, or onto a sensor such as a CCD camera. The first practical TEM was built by Albert Prebus and James Hillier at the University of Toronto in 1938 using concepts developed earlier by Max Knoll and Ernst Ruska.[150]

Nowadays, TEM is used widely in material science. It gathers crystallographic (through electron diffractions and lattice high resolution images) and chemical data

(through EDS) at unit cell or near unit cell scale. HRTEM images are phase contrast images. They are formed by using a large objective aperture to select many beams to reconstruct a yield contrast that can be interpreted in terms of the projected crystal potential, which is directly related to the atomic structure of materials. Information of nanostructures such as size, shape, lattice diameter, perfection, orientation, composition, surface structure and defects can be directly obtained from TEM and HRTEM images.

In this thesis, the detailed TEM/HRTEM studies were performed using a TEM (JEOL JEM-2010) operating at 200 kV. The electron gun used was LaB_6 thermionic emission source, and the point resolution is 1.9 Å.

Besides HRTEM, bright field (BF) and dark field (DF) TEM were also implemented. The BF images are formed when a small objective aperture is centered about the optic axis to exclude scattered electron. Regions of specimen that are thicker or denser will scatter electrons more strongly and appear darker in the image. The DF images are formed using electrons scattered from the specimen and selected from imaging using a small objective aperture. The BF and DF images are particularly sensitive to extended crystal lattice defect, such as dislocations.

For sample preparations, the sample was ultrasonically dispersed in ethanol first. Then several drops of the solution were dropped onto a special TEM copper grid and dried. Alternatively, the nanostructures on the substrate were scratched off and dispersed on the TEM copper grids. There was no further treatment of the TEM samples.

2.2.5 Photoluminescence spectroscopy

The optical properties of a semiconductor are connected with both intrinsic and extrinsic effects. Photoluminescence (PL) spectroscopy is a contactless, nondestructive method of probing the electronic structure of materials. It is a suitable tool to determine the crystalline quality and the presence of impurities in the material as well as exciton fine structure. Light is directed onto a sample, where it is absorbed and imparts excess energy into the material in a process called photoexcitation.

In this thesis, the room temperature PL measurements were carried out using a Renishaw Micro-PL system with a 1800 grooves/nm grating. The excitation line used was 325 nm and the average laser power detected at the front of microscope lens was 1.5 mW (100%). The low-temperature PL measurements were carried out with the sample placed in a close-cycle He gas cryostat in the temperature range of 4.5-300 K. A 325 nm He-Cd laser was used as the excitation source.

2.2.6 Raman spectroscopy

Raman is a spectroscopic technique used in condensed matter physics and chemistry to study vibrational, rotational, and other low-frequency modes in a system. It relies on inelastic scattering, or Raman scattering of monochromatic light, usually from a laser in the visible, near infrared, or near ultraviolet range. In this thesis, we used a Ranishaw Micro-Raman system with a 3600 grooves/nm grating. The excitation line used was 514 nm.

2.2.7 X-ray photoelectron spectroscopy

X-ray photoelectron spectroscopy (XPS), also known as electron spectroscopy for chemical analysis (ESCA), is a quantitative spectroscopic technique that measures the elemental composition, empirical formula, chemical state and electronic state of the elements that exist within a material. XPS spectra are obtained by irradiating a material with a beam of X-rays while simultaneously measuring the kinetic energy and number of electrons that escape from the top 1 to 10 nm of the material being analyzed. Therefore, it is a surface chemical analysis technique. The XPS measurement requires ultra-high vacuum (UHV) conditions.[151]

In our work, the elemental analysis on the shallow surface of the samples was performed in a Kratos AXIS Ultra spectrometer with a monochromatized Al K_a X-ray source (1486.71 eV) operated at a reduced power of 150 W (15 kV and 10 mA). The base pressure in the analysis chamber was 2.66×10^{-7} Pa. The core-level spectra were obtained at a photoelectron take-off angle of 90° measured with respect to the sample surface and were recorded in 0.1 eV step with the pass energy of 40 eV. The binding energy scale of the XPS spectrum was calibrated with the C 1s peak (neutral C-C peak at 284.5 eV).

Chapter 3 FABRICATION OF

DIAMOND-SHAPED ZNO

3.1 Introduction

Wurtzite ZnO has been demonstrated to be the material with the most prolific usage for the fabrication of nano/micro-structures up to now, including wires,[152, 153] ribbons,[154] rings,[37] sheets,[155] tetrapods,[156] tubes,[157, 158] belts,[159, 160] disks,[161] walls,[162] cages,[163] combs,[164] etc. Synthesis and studies of growth mechanism of these ZnO nano/micro-structures have been an active field because of their peculiar physical properties of exotic 1D structures and hierarchical self-assembled two or three-dimensional structures. Various synthesis methods, such as VTP[90, 94, 161], thermal evaporation,[38] metal-organic vapor-phase epitaxy (MOVPE),[165] aqueous thermal decomposition,[166] aerosol route,[167] electrochemical deposition,[168] and ion beam sputtering[95] have been reported. Most of the structures reported, including rods and combs, are hexagonal-natured morphologies. Only recently, Yu *et al,*[169], Wang *et al,*[170] have synthesized ZnO NRs with cross section reduced from hexagonal to diamond, which is only one-third of a hexagonal. However, the growth mechanism is still not clear and diamond-shaped comb-like structures have not been reported.

On the other hand, diluted magnetic semiconductors (DMS) have attracted much interest in recent years with the possibility to establish semiconductor spin electronics (spintronics).[171] Large bandgap semiconductors, including ZnO and GaN, have been

reported to be good host materials for spintronic devices with Curie temperature above room temperature.[172] Large magnetic circular dichroism was also observed for 3*d* transition-metal doped ZnO with strong *sp-d* exchange interactions.[172] Copper, different from other magnetic metal dopants (e.g., Mn, Co, etc),[173] is not ferromagnetic, and neither is Cu_2O nor CuO. However, Cu ions can be spin polarized in ZnO. The band gap for spin up and spin down of Cu-doped ZnO has 0.28 eV difference as calculated by Chien *et al.*[174] Previous works have demonstrated that Cu-doped ZnO film or powder can be ferromagnetic above room temperature.[175-177]

In this Chapter, we shall present the fabrication of a two-dimensional ZnO rafts-like structure with diamond-shaped cross sections by VPT method using copper as a catalyst. Investigation on these ZnO structures helps to understand the fundamental growth mechanism of wurtzite structures. Optical properties and ferromagnetism of these copper-doped ZnO will be discussed.

3.2 Experimental details

The ZnO microchains and microrafts were synthesized via VPT method using high-temperature tube furnace as has been briefed in Chapter 2. An empty furnace was preheated to 800°C first. Meanwhile, the mixture of ZnO and graphite powder (1:1) was placed at the end of a slender one-end sealed quartz tube. Five pieces of copper grids (400 meshes) were placed on a *p*-type silicon strip and inserted together into the small quartz tube at a downstream area. Then the small quartz tube was pushed into the standing-by furnace. The furnace was then heated from 800°C to 1100°C and maintained at 1100°C for 10 min. The silicon strip was in the temperature region ranging from 1000°C to 500°C

when the furnace was heated to 1100°C. Then the quartz tube was pulled out and slowly cooled down to room temperature. Yellowish products were found flourishingly growing from melted copper grids.

3.3 Results and discussions

3.3.1 Morphology of the microchains and microrafts

Figure 3.1 (a) shows a low magnification SEM image of the as-grown product, where a large area of raft-like microstructures can be seen on the copper grid. Figure 3.1 (b) is an enlarged image of a microraft. The width of the diamond-shaped microrods growing on these microrafts is ~2 μm to 3 μm, with lengths up to 20 μm. We also observed some chain-like microstructures with much shorter microrods, which are microrafts at their early growth stage. Figure 3.1 (c) shows several ZnO microchains found in the samples at relatively lower temperature region, with an enlarged image of single microchain shown in Figure 3.1 (d). Many evenly spaced diamond-shaped microbeads with width close to that of microrods, were growing from the surface of a nanobelt. As can be seen in Figure 3.1 (e), the microchains examined are originated from the same nucleus. The angles between adjacent nanobelts are 30°, 60°, or 120°, due to the six-fold symmetry of ZnO crystal. Our detailed SEM analysis revealed that, the microrods and microbeads growing on microrafts and microchains respectively, have rhomboidal cross section with small inner angles of 60° ± 1°, as indicated in Figure 3.1 (d). All the microchains and microrafts observed in our sample originated from relatively thick nanobelts, a typical one being
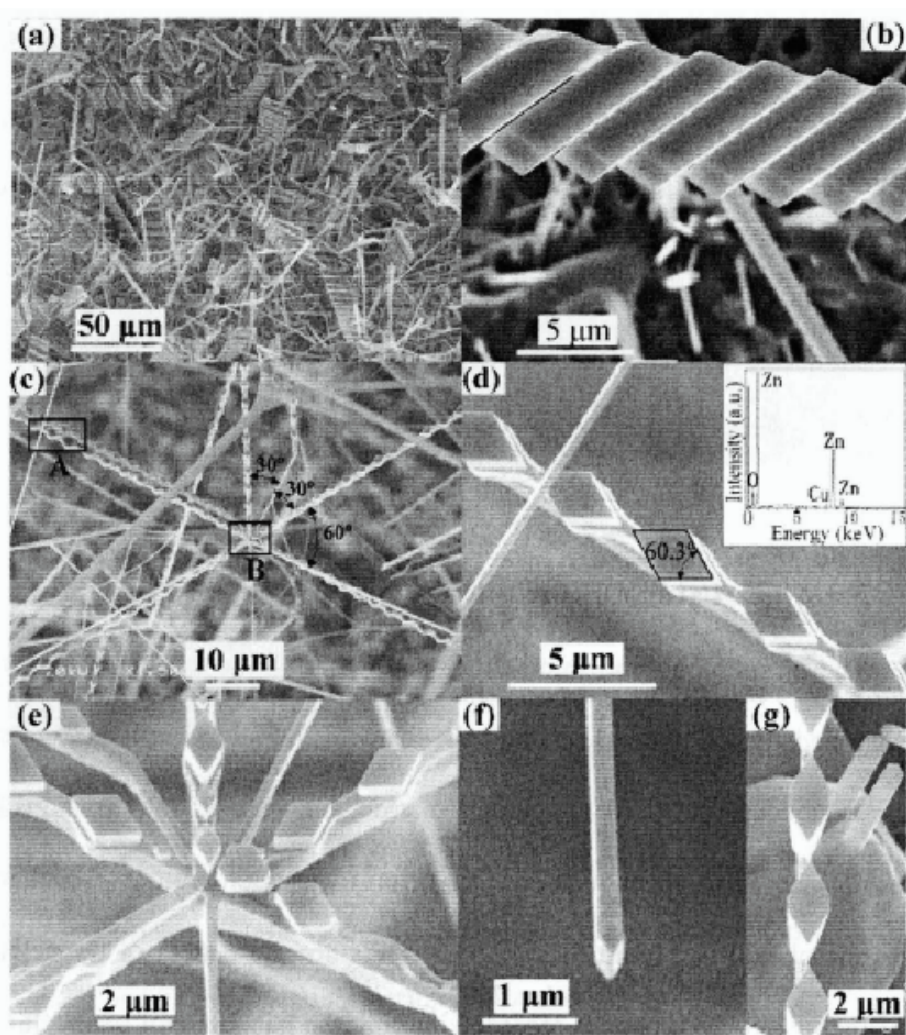
Figure 3.1 SEM images of: (a) Large area of microrafts growing on a copper grid;

(b) Single microraft of periodic structure; (c) A cluster of ZnO microchains. The

angles between adjacent microchains are 30 °, 60 °, or 120 ° as indicated.

(d, e) Higher-magnification SEM images of a single microchain and a microchain

joint corresponding to regions A and B shown in (c), respectively. The measured

inner angle of diamond cross section is indicated in (d). The inset in (d) is the

EDX result recorded from the structure shown in the main image. (f) Higher-

magnification SEM image of a thick nanobelt. (g) SEM image of microbeads with

irregular hexagonal shaped cross section obtained at a lower temperature region

showing the transition of microbead from hexagonal to diamond shape.

shown in Figure 3.1 (f). In comparison with the fully-grown diamond-shaped microbeads in Figure 3.1 (d), Figure 3.1 (g) shows several microbeads found further away from the source (lower growth temperature), which have irregular hexagonal shaped cross-sections with two $\{\bar{1}100\}$ facets yet to disappear. The EDX analysis conducted on a microchain shows that the atomic ratio of Zn: O is close to 1 and the copper content is about 1.6 at % [inset in Figure 3.1 (d)], suggesting that copper was doped into ZnO.

3.3.2 TEM study of the microchains

The morphology and microstructure of the microchains and microrafts were further examined by TEM to understand the growth of these unique structures. Figure 3.2 (a) shows a side view TEM image of a microchain. Figures 3.2 (b) and (c) shows the high-resolution TEM images with electron beam focused on region A (backbone nanobelt) and B (microbead) in Figure 3.2 (a). The insets are the results of the selected-area electron diffraction (SAED) pattern recorded on both the backbone of nanobelt (region A) and the edge of microbead (region B), respectively. The results confirm that the microchain is a single crystal with backbone growing along the $[0\,\bar{1}\,10]$ direction and microbead is growing along [0001] direction. From the literature, the branch of ZnO comb grows along [0001] direction while the ribbon grows along $[0\,\bar{1}\,10]$, $[2\,\bar{1}\,\bar{1}\,0]$ or [0001] direction.[155, 159, 178] The crystalline structure of microchain and microraft is in agreement with that of other types of ZnO combs that have been reported earlier in literature.[164] The calculated angle (60°) between the $(10\,\bar{1}\,0)$ and $(01\,\bar{1}\,0)$ surfaces of wurtzite ZnO crystal structure is consistent with the inner angle enclosed by these two surfaces observed in SEM.
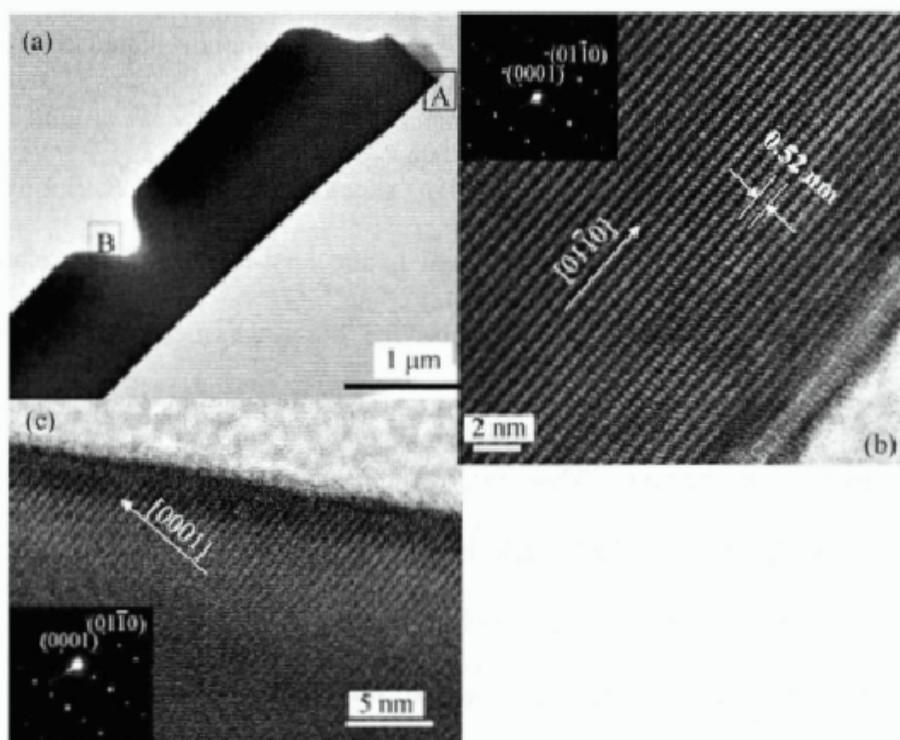
Figure 3.2 (a) Low-magnification TEM image of the side view of a microchain.

(b) High-resolution image of marked region A shown in (a) and its corresponding

SAED pattern (inset). (c) High magnification of the marked region B shown in (a)

and its corresponding electron diffraction pattern (inset).

3.3.3 Optical properties

Figure 3.3 (a) shows the Raman spectrum of the copper-doped microstructures. Raman spectra for doped and undoped ZnO films were discussed previously.[179, 180] The ZnO crystal has C_{6v} symmetry and shows six Raman-active phonon modes in the first-order spectrum at 101, 381, 407, 437, 574 and 583 cm^{-1} for the E_2 (low), A_1 (TO), E_2 (high), A_1 (LO) and E_1 (LO) mode of ZnO, respectively. It is a unique feature of ZnO that the LO signal is weak while the two-phonon signal is relatively strong.[181] The peak at

around 330 cm^{-1} corresponds to the second-order phonon signal of A_1 (TO). There are other two anomalous first-order Raman modes of doped ZnO around 275 and 580 cm^{-1} corresponding to B_1 (low) and B_1 (high) silent modes.[180] The B_1 (high) mode appears in the Raman spectrum can be attributed to the host-lattice defects related to the copper doping. These results further confirm that the ZnO microstructures are composed of hexagonal ZnO as the E_2 (high) mode corresponds to band characteristics of the hexagonal wurtzite phase. These microstructures are of good crystal quality since the peak corresponding to E_2 (high) mode is relatively strong and sharp, compared to the peak around 580 cm^{-1} which is related to the defects in ZnO.

The PL spectrum was recorded at room temperature using the same Renishaw microspectrometer excited by the 325 nm line of a He-Cd laser. Figure 3.3 (b) shows the emission spectrum of the copper-doped microstructures (solid line) and pure ZnO nanostructure (dotted line). It is well known that ZnO is a wide direct-gap (3.37 eV) II-VI semiconductor with large exciton binding energy of 60 meV at room temperature.[182] However, only a broad green band appears, with a contrast sample showing strong UV emission (ZnO powder). This green band would come from multiple energy levels in the forbidden band due to copper doping and oxygen vacancies.[183] Compared with pure ZnO nanostructures, the increased amount of deep-level energy related defects could be the center of radiative or non-radiative recombination centers that "quench" the UV emission of these Cu-doped microstructures.
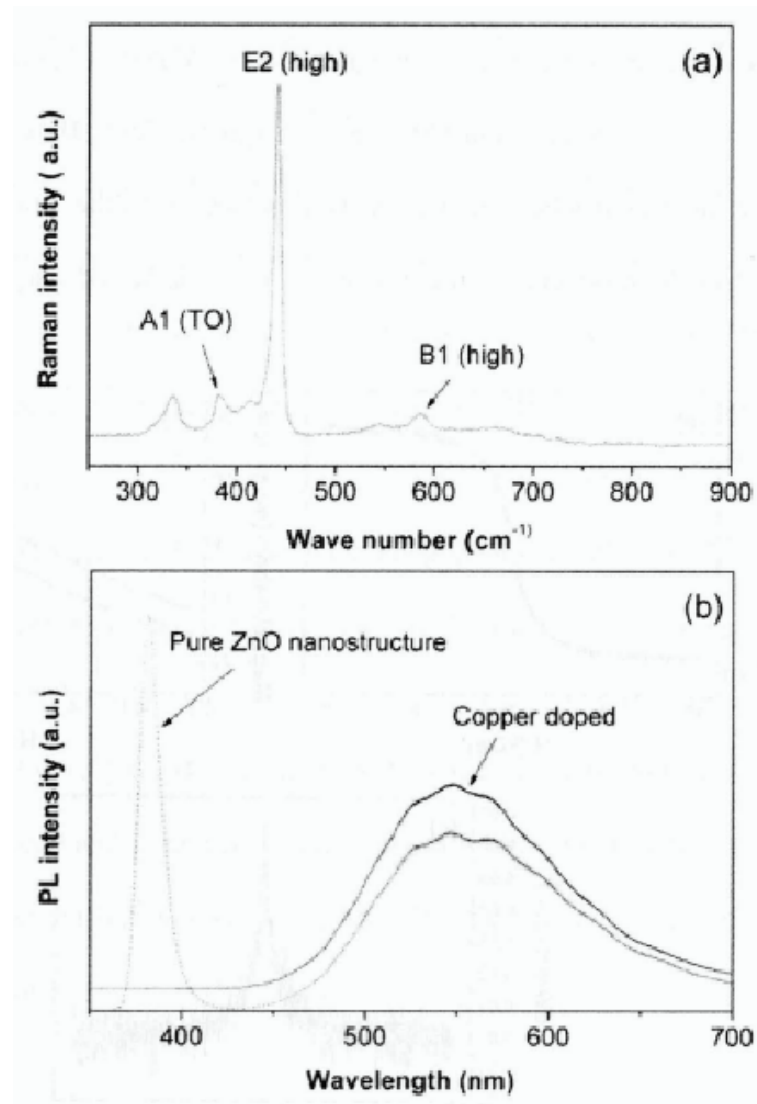
Figure 3.3 (a) Raman spectrum of as-deposited ZnO microstructures at room

temperature using 514 nm line as the excitation source. (b) 325 nm line PL

spectrum of as-deposited ZnO microstructures (solid line) and a pure ZnO powder

(dotted line) at room temperature using as the excitation source.

3.3.4 Magnetic properties

Ferromagnetic properties of copper-doped ZnO microstructures were measured using high sensitivity alternating gradient magnetometer (AGM) at room temperature. Figure 3.4 (a) shows the magnetization (**M**) versus magnetic field (**H**) characteristics at room temperature, measured when the applied **H** was parallel to the silicon substrate that was used to collect the products. Figure 3.4 (b) shows an enlarged magnetic loop of (a), and
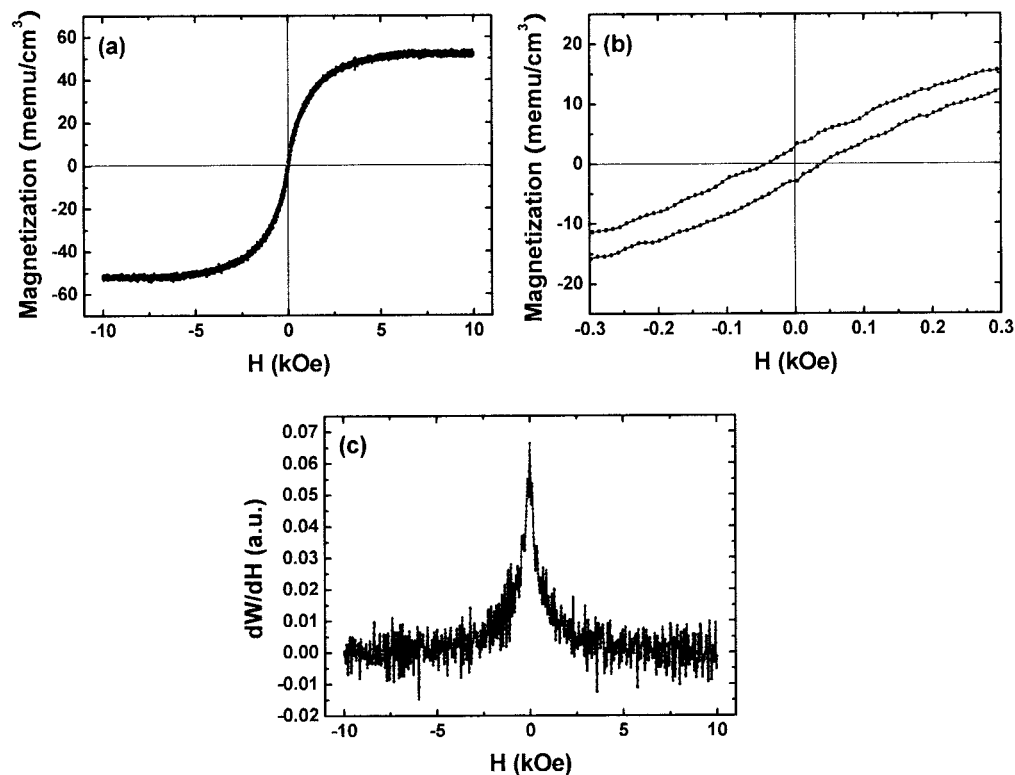
Figure 3.4 (a) Magnetization M versus applied magnetic field H curve detected at room temperature. The enlarged hysteresis loop is shown in (b) and the derivative curve (dM/dH) is shown in (c). The two CGS units, emu and Oe, are electromagnetic and magnetic units, and the conversion factors to SI units (both are A/m) are 10^{-3} and $4\pi \times 10^{3}$, respectively.

the derivative curve of the decreasing-field sweep is also illustrated, as shown in Figure 3.4 (c). The saturation magnetization M_s of the copper-doped sample is estimated to be 53 memu/cm^3 from the **M-H** curve. The saturation field is about 7 kOe, and the coercive field (H_c) is about 40 Oe, as can be seen in Figure 3.4 (b). The M_s is almost ten times lower than that of copper-doped ZnO thin film reported by Buchholz *et al.,*[176] and approximately 400 times higher than that of copper-doped ZnO powders reported by Lee *et al.,*[177] which were both measured at room temperature. The estimated magnetic moment (0.0043μ_B/Cu atom) is about 10 and 100 times smaller than that reported by Herng *et al.*[175] and Buchholz *et al.,*[176] respectively. The differences might be attributed to doping concentration, magnetic coupling and inhomogeneous distribution of copper ions. The calculated squareness of the hysteresis loop is 0.06 and its switching field distribution (SFD) is 0.068. SFD is a ratio of the full width at half maximum of the differentiated curve [Figure 3.4 (c)] to H_c. A small SFD indicates a narrow and stable switching transition produced and is related to the microstructure and chemical inhomogeneities in the material. Generally, materials with high H_c and small SFD are desirable for high-density recording.

3.3.5 Growth mechanism

In accordance with the TEM and SEM data, here we propose a possible growth mechanism as shown in Figure 3.5 (a)-(c) with simple schematic depictions of a microchain and a microraft. The growth directions of the microstructure are indicated by arrows. Figure 3.5 (a) shows a thick quadrate nanobelt according to the SEM image observed in Figure 3.5 (f). Figure 3.5 (b) indicates the growth of a microchain observed in
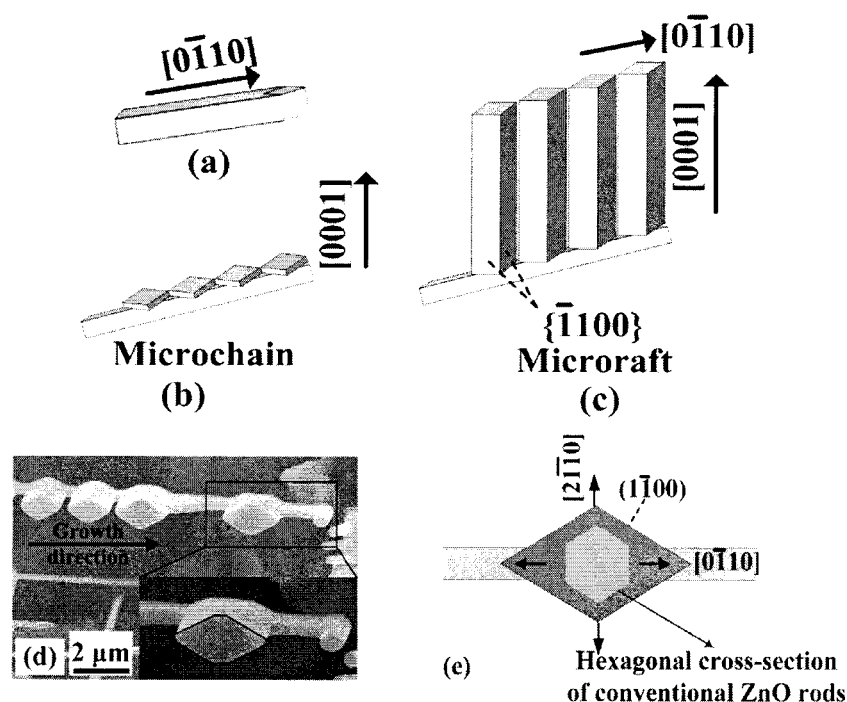
Figure 3.5 (a-c) Proposed growth diagram and simple models of thick nanobelt, microchain and microraft structures, respectively. (d) SEM image of a microchain at a lower temperature region showing. The microbeads away from the belt tip are closer to diamond and a microbead is nucleating from the tip of the belt.

(e) Schematic depiction showing the relationship between diamond and hexagonal.

Figure 3.1 (c). It is known that wurtzite ZnO has three fast growth directions in $[0\bar{1}10]$, $[2\bar{1}\bar{1}0]$ and $[0001]$, which are perpendicular to each other. Therefore, the microbeads could be formed by growing along $[0001]$ direction of ZnO at the tip of a $[0\bar{1}10]$ growing ZnO belt, as can be seen in Figure 3.5 (c). The formation of a microraft results from the fast growth of microbeads along $[0001]$ direction, shown in Figure 3.1 (b). From the TEM analysis, both the diamond and hexagonal-shapedZnO are of 6-fold wurtzite structure, and

49

grows preferentially along the [0001] direction. However, two surfaces from the $\{1\bar{1}00\}$ group are missing in the diamond-shaped microbeads. To explain this difference, Figure 3.5 (e) shows the relationship between the rhomboidal and hexagonal shapes due to the fast growth of the $\pm(01\bar{1}0)$ surfaces along the same growth direction of nanobelt backbone, while the fast growth along $[2\bar{1}\bar{1}0]$ direction is indicated by arrows. It is known that crystal facets with faster growth rate disappear easily, and the crystal facets with slower growth rate remain. The growth rate of ZnO in $<0\bar{1}10>$ directions is faster than in $<2\bar{1}\bar{1}0>$ directions in our experiment. Therefore, only $\pm(10\bar{1}0)$ and $\pm(1\bar{1}00)$ facets remain and form diamond-shaped cross–section at substrates. This growth mechanism can be inferred from Figure 3.1 (g) and Figure 3.5 (d), where the microbeads are in the middle of the hexagonal to diamond transformation. These microrods, therefore, can be considered as one third of hexagonal microrods and also a reduced form of the hexagonal structure in which two parallel facets disappear.

3.4 Summary

In summary, we fabricated diamond-shaped ZnO microchains and microrafts based on wurtzite ZnO. The backbone of these structures extended along $[0\bar{1}10]$ direction and the side branch grew in [0001] direction. Raman and EDX measurements revealed that these microstructures are copper-doped. UV-blue luminescence quenching has been observed due to the copper doping into ZnO. The microstructures showed a clear ferromagnetic behavior with a high H_c and small SFD value, which may have potential applications in

data storage. We postulate that the formation of diamond-shaped ZnO is due to the fast

growth of two parallel planes in $<0\bar{1}10>$ directions along the growth of the backbone.

Chapter 4 FABRICATION OF

RESISTOR-SHAPED ZnO NANOWIRES

4.1 Introduction

VPT appears as the most commonly used method for growing oxide nanostructures of various morphologies and aspect ratios. To some extent, the shape- and size-control of the nanostructures is achieved by controlling the growth parameters, such as carrier gas flow rate, the partial pressure of reactive gases, the vapor flow direction, as well as the temperature and the choice of substrate materials.[153, 162] In addition, the formation of nuclei and subsequent growth behavior can be largely influenced by the presence of metals, metal ions and water.[37, 160, 184] For instance, ring-shaped nanostructure have been fabricated by adding indium and/or lithium to the precursors.[37] Triboulet *et al.*[184] have reported the growth of ZnO single crystals using water as growth 'activator'. In a recent study by Huang *et al.*,[160] $ZnCu_2$ alloy was used as Zn source, with water vapor introduced into the system by carrier gas. They found that Cu and water vapor resulted in a modified growth behavior of ZnO nanobelts.

As presented in Chapter 3, we have fabricated Cu-doped microchains and microrafts on Cu grids. In Chapter 4, we will continue to study the effect of Cu and water in formation of ZnO nanostructures. We introduce Cu into the growth system by using pure Cu wires. Water is also added and the source of ZnO and graphite are doubled in weight to increase the vapor pressure. The morphology and structural characteristics and a growth

mechanism are discussed. This new ZnO morphology, analog to the shape of electrical resistors connected in series is characterized by an abrupt diameter change at the junction, which is similar to the step-shaped Bi NWs,[185] (Ga, Mn)As NWs,[186] and Y-shaped CNTs[187] reported previously.

4.2 Experimental details

The resistor-shaped ZnO NWs (RSNWs) were synthesized via a VPT method using a high-temperature tube furnace. The mixture of ZnO and graphite power (0.5 g, 1:1 in wt %) was placed at the end of a slender one-end sealed quartz tube. One piece of a 10 cm long copper wire (0.2 mm in diameter) placed on a wet silicon strip was inserted into this slender quartz tube at a downstream area. A volume of 0.2 ml water was intentionally spread on the silicon strip. The furnace was then heated from room temperature to 1090°C at a rate of 30°C/min. Once the temperature reached 650°C, the quartz tube was inserted into the furnace. When the source temperature reached 1070°C, a constant flow of vapor in the quartz tube could be observed. The quartz tube was then pulled out and cooled down to room temperature when the temperature reached 1090°C. The Si substrate and copper wire were covered with a silk-like powder near the open-end of the quartz tube. To study the effect of water and copper on the nanostructure morphologies, the experiment was then repeated successively in the absence of (1) water, (2) copper wire, and (3) both water and copper wire, respectively.

4.3 Results and discussion

4.3.1 XRD analysis

Figure 4.1 shows the powder XRD pattern of the as-synthesized product. All as-labeled peaks match well the hexagonal ZnO nanostructure with lattice constants of $a = 3.249$ Å and $c = 5.205$ Å. No diffraction peak originated from copper, silicon (used as substrate) or any of their compounds can be found in the XRD data. Further examination by EDX shows that the atomic ratio of O:Zn is close to 1. The copper signal is below the detection limit of EDX, which indicates that concentration of copper is too low to be detected.

4.3.2 Morphology and crystal structure of the RSNWs

Figure 4.2 (a), (b) and (c) show SEM images of the as-synthesized nanostructures at various magnifications. Abundant RSNWs are clearly observed, which consist of a
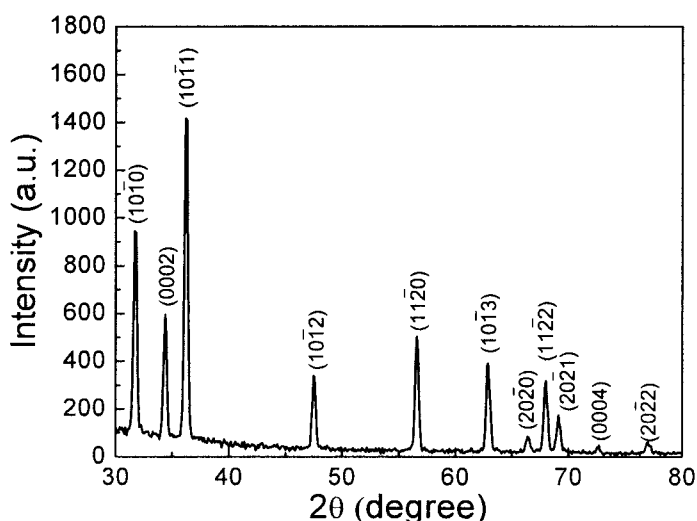
Figure 4.1 XRD pattern of the as-prepared ZnO RSNWs.
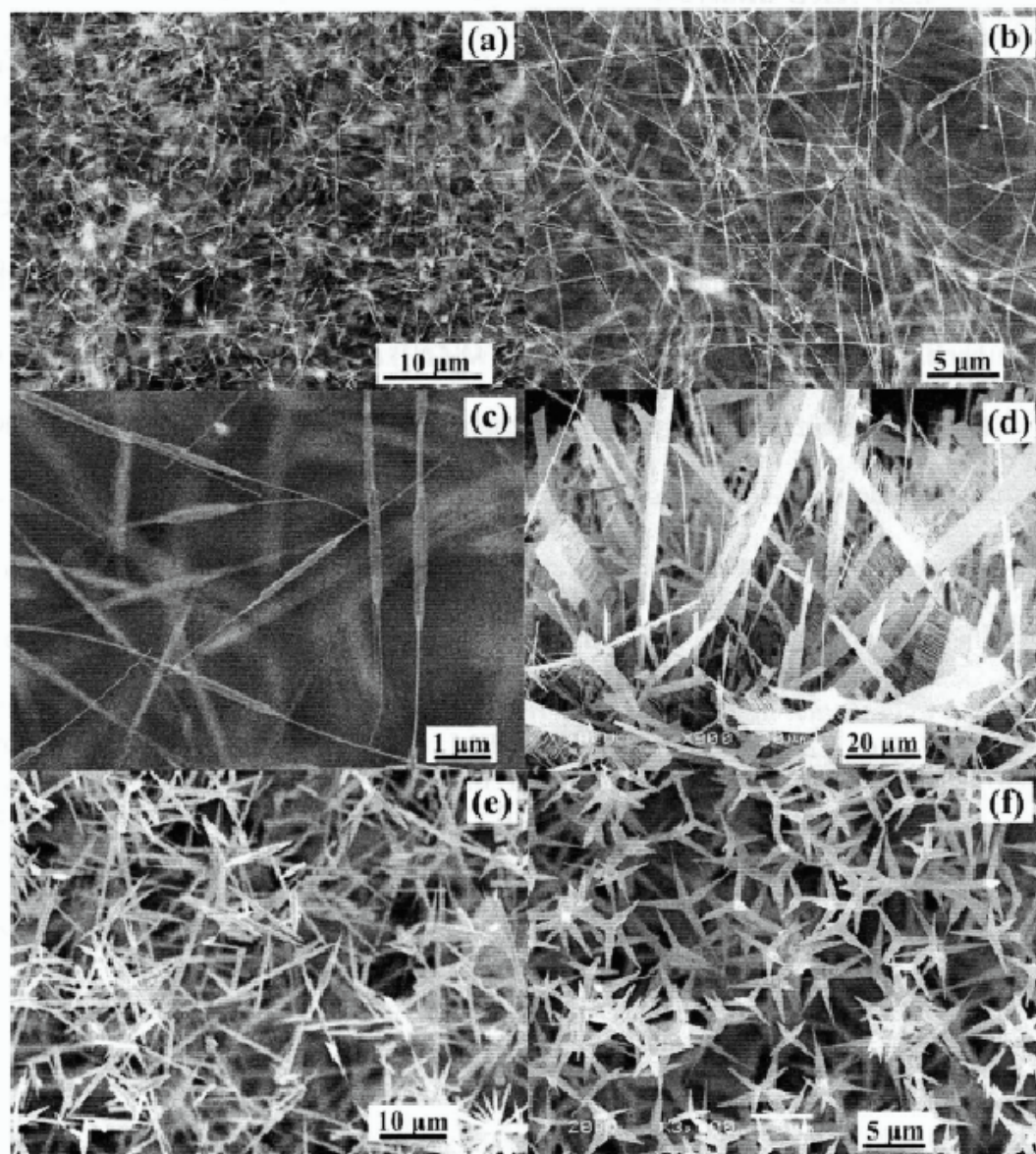
Figure 4.2 (a-c) SEM images of ZnO RSNWs fabricated using both water and

Cu,at various magnifications. (d-f) SEM images of similar structures fabricated

using: (d) only Cu; (e) only water (no Cu); (f) without both water and Cu,

respectively

thick NR in the center with diameter ranging from 150 nm to 200 nm, and length of about 2 μm. Fine NWs grow from both ends of the thick NRs. The length of NWs ranges from tens of nanometers up to tens of micrometers, and their diameter is only about 10 to 20 nm. In comparison, the as-grown product (1) without water, (2) without copper wire, and (3) without both are shown in Figure 4.2 (d), (e) and (f), respectively. It can be noticed that in these latter three cases no RSNWs grow but (1) NCBs growing only on Cu wire, (2) powder of submicron needle-like rods, and (3) powder of submicron tetrapods are all found in these samples. It is clear that Cu itself (without water) does not induce the growth of RSNWs, and, in the presence of both water and Cu, the density of RNNWs $(2.56 \times 10^{16}$ mm^3) and their morphology is close to that of needle-like rods $(2.59 \times 10^{16}$ mm^3), whereas the diameter is reduced by around ten times.

It is noted that many RSNWs are connected to each other forming "in-series" structures as shown in Figure 4.3 (a). The enlarged "in-series" structures are clearly shown by TEM images in Figure 4.3 (b) and (c). Their diameter is on average around 200 nm for the rods and around 10 to 20 nm for the wires, with a sharp reduction in diameter at the NR-NW junctions. In-depth investigation revealed that they were formed by attachment of several RSNWs. The TEM caption images inserted in Figure 4.3 (b) and (c) taken from the dot-circled parts at the NW junction between two RSNWs present a clear evidence of the in-series connection of the RSNWs.

In Figure 4.3 (b) and (c) the grain boundaries of the RSNWs can be observed from the contrast near the center of the thick NRs. Typical bright field (BF) and dark field (DF) TEM images taken from the rectangle-selected area of the thick NR [Figure 4.3 (b)] are shown in Figure 4.3 (d) and (e), respectively. The grain boundary was further studied by
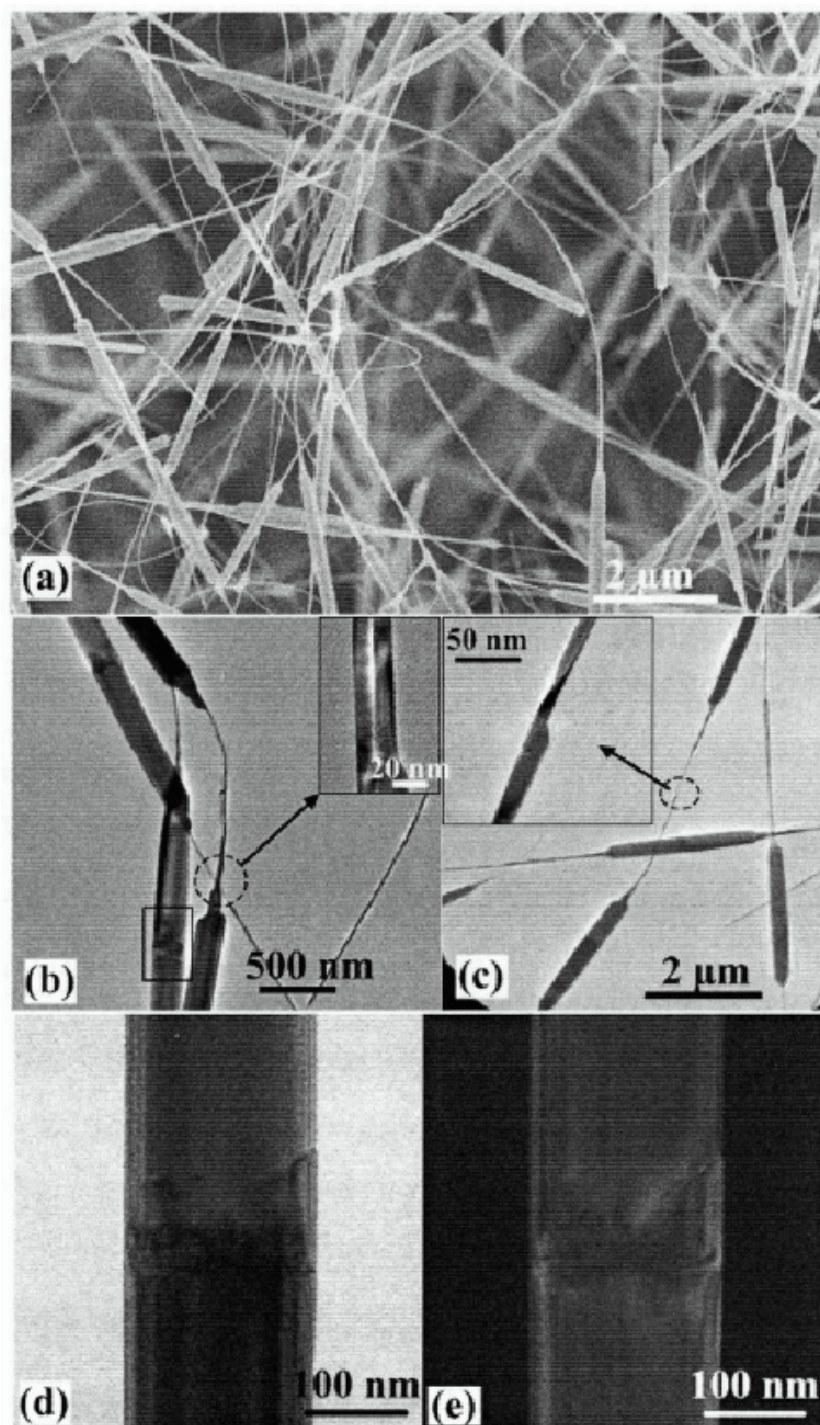
Figure 4.3 (a) SEM images of "in-series" RSNWs. (b and c) TEM images of some

series of RSNWs inserted with the enlarged connect sites of the NWs between

two RSNWs. (d) BF and (e) DF TEM images of rectangle-selected region in (b).
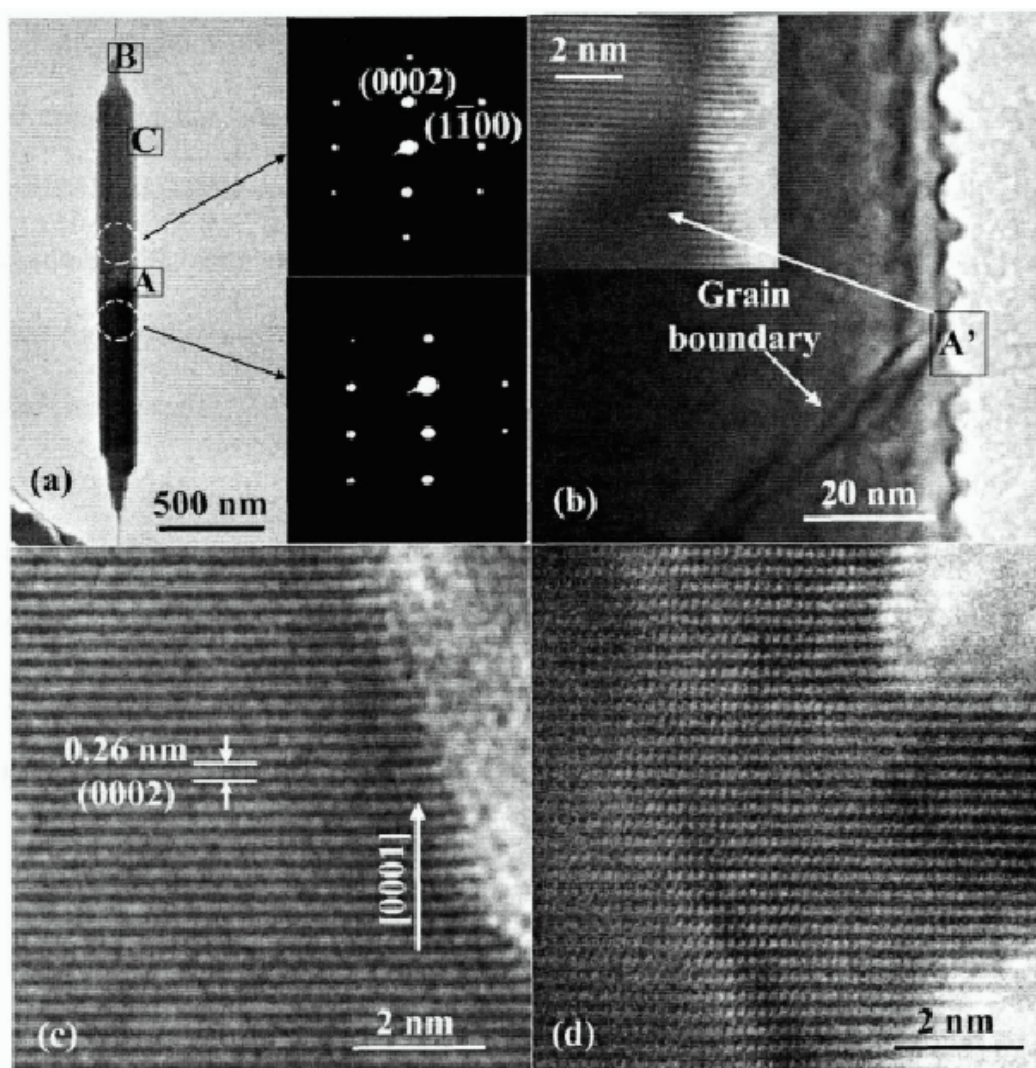
Figure 4.4 (a) Typical TEM image of a ZnO RSNW inserted with the SAED

patterns taken from the sides near the grain boundary. (b) Higher-magnification

TEM image of region A in (a) inserted with the corresponding HRTEM image.

(c and d) HRTEM images recorded from region B and C labeled in (a).

HRTEM. Figure 4.4 (a) shows a low-magnification TEM image of a single RSNW and

the SAED patterns taken from the circled regions near the grain boundary to examine the

crystal structure of the thick NRs. It is worth mentioning that, the SAED patterns shown

in Figure 4.4 (a) were obtained without tilting the sample. Both SAED patterns are the

same except a relative intensity difference of diffraction spots, indicating the same crystal orientation of these two grains. Figure 4.4 (b) shows a higher-magnification TEM image recorded from the grain boundary at region A in Figure 4.4 (a), and the inset is the corresponding HRTEM. A grain boundary can be clearly seen. Figure 4.4 (c) and (d) show the HRTEM images taken from region B (near NR-NW junction) and region C (thick NR) in Figure 4.4 (a), respectively. All the HRTEMs show clear lattice fringes indicating the RSNWs are formed from two single-crystallites with a grain boundary at region A [Figure 4.4 (a)] separating them. As shown in Figure 4.4 (c), the spacing of 0.26 nm between adjacent lattice planes corresponds to the d-spacing of (0002) planes, indicating <0001> as the growth direction for the RSNWs. It is worth mentioning that the surface of the nanostructure is rough [Figure 4.4 (b)], which might be due to electron beam irradiation in TEM.[188]
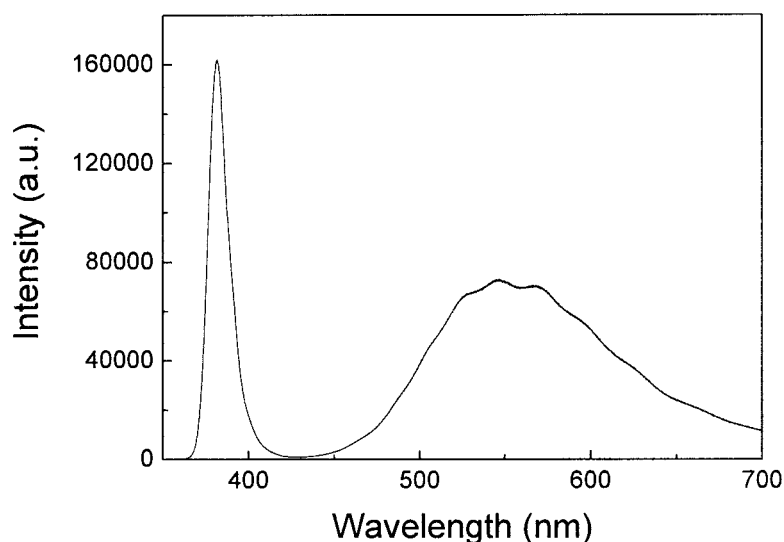
Figure 4.5 PL spectra of the ZnO RSNWs grown on a silicon substrate.

4.3.3 Optical properties of RSNWs

As shown in Figure 4.5, the PL spectra exhibit relative sharp UV emission peaked at around 381 nm while a much boarder emission (FWHM = 120 nm, 450-700 nm) is centered at around 546 nm. The UV band emission of ZnO has been attributed to the free exciton emission at the near-band edge.[123] The visible emission might be due to deep-level transition caused by defects, in particular surface states[154] and oxygen vacancies.[128, 129] The FWHM of the UV emission was calculated to be around 15 nm, which is much smaller than that of bulk ZnO powders (32 nm) but comparable to those of ZnO NWs (20 nm).[104, 136] The absence of Cu element shown by XRD is confirmed by the PL result since the UV emission is not quenched and the ratio of UV-to-visible emission densities is comparable to that of pure ZnO nanostructures.[133]

4.3.4 Growth mechanism

According to the electron microscopy observations and analysis, a possible growth mechanism is proposed by considering the $\pm (0001)$ polar surfaces of ZnO. A corresponding schematic diagram is displayed in Figure 4.6. The formation of the RSNWs can be depicted as a three-stage process, as illustrated in Figure 4.6 (a-c). In Figure 4.6 (a), growth species of ZnO_x and Zn are formed due to the thermal reactions of ZnO and graphite, and the growth of ZnO 1D nuclei and NRs involves adsorption/desorption of growth species. Following the argument proposed by Huang *et al.*,[160] the addition of Cu and water can control the supply of Zn and oxygen, and thus modify the crystal growth kinetics. Our present work supports such assumptions. The following chemical reactions between water vapor and growth species at high temperature could be:[160]

$$Zn(g) + xH_2O(g) \Leftrightarrow ZnO_x(g) + xH_2(g), \qquad (4.1)$$

$$ZnO_x(g) + xH_2O(g) \Leftrightarrow Zn(g) + xH_2(g) + xO_2(g), \qquad (4.2)$$

$$ZnO_x(g) + xH_2O(g) \Leftrightarrow xZn(OH)_2. \qquad (4.3)$$
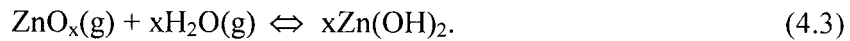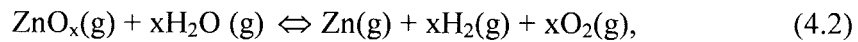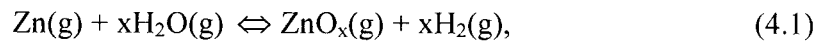
where water is a source of O_2 and H_2. The chemical reactions (2.1)-(2.3) between water vapor and growth species probably confine the growth of ZnO nuclei along the c-axis by lowering the surface energy of {0001}.[189] On the other hand, according to Haugsrud *et al*, and Fujikawa, *et al*.,[190, 191] Cu can be easily oxidized by water vapor at high temperature according to the following reactions,

$$2Cu + H_2O (g) \rightarrow Cu_2O + H_2 (g), \qquad (4.4)$$

$$Cu_2O + H_2O (g) \Leftrightarrow CuO + H_2 (g). \qquad (4.5)$$
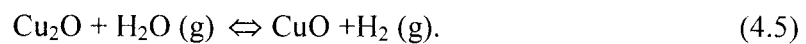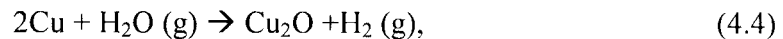
Therefore, production of hydrogen from water vapor can be enhanced. More H_2 can increase the desorption speed of growth species on the growing surface through reductive reactions, and consequently reduce the growth speed, in comparison with the case where only water is presents.

In Figure 4.6 (b), the formation of the paired-crystal structure can be understood as due to electrostatic interactions at both ends of NRs with sharp tips. It is well known that the chemically active facet (0001) of wurtzite structured ZnO is Zn^{2+}-rich and the inert facet (000$\bar{1}$) is O^{2-}-rich. When the (0001) facet comes close to the (000$\bar{1}$) facet, they will be connected due to mutual electrostatic attraction with well-matched lattice.[88] Although the purity of RSNWs is high [Figure 4.1 (b)], we can still find some needle-like NRs in TEM, which have just half of the length of the thick NRs. We can also find a small amount of paired-NRs with two grains connected in a random orientation (TEM images
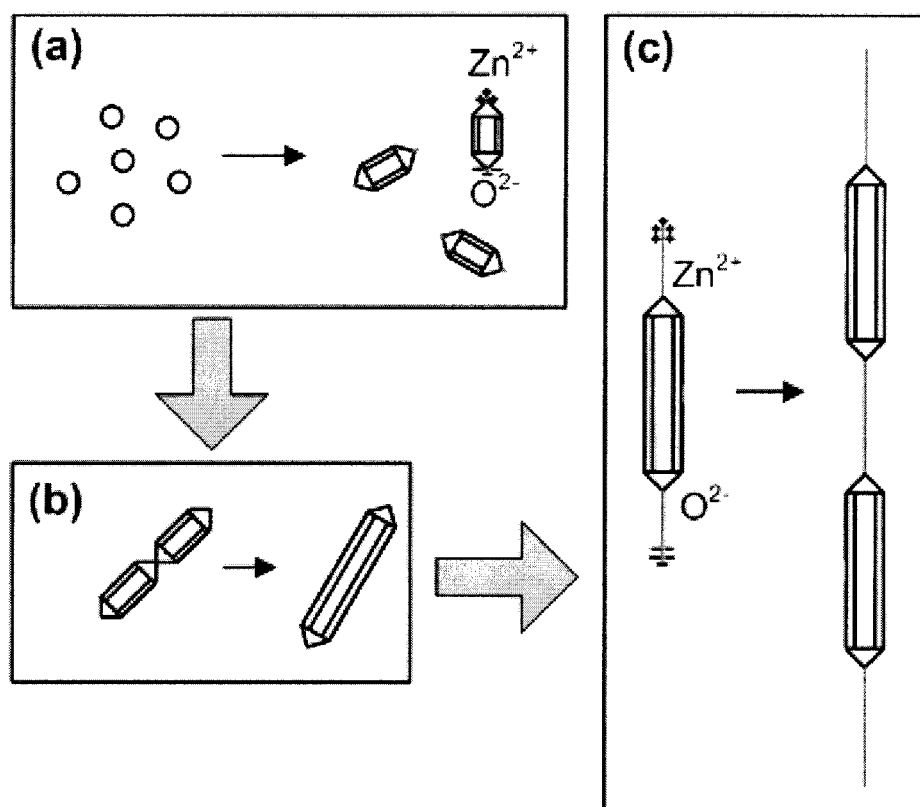
Figure 4.6 Schematic diagram of the possible formation process of ZnO RSNWs,

and "in-series" RSNWs with a polar-surface induced growth model,

(a) growth of 1D nuclei and NRs, (b) the NRs are attracted by spontaneous

electrostatic attraction and form paired-crystalline structure, and (c) growth of

fine NWs from both ends of the NRs and the formation of the "in-series" RSNWs.

not shown here). Such observations are in agreement with the proposed growth mechanism and further support strengthen its validity.

Figure 4.6 (c) shows the formation of single and "in-series" RSNWs. The diameter of the NWs decreases drastically at this stage, due to the substantial decrease in the vapor pressure. Similar to Figure 4.6 (b), the floating RSNWs attract each other and connected together to form RSNWs "in-series". It is worth mentioning that fine NWs grow in both

$\pm[0001]$ directions from thick NRs and the growth rates in both directions have almost equal values.

4.4 Summary

In summary, a novel ZnO nanostructure, *ad hoc* demonstrated as the "resistor-shaped" NW, has been synthesized using a vapor phase transport method in the presence of water and Cu, which adjusted the growth kinetics, enabling therefore the growth of such a unique complex morphology. The RSNWs are built up by thick NRs and fine NWs, morphologically bridged with abrupt junctions, and of wurtzite paired-crystalline nanostructures. The formation of paired-crystalline structure and series RSNWs are attributed to the electrostatic forces induced by the spontaneous polarization of ZnO $\pm(0001)$ polar facets at different growth stages. The RSNWs are potentially useful for building and connecting electrical nanodevices as well as building blocks in the fabrication of functionalized interfaces.

Chapter 5 SURFACE MODIFICATION

OF ZnO NANOSTRUCTURES I-

QUENCHING OF SURFACE-EXCITON

EMISSION

5.1 Introduction

In Chapter 3 and 4, we presented two different morphologies of ZnO by VPT method. For a nanometer-sized system, the PL becomes more surface-related than that for bulk ZnO crystal.[126, 133] The PL spectra of most of our ZnO nanostructures have a weak UV band compared with the broad and strong visible band due to a high surface-to-volume ratio compared to bulk material. It was observed recently that in a ZnO NW/nanowall system, a prominent near-band-edge PL peak at around 3.367 eV increasingly contributes to the optical properties of individual NWs with the decreasing of diameter at low temperature,[138] which was assigned to the recombination of surface excitons (SXs) by Grabowska *et al.*,[126] who also indicated that, in order to realize nanostructured optoelectronic devices at room temperature, the SXs need to be eliminated. The dynamics of this SX emission was further investigated by Wischmeier *et al.*,[139] who suggested that SXs originated from a broad energy distribution of near-surface states.

On the other hand, PIII is a well developed surface modification technique.[81-84] It is a simple, non-line-of-sight process, as opposed to conventional beamline ion implantation; non-planar samples can be implanted with good conformality and uniformity without special sample manipulation. During PIII, the substrate is immersed in plasma and negative voltage pulses can be applied to implant ions from the plasma to the surfaces. The modification depth can be well controlled by the bias voltage, which is suitable for surface modification of thin films and nanostructures with complicate morphologies.[81, 85] Current research of the PIII is focused on modification of polymer and diamond-like carbon film, and impurity doping, etc.[82, 83, 86, 87] However, the surface modification of nanostructures by PIII has been much less investigated. In this Chapter, we shall report an effective quenching of ZnO SXs by PIII modification, which provides us with a powerful tool to overcome the problem associated with increased surface area (reduced dimension).

5.2 Experimental details

5.2.1 Growth of ZnO nanocombs

The growth of ZnO nanocombs (NCBs) was carried out in a horizontal tube furnace by VPT method. The growth mechanism follows a typical VLS mechanism. Firstly, 2 nm Au was coated on the cleaned substrate by sputtering. Then, pure ZnO and graphite powder (1:1 in wt %) were grounded together and loaded into a small quartz tube with an inner diameter of 20 mm. The substrate (1×2 cm) was placed in the downstream region of source with a separation of ~200 mm between the source and the substrate. The small quartz tube was then inserted into a furnace at 950°C for 30 min under a flow of 100 sccm

Ar and 10 sccm O_2. The pressure inside the furnace was maintained at 0.7 Torr throughout the experiment. After evaporation and deposition the quartz tube was drawn out from the furnace immediately and cooled down to room temperature. We found that the Si substrate was covered by a thin layer of uniform grayish film.

5.2.2 Surface modification by Ti-PIII

The NCB was chosen because of its large surface area. The as-grown products were then directly treated with Ti-PIII.[87, 192] Prior to the treatment, a base pressure of 3×10^{-6} Torr was obtained. The pressure was kept at 8×10^{-5} Torr with 8 sccm Ar flow during PIII. Negative pulse voltage of 0 and 5 kV was applied to the substrate holder for 2 min. The ion dose was estimated to be $\sim 1 \times 10^{13}$ ions/cm^2 upon 5 kV bias. The substrate temperature has been monitored to be below 100°C.

5.3 Results and discussions

5.3.1 Morphology and chemical analysis of the NCBs

Figure 5.1 (a) shows the typical morphology of the ZnO NCBs. There was no noticeable change in the morphology by SEM analysis before and after Ti-PIII. In comparison to the diameter of NCB fingers (~100 nm), the PIII in our experiments only modified the shallow surface of ZnO NCBs. In fact, the implant depth of Ti ions into the ZnO crystal is 0.4 and 4.5 nm for 0 and 5 kV bias voltages, respectively, as calculated with the SRIM.[148] Figure 5.1 (b) shows the EDX spectrum of the ZnO nanostructure after Ti-PIII at a bias voltage of 0 kV for 2 min, where Zn, O, and Ti peaks can be clearly

observed in the spectrum. The Ti:Zn:O ratio after 0 kV PIII is estimated to be 0.005:1:1.02 from the EDX spectrum by quantitative analysis, and the result is similar for 5 kV Ti-PIII. For comparison, the Zn:O ratio before PIII was 1:1.03. It is worth mentioning that the X-ray in EDX measurement penetrates in depth 1-2 μm, therefore the quantitative analysis obtained from EDX represents the bulk characteristics of the NCBs. From XPS surface analysis (not shown here), the Zn:O ratio of as-grown ZnO resulted to be 1:0.495, indicating a Zn-rich surface. After a 0 kV Ti ion treatment, the ZnO surface becomes Ti rich, with a Ti:Zn:O ratio of 3.65:1:7.68, indicating significant changes in the surface chemical composition. However, as the bias voltage rises above 5 kV, the Ti signal was below the detection limit of XPS measurement, which is due to increased implantation depth of Ti, in agreement with the SRIM simulation.
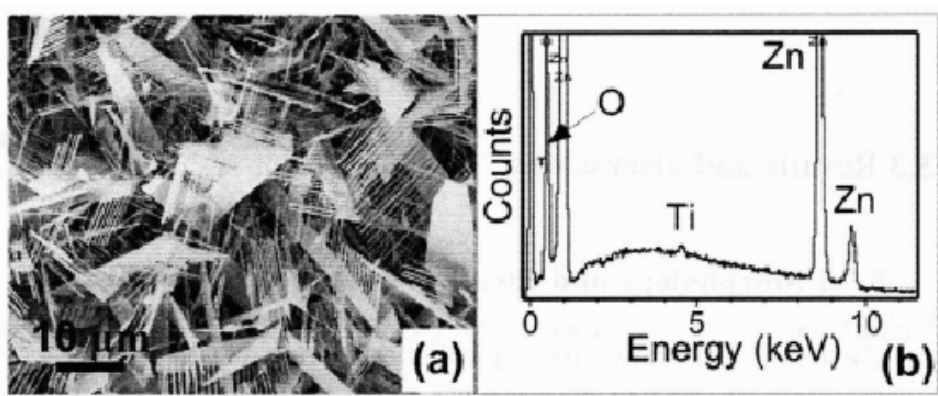
Figure 5.1 (a) SEM image of the ZnO nanostructures grown on Si substrate.

(b) EDX result of NCB after 0 kV Ti-PIII.

5.3.2 TEM analysis of the NCB surface after PIII

Figure 5.2 (a) and (b) show the typical TEM images of ZnO comb fingers after 0 and 5 kV Ti-PIII, respectively. The insets are corresponding SAED patterns. Figure 5.2 (d) and (e) are the HRTEM images corresponding to the areas selected by the rectangles in Figure 5.2 (a) and (b), respectively, in comparison with the HRTEM image of the as-grown ZnO comb fingers in Figure 5.2 (c). All the comb fingers observed in TEM are growing along the [0001] direction, which is consistent with our proposed growth model of ZnO combs reported in the literature.[164] No visible line or planar defects can be seen from the HRTEM image of the as-grown ZnO comb fingers [Figure 5.2 (c)]. The d-spacing of 0.52 nm corresponds to the lattice spacing of (0001) planes of wurtzite ZnO. After the 0 kV Ti ion treatment (without bias voltage), the surface of the NW is covered by a discontinuous layer less than 3 nm thick [Figure 5.2 (d)]. This ultra-thin amorphous layer is formed by Ti ions that are both deposited and superficially implanted onto the ZnO surface with a typical ion energy of 20-150 eV when no bias voltage is applied,[192] in agreement with the XPS measurement results. Careful examination of this ultra-thin coating [Figure 5.2 (d)] shows that it contains some nanocrystals with the d-spacing of 0.216 nm which matches that of (111) planes of rutile TiO_2. Figure 5.2 (e) shows the HRTEM of the ZnO surface after 5 kV ion treatment. The Ti ions are completely implanted into ZnO crystals and no Ti-related coating layer or new crystallite phases such as TiO_2 could be found. From our experiments, ZnO nanostructures treated under 2-5 kV bias showed similar HRTEM images as that shown in Figure 5.2 (e). The contrast of inhomogeneous regions in Figure 5.2 (b) and (e) increases with the applied negative bias voltage, indicating an increased implantation dose of Ti ions(most likely at interstitial sites of ZnO) and lattice defects.[193]
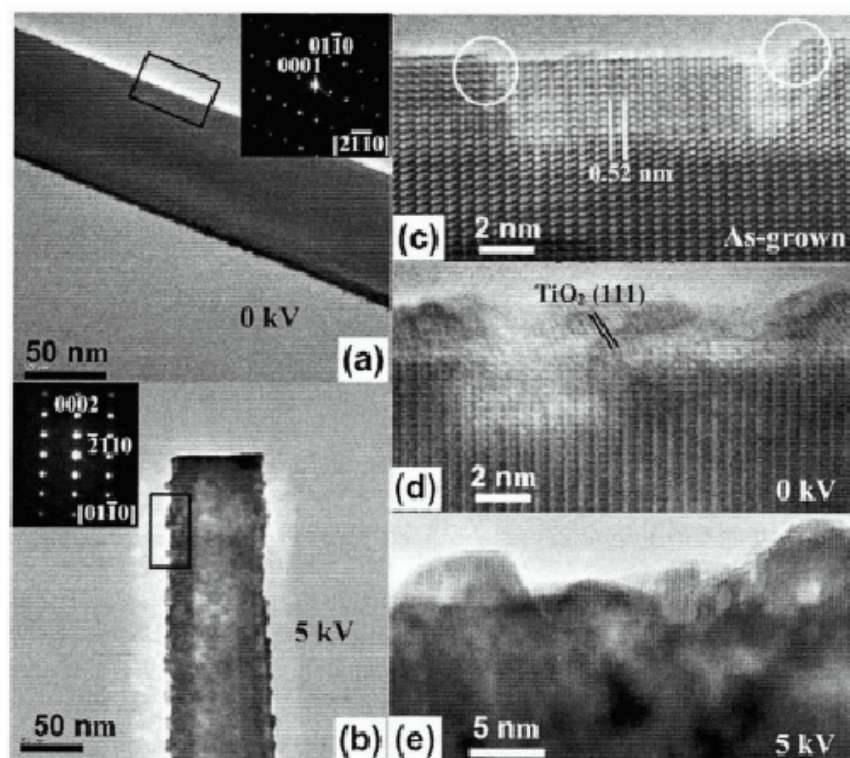
Figure 5.2 (a) and (b) show typical low-magnification TEM images of ZnO comb

fingers after 0 and 5 kV Ti-PIII, respectively. Insets are the corresponding SAED

patterns. (c) HRTEM images of ZnO comb fingers before PIII treatment.

(d,e) HRTEM images of ZnO comb fingers taken from the selected area in (a) and

(b), respectively.

5.3.3 Low-temperature PL analyses in UV region

Figure 5.3 shows the normalized near band-edge (NBE) PL spectra of the as-grown, 0

and 5 kV Ti-PIII treated ZnO NCBs obtained at 4.5 K for curves A-C, respectively. The

inset shows room temperature NBE PL spectra of the as-grown (curve A') and 5 kV Ti-

PIII treated NCBs (curve C'). The PL spectra of ZnO NCBs before surface modification
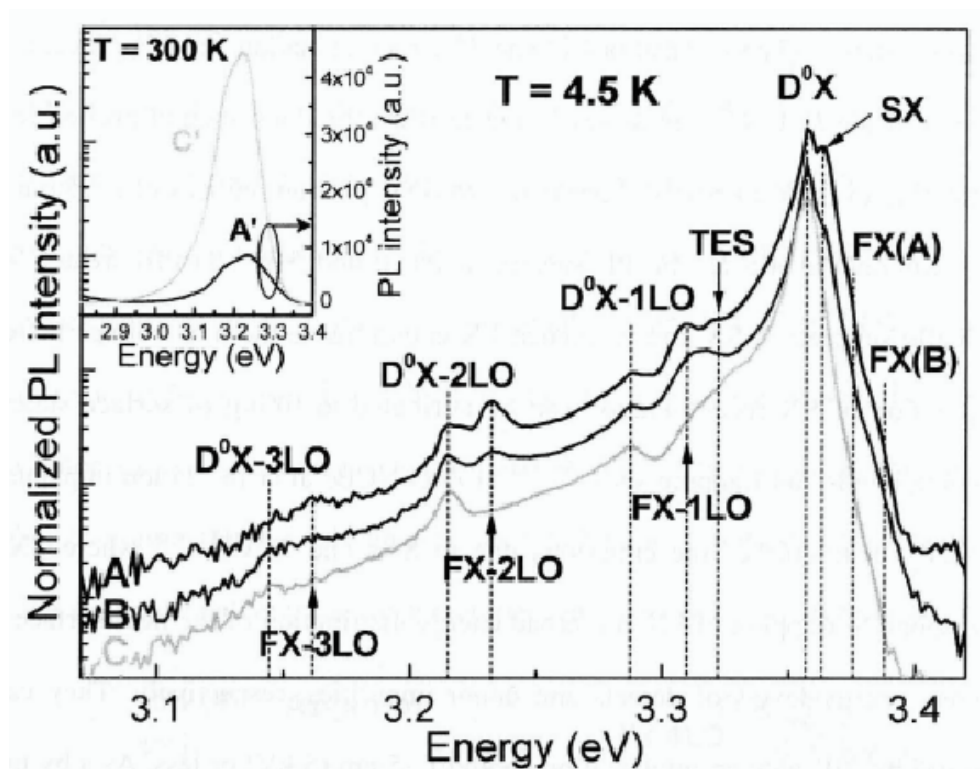
Figure 5.3 Normalized PL spectra of ZnO NCBs before and after 0 and 5 kV Ti-PIII treatments. The curves are shifted in intensity for a better comparison. The inset compares room-temperature PL spectra before and after 5 kV Ti-PIII.

are dominated by the emission peak at 3.3576 eV originating from the radiative recombination of donor-bound excitons (D^0X).[123] Another strong peak at 3.3641 eV is assigned to the recombination of SXs,[126, 138, 140] consistent with the large surface area of NCBs. Two small shoulders can be observed at 3.3773 and 3.3889 eV, which are assigned to the recombinations of the A- and B-free excitons (FXs), respectively.[123] On the lower energy side of these bands, the phonon replicas of D^0X and A-FX are observed, with average spacings of 71.7 and 71.8 meV, respectively, consistent with the LO-phonon energy of ZnO. According to Teke *et al.*,[123] the peak at 3.3217 eV might be due to two-

electron satellite (TES) transitions of the D^0X recombination. In this process, the donor electron of the D^0X is left in an excited state when the donor-bound exciton recombines. Comparing to the well-resolved peaks due to SXs, phonon replicas of D^0X and FX of the as-grown ZnO at 4.5 K, the PL spectra of the 0 and 5 kV Ti-PIII treated ZnO show gradually suppressed SX and weakened FX emissions as the bias voltage increases. The suppression of SX recombination can be attributed to filling of surface states, such as dangling bonds and trapping sites,[126, 138] of ZnO NCBs after the Ti ion implantation. This evidently distinguishes the emissions due to SXs and D^0X,[123, 138] where SX and D^0X correspond to trapping of FX at a broad energy distribution of the near-surface states and discrete energy levels of defects and donor impurities, respectively. They can be well resolved by PIII with an implantation depth of ~5 nm (5 kV) or less. As a by-product, we can conclude that the surface states responsible for SX's are located within a 5 nm depth from the surface. On the other hand, the D^0X-related and TES emissions are retained, suggesting that the donor-bound radiative recombination persists inside the bulk of the NCBs. These SX quenched samples showed a better PL performance at room temperature, where distinct PL enhancement (300 K) can be seen in the inset of Figure 5.3.

As temperature increases [Figure 5.4 (a)], the intensity of D^0X-related and SX emissions decrease much faster than that of A-FX and its first two replicas due to thermal activation of the donor-bound excitons, and finally the FX becomes dominant at room temperature.[140] The dissociation of the D^0X results in increased emission from the free excitons and other shallower donor-bound excitons.[123] This is consistent with the observation in Figure 5.4 (b), in which the D^0X replicas vanish and FX replicas re-appear

at 60-80 K. The SX emission is thermally quenched and merged with D^0X around 60 K, due to the dissociation of excitons trapped to SX states into FX states with increasing temperature, with a low thermal activation energy corresponding to the energy separation between the FX and SX peaks (~ 13 meV), which is slightly larger than the value reported by Wischmeier *et al.* (~ 9 meV),[139] and smaller than that of D^0X (10-20 meV).[123] In comparison to donor impurities which are the origin of D^0X emission, the broad-energy-distributed surface states responsible for the SX recombination, in accordance with large surface-to-volume ratio, could be less stable at high temperature. The ionization of these surface states at relatively low temperatures can create non-radiative surface traps which
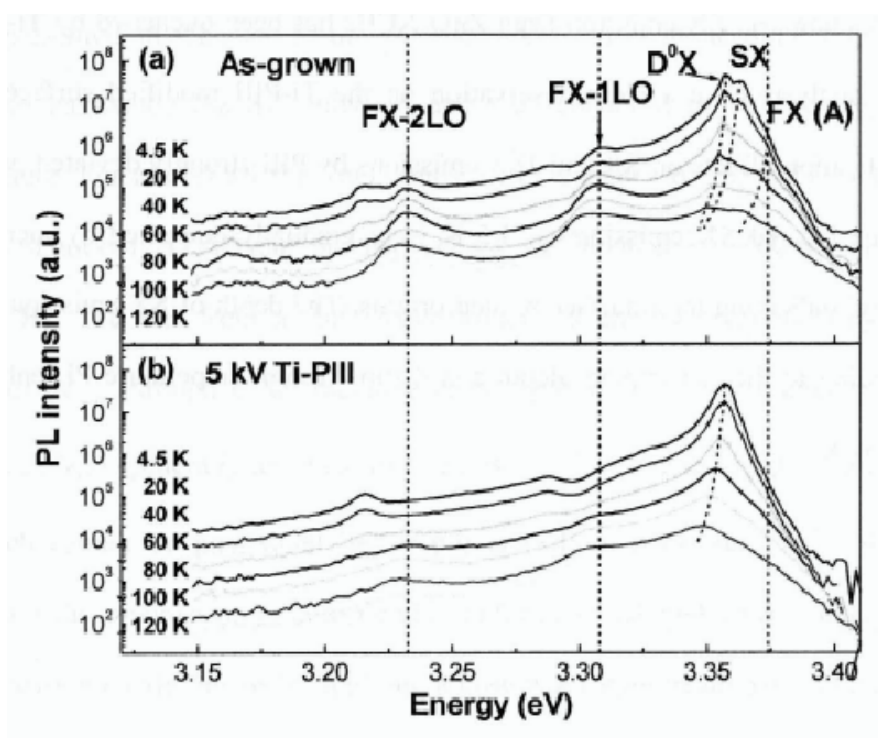
Figure 5.4 Temperature-dependent NBE recombination for (a) as-grown, and (b) 5 kV Ti-PIII treated ZnO NCBs showing the FX and its LO phonon replicas. The vertical lines indicate the maxima of the FX, FX-1LO and FX-2LO in (a) at 4.5 K. The curves are shifted in intensity for a better comparison.

induce rapid decay of FX's at room temperature, resulting in a weak PL.[126] Our surface modification thus blocked this nonradiative recombination process of FX by passivating these surface states. This is the reason why the surface passivation layer containing Ti impurities can enhance room-temperature NBE PL. It is worth mentioning that other elements, e.g. Fe, Ni, Cu, and C, have a similar modification effect through low energy PIII, indicating that the PL of ZnO is insensitive to the implanted elements used.

5.4 Summary

In summary, SX emission from ZnO NCBs has been quenched by Ti-PIII treatment. TEM analysis gave a clear observation on the Ti-PIII modified surface of ZnO. The modification effects on SX and D^0X emissions by PIII strongly deviated, where the near-surface located SX emissions at 4.5 K were gradually quenched by increasing the ion energy, indicating their surface related origins. The depth of SX emission was estimated according to the ion implant depth and distinct room-temperature PL enhancement was achieved.

Chapter 6 SURFACE MODIFICATION OF ZNO NANOSTRUCTURES II- QUENCHING OF GREEN EMISSION

6.1 Introduction

As-presented in Chapter 5, the surface modification induced after using the PIII technique passivated the SX emission and thus enhanced the UV emission at room temperature. For almost all the ZnO nanostructures grown by the VPT method, the PL consists of not only a UV band, but also a deep-level broad emission band called the green band (GB). The GB from a ZnO nanostructure is caused predominantly by oxygen vacancies (V_O), through either radiative recombination involving single ionized oxygen vacancies ($V_O^{\bullet}$) (generally accepted hypothesis)[128, 129] or deeply trapped holes in $V_O^{\bullet\bullet}$,[134, 135] which cannot be passivated by simply annealing in oxygen.[143, 144] An important question is the suppression of defect emission for practical applications, either by varying the fabrication conditions or by applying a post-fabrication treatment. In this Chapter we shall continue the study of surface modification by PIII, and its modification effect of GB emissions will be compared between three different ZnO nanostructure systems: NCBs, random nanowires (RNWs), and aligned nanowires (ANWs) when the bias voltages range from 0 to 10 kV. Gradual GB quenching and drastic UV emission enhancement has been

observed in ANWs, revealing a deeper GB origin in these structures as compared to the NCB and RNW systems.

6.2 Experimental details

6.2.1 Growth of ZnO nanostructures

The ZnO nanostructures were grown by VPT method from ZnO (99.99%, Alfa Aesar) and graphite powder (99.99%, Aldrich) (1:1 wt%) on the Si (111) substrate pre-coated with a 20 nm Au film. The source was placed in the center of a horizontal tube furnace maintained at 950°C, and the substrate was placed at a temperature zone of 650-450°C for collecting ZnO nanostructures. ZnO ANWs, RNWs, and NCBs were fabricated by varying the O_2 flow rate from 2-10 sccm while keeping a constant Ar flow rate at 100 sccm. The growth followed the VLS mechanism.

6.2.2 Surface modification by Ni-PIII

The as-grown ZnO nanostructures were directly treated with Ni-PIII. During the treatment, negative pulse voltages of 0, 2, 5, and 10 kV, respectively, were applied to the sample for 1-5 min. The ion dose was estimated to be $\sim 1 \times 10^{15}$ ions/cm^2 for a 5 min treatment with 10 kV bias (maximum ion dose conditions in this work). The substrate temperature has been monitored to be below 100°C.

6.3 Results and discussion

6.3.1 SEM and XRD analyses of NCBs, RNWs, and ANWs

Figure 6.1 (a-c) shows the representative SEM images of ZnO NCBs, RNWs, and ANWs deposited on Si at a constant Ar flow and O_2 flow rates of 10, 4, and 2 sccm, respectively. The NCBs are grown in higher O_2 flow in comparison with that of NWs. The as-grown ZnO NWs showed very uniform diameters and length covering a large area of the substrate (1×1.5 cm). The average diameters of RNWs and ANWs are ~50 and ~150 nm, respectively, while the average lengths were ~10 and ~4 μm, respectively. It is obvious that in our experiment, by increasing the O_2 flow from 2 to 4 sccm, the length of the NWs is increased and therefore faster growth takes place along the *c*-axis. However, they bundle together easily when they grow longer. As shown in Figure 6.1 (d), the XRD patterns corresponding to Figure 6.1 (a-c) have a strong and sharp peak from the (0002) plane with decreasing O_2, confirming the *c*-axis preferred orientation of NWs. Therefore, in an O_2-rich environment, ZnO prefers to grow into comb morphology, whereas when O_2 is deficient, ANWs are preferred, due to a self-catalytic growth process.[131] This is consistent with previous studies on the controlled growth of ZnO NWs and combs.[127, 155] In addition, there was no noticeable change before and after the PIII treatment in the morphology and (0002) diffraction peak position according to SEM and XRD analysis. In fact, from the SRIM,[148] the implant depth corresponding to the projected range of Ni ions into the ZnO crystal is around 0.4, 2.5, 4.3, and 6.7 nm for 0, 2, 5, and 10 kV bias voltages, respectively. In comparison with the diameter of NCB fingers and NWs (50~100 nm), the PIII in our experiments only modified the subsurface of ZnO.
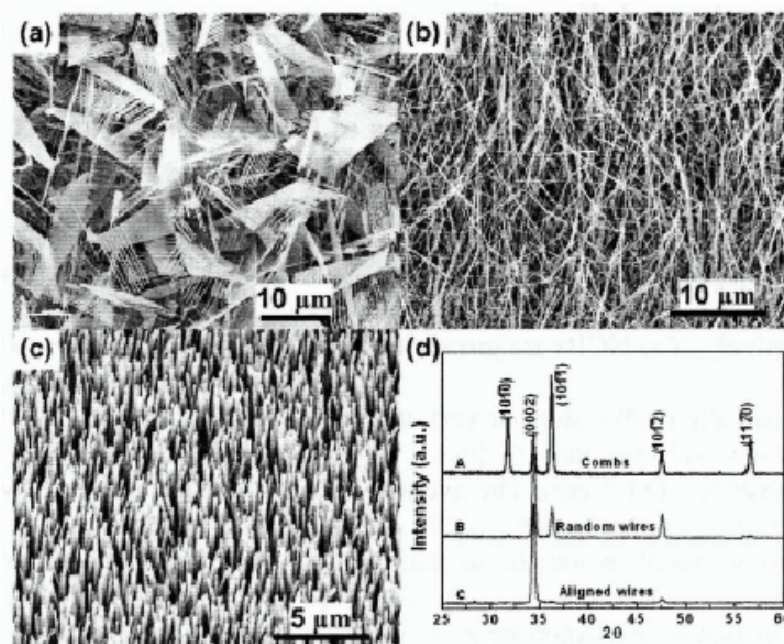
Figure 6.1 (a-c) SEM images of (a) NCBs, (b) RNWs, and (c) ANWs.

(d) Corresponding XRD spectra of these three morphologies with the intensity

normalized to the maximum separately for each curve.

6.3.2 TEM analyses on the surface structure after PIII

The surface modified ANWs were studied in TEM to examine the surface structure after PIII. Figure 6.2 (a) shows the low-magnification TEM images of a typical NW subjected to 5 min 10 kV Ni-PIII with the corresponding SAED pattern shown as inset. Irregular dark and bright regions of the TEM image indicate that Ni implantation is all over the NWs. Figure 6.2 (b) and (c) show the HRTEM images of the NW edge facing the coming Ni ions (enclosed area B) and the side surface of the NW parallel to the Ni ions implantation direction (enclosed area C), respectively. The lattice spacing of 0.26 and

0.28 nm corresponds to the *d*-spacing of (0001) and (01$\bar{1}$0) plane of wurtzite ZnO, respectively, confirming that the ZnO NWs are preferentially oriented in the *c*-axis
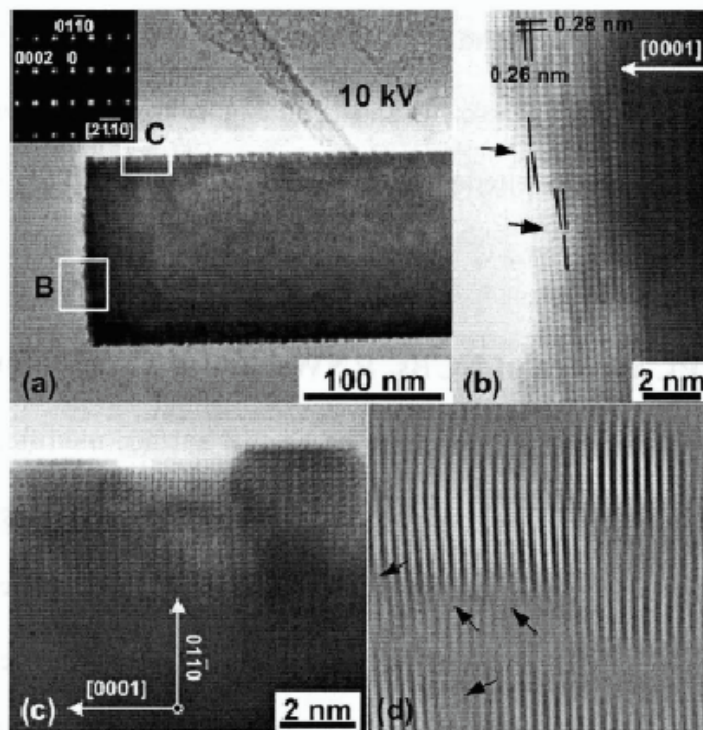
Figure 6.2 (a) Low-magnification TEM images of the typical NW modified by 5 min 10 kV Ni-PIII. Inset shows the corresponding SAED pattern. (b,c) HRTEM images of (b) the edge facing the coming Ni ions (enclosed area B) and (c) the surface paralleling the coming direction of Ni ions (enclosed area C), respectively. (d) Back and forth FFT from ±0001 diffraction spots of (c).

direction. No Ni/NiO$_x$ coating or new complex crystal phase could be seen in the HRTEM, indicating atomic level incorporation of Ni ions into the ZnO crystal. Metal aggregation and crystallization were avoided due to low thermal spike energy and low Ni ion dose. Although ZnO is a very irradiation resistant material, due to the high bonding ionicity and the confined energy dissipation in the nanostructure,[193] the lattice damage

78

becomes observable in HRTEM upon 10 kV PIII. As pointed out with black arrows in Figure 6.2 (b), several line defects could be found in the tip facing the coming Ni ions. The corresponding back and forth Fourier transformation (FFT) from ±0001 diffraction spots of Figure 6.2 (c) (inset) is shown in Figure 6.2 (d), where the line defects can be seen clearly within the (0001) planes.

6.3.3 PL spectra of NCBs, RNWs, and ANWs, before and after PIII

The representative PL spectrum of Ni-PIII surface modified ZnO NCBs and RNWs are shown in Figure 6.3 (a) and (b), respectively. The bias voltages applied for both NCBs and RNWs were optimized to achieve the best PL enhancement. All our samples exhibited strong NBE emission [see also Figure 6.4 (a)] when excited by a constant laser power ($\sim$400W/cm^2, 1%, λ=532 nm). For the untreated ZnO, relatively weak NBE emissions can be seen at $\sim$3.26 eV, with broad and strong GB emissions peaking around 2.3 eV. The GB emission is significant in all the as-grown ZnO nanostructured systems in our experiments. For NCB and RNW systems, since the large outer surface area of the ZnO nanostructures strongly attracts impurities on the surface, which traps free exciton (FX) to form SX at low temperature, NBE emission enhancement can be observed due to SX quenching on the surface.[194] In addition, both nanostructure systems showed complete quenching of the GB emission after a PIII treatment with the bias voltage between 0 to 10 kV. This GB passivation also contributes to significant enhancement of UV emission [see Figure 6.3 (a) and (b)], where free exciton recombination is enhanced at room temperature due to modification/passivation of both surface states (origin of SX) and surface defects (origin of GB).[195] The origin of GB has been studied extensively, which is generally

attributed to the transition of native defects such as singly ionized oxygen vacancies ($V_O^{\bullet}$

),[129] and there are evidences showing that it is located at surface.[196-198] The complete

quenching of surface-located GB emission (close to background noise) suggests that the

origin is located with no more than 0.5 nm in depth according to ion implantion depth.

However, complete passivation of GB emission after shallow surface modification (0 kV

PIII) does not apply to ANWs deposited with only 2 sccm flow of O_2 (O_2-deficient

situation).
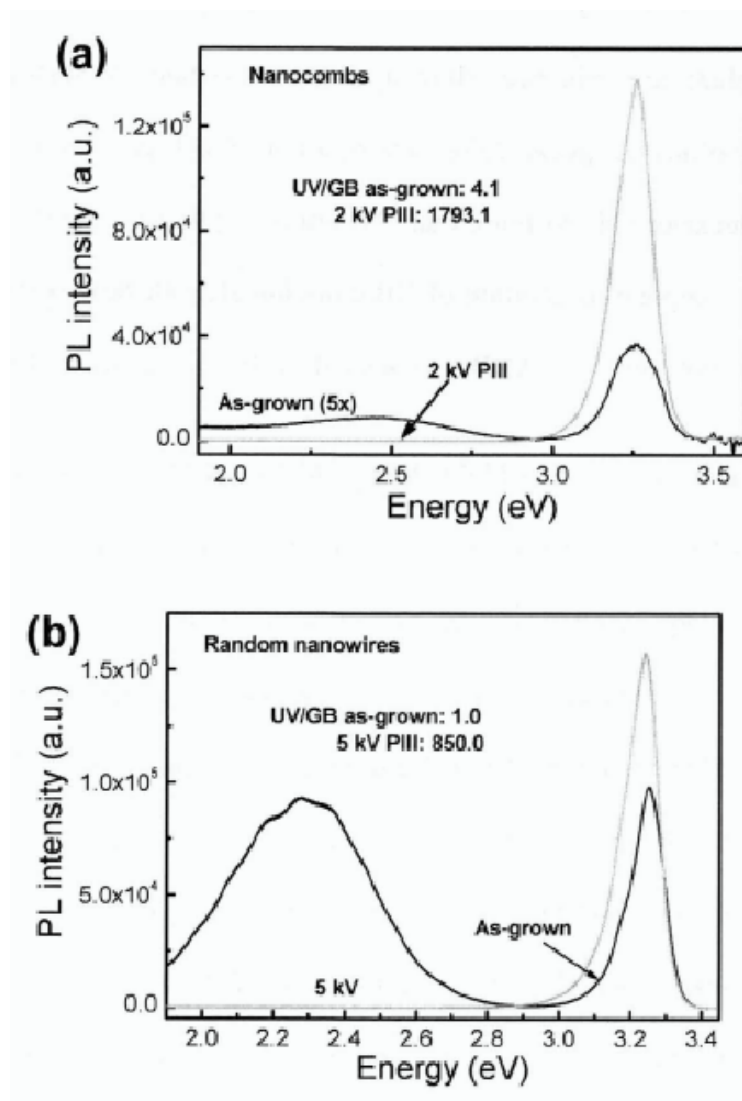
Figure 6.3 Room temperature PL spectra of the as-grown and (a) 2 kV PIII treated ZnO NCBs and (b) 5 kV PIII treated RNWs.

The PL spectra of Ni-PIII treated ZnO ANWs are shown in Figure 6.4 (a). It is worth mentioning that special care was taken for both sample preparation and measurements in order to ensure that the PL results are reliable and comparable. Firstly, the ANW samples for PIII treatment were grown in a single run inside the same constant temperature zone in the furnace. Secondly, the PL measurements for the as-grown, 0, 2, 5, and 10 kV PIII

treated ANW samples were carried out together with the same measurement setup and sample alignment. Green emission quenching is achieved by Ni-PIII with the bias voltage increased from 0 to 10 kV, where the intensity is close to background noise after 10 kV PIII treatment. The NBE emission enhancement, on the other hand, reaches its maximum fora PIII bias voltage of 5 kV, and is not linearly proportional to this bias voltage. The red shift (10-17 meV, 1-3 nm) of the NBE emission is significant at higher bias voltage and ion dose (up to 5 min 10 kV, ion dose $\sim 10^{15}/cm^2$), whereas the peak broadening is not observable. The red shift of the NBE emission can be attributed to an optical band-gap narrowing effect caused by a merging of donor and conduction bands, and band tailing by impurity-induced potential fluctuations, indicating a semiconductor-metal transition due to metal ion implantation.[124] The latter phenomenon happens when the carrier concentration exceeds the Mott critical density.[124] As shown in Figure 6.4 (b), the intensity of GB decreases gradually with applied bias voltage, and correlates quite well with the ion implantion depth. For this ANWs, the correlation between the GB suppression (y) (ratio of after PIII to as-grown GB intensity) and the ion implant depth (x) can be expressed as $y=y_0+a*e^{-x/b}$ experimentally, where y_0=0.003 (0.3 % of the as-grown GB intensity) is the bulk contribution to GB emission, and a and b (0.28 and 1.7, respectively) are the fitted parameters. Figure 6.4 (c) shows the UV/GB improvement after PIII treatment. It can be seen that the ratio increases linearly with the bias within experimental range (10 kV). It reaches around 100 times by 10 kV PIII. In addition, we also observed similar visible luminescence quenching and UV enhancement by applying Ti- and Fe-PIII. Similar to our previous analysis, we can conclude that the GB origin is ~7 nm in depth corresponding to the ion implant depth, which is much deeper than that of

NCBs and RNWs. The results correlate well with the growth condition of ANWs where lowest O_2 flow was used among the three morphologies. It is worth mentioning that the depth of GB origin is different from the thickness of surface-recombination layer,[104, 133] which includes a certain effective diffusion length. The GB distribution and depth depends on growth conditions, especially the O_2 concentration just like what we showed in this chapter.
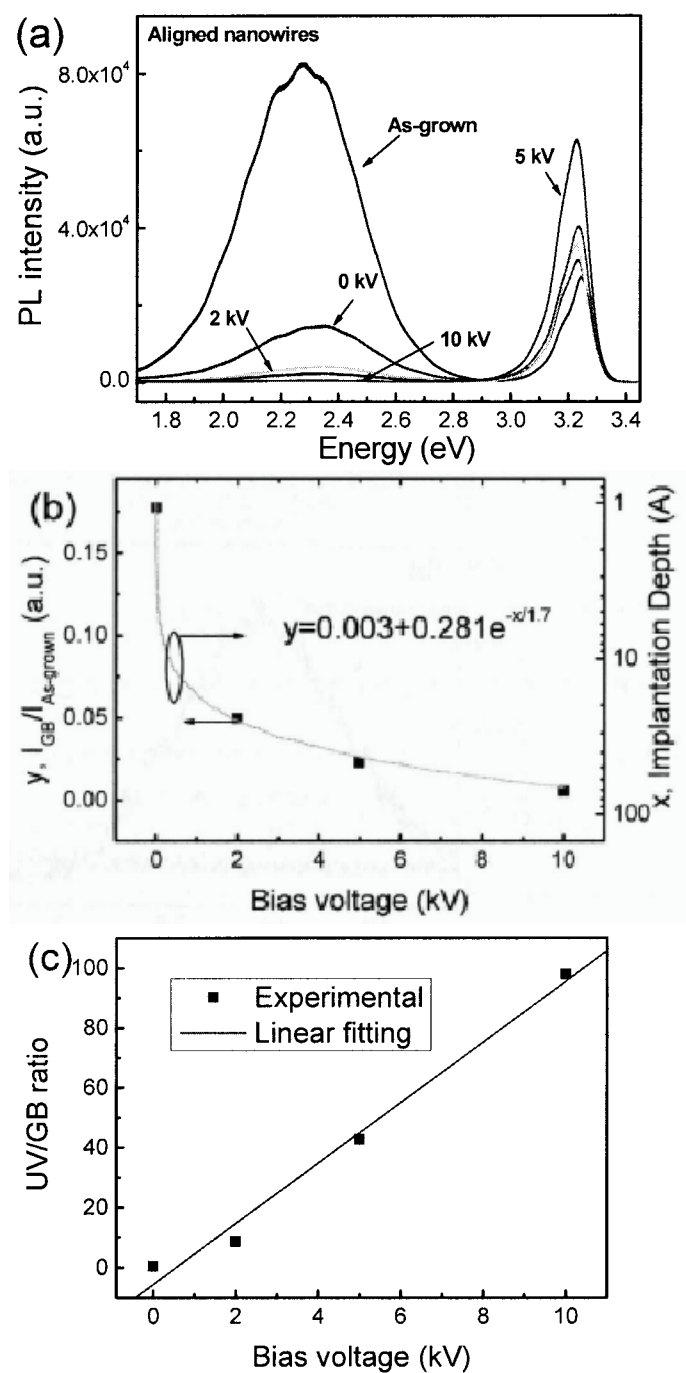
Figure 6.4 (a) Room temperature PL spectra of as-grown and 0, 2, 5 and 10 kV

Ni-PIII treated ZnO ANWs. (b) Plot of GB suppression (y, left Y axis, ratio of the

GB intensity after PIII to as-grown, $I_{GB}/I_{As-grown}$) vs. Ni ion implant depth (x, right

Y axis, semilog plot). (c) Plot of UV/GB ratios vs. PIII bias voltage.

6.3.4 Low-temperature PL studies on ANWs
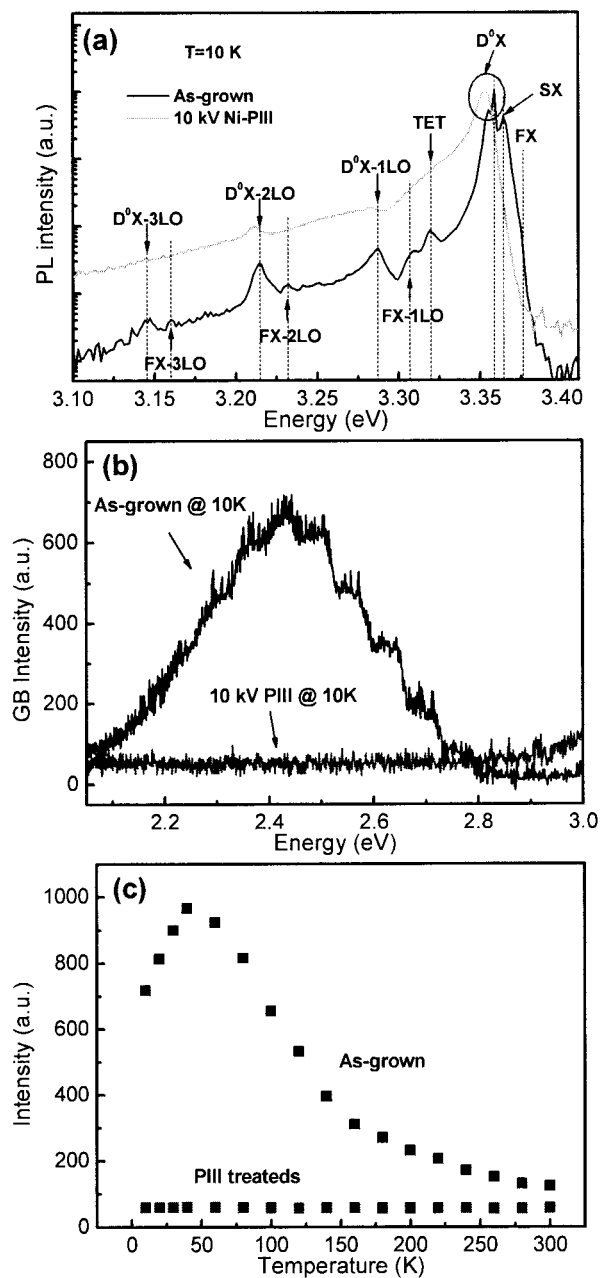
Figure 6.5 (a) Normalized NBE luminescence spectra of ZnO ANWs before and after 10 kV Ni-PIII treatments. (b) GB spectra of ZnO ANWs before and after 10 kV PIII. (c)Intensity of the corresponding GB emissions plotted as a function of temperature.

The optical properties of the ZnO ANWs modified by PIII were further studied by low temperature PL. Figure 6.5 (a) shows the normalized NBE spectra of the as-grown and 10 kV ion treated ZnO ANWs obtained at 10 K. The PL spectra of as-grown sample are similar to that of NCBs shown in Section 5.3.3. Red-shift of the peak positions after PIII becomes obvious at this ion dosage, which can be attributed to the relative contributions of FX, FX-1LO, and FX-2LO altered by surface modification.[140]

Figure 6.5 (b) shows the GB spectra of the as-grown and 10 kV PIII modified ZnO ANWs measured at 10 K, with the corresponding GB intensity plotted as a function of temperature. As shown in Figure 6.5 (b), the appearance of the LO phonon structure indicates that the strong electron-LO phonon coupling is responsible for the observed broad GB in ZnO. The average separation is 69 meV, consistent with the characteristic energy of LO mode. As temperature is increased from 10 to 300 K, the intensity increases up to 40 K then decreases gradually with increasing temperature for the as-grown sample. The decrease with temperature follows the normal temperature behavior of semiconductor luminescence, and is caused by several quenching mechanisms such as thermal activation of nonradiative centers and thermal escaping of localized carriers involved in the emission process.[199] At low temperatures (less than 40 K), the intensity of GB increases with temperature, which has not been observed before. We suggest that this can be attributed to the thermal activation of nonradiative transition path(s) from FX and/or D^0X to deep-level excitons at elevated temperatures. It can be seen that the GB intensity of as-grown ZnO increases with the decrease in temperature (50 K - 300 K), whereas the GB of treated ZnO ANWs was below the detection limit in the entire temperature range from 10 to 300 K, indicating a temperature independent surface modification/passivation process of the

subsurface defects that are responsible for GB. Based on the proposed hypotheses on the GB emission mechanism, the GB quenching could be attributed to passivation of the hole trapping sites such as $V_O^{\bullet}$,[128, 129] and/or electron trapping sites such as $V_O^{\bullet\bullet}$ [134, 135] at the surface by implanted Ni ions, and therefore blocking the radiative transition recombination between the photoexcited holes in the valence band (or shallowly trapped holes) and the electrons in $V_O^{\bullet}$ and/or the photoexcited electrons in the conduction band (or shallowly trapped electron) and the deeply trapped holes in $V_O^{\bullet\bullet}$. The Ni-PIII treated ZnO is observed to have an enhanced conductivity as shown in Figure 6.6, which implies that the incorporated Ni ions act as shallow donors.

The depth of native defects, such as oxygen vacancies, correlates to the band bending and depletion width of the subsurface of nanostructure, which are closely related to the various properties of ZnO, such as photosensitivity, gas sensitivity, field emission etc.[129, 133, 200] Therefore, the study of the depth of native defects also helps to understand the diverse responses of various kinds of ZnO nanostructure morphologies for photodetector, gas sensing, field emission applications, etc. Using gas sensing as an example, generally, there are two main approaches to enhance the sensitivity. The first one is to obtain nanostructures of small size and large surface area,[201] and the second one is to control the depletion width.[202] From our surface passivation study of ZnO nanostructures, the product grown in O_2-deficient environment could have a significantly deeper defect-containing (depletion) layer, which is expected to have a better sensitivity compared to those grown in O_2-suficient environment. Moreover, by applying PIII surface modification, which is a non-destructive and well-developed technique, we can quench the GB emissions of
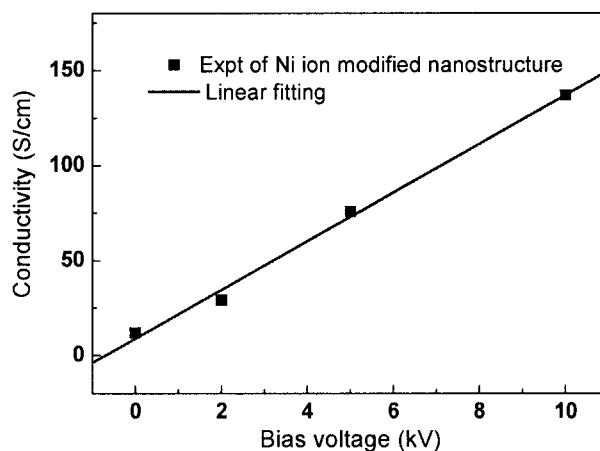
Figure 6.6 Plot of conductivity vs. bias voltage of Ni-PIII modification. The

conductivity was measured using a simple two-probe configuration.

various origin depths. PIII should thus have a significant role for surface modification of

nanostructures in practical applications.

6.4 Summary

In summary, by applying Ni-PIII surface modification/passivation on ZnO NCBs,

RNWs, and ANWs, we have probed the depths of the corresponding defects responsible

for GB emission for the nanostructures grown at different oxygen ambient. Quenching of

GB luminescence and enhancement of UV/GB ratio has been achieved. The GB of ANWs

was gradually quenched by increasing bias voltages from 0 to 10 kV, and showed deeper

depth (~ 7 nm) of subsurface located GB origin than that of NCBs and RNWs (~ 0.5 nm).

The quenched GB is temperature independent, and it can be attributed to passivation of

surface hole/electron trapping sites by Ni ions. The PIII technique has been demonstrated

to be suitable for non-destructive surface modifications on nanostructures to achieve enhanced optical properties. It is a useful tool to directly probe the surface native defect depth in terms of the ion implantation depth, which is also closely related to the surface-sensitive properties and applications of metal oxides.

Chapter 7 TWINNED Zn_2TiO_4 SPINEL NANOWIRES USING ZnO NANOWIRES AS A TEMPLATE

7.1 Introduction

As-presented in Chapter 3 to 6, several ZnO nanostructures have been prepared, and the PIII surface modification technique has been successfully applied to ZnO nanostructures to improve the PL properties. Followed by the controlled synthesis of ZnO NWs, we will investigate the application of ZnO as a template to grow other oxide nanostructures.

Due to the limited properties and applications of the nanomaterials by their simple binary systems,[203] synthesis of complex functional nanomaterials with controlled size and morphology, such as core-shelled quantum dots,[204] NWs and nanobelts,[205-208] heterostructures,[203, 209] superlattices,[210] and nanotubes,[206, 211-213] are highly desirable. Furthermore, the 1D ternary nanocomposites, such as Zn_2SnO_4,[205, 208, 214] Zn_2TiO_4,[215] $ZnGa_2O_4$,[207, 213] $MgAl_2O_4$,[211] $CoFe_2O_4$[216] etc, exhibit specific functions that are unattainable by common binary composites. Conventional synthesis methods of those ternary composites usually involve high-energy ball milling of two binary solid oxides,[215] or high temperature solid reaction,[217, 218] which are not suitable for 1D nanostructure

growth. Only recently, syntheses of single crystal ternary oxide NWs and nanotubes have been achieved by using Ga_2O_3, MgO or ZnO NWs as template.[207, 211, 212] For face-centered cubic (*fcc*) nanostructures, twinning is probably the most common structural defect, especially in metal and metal alloy nanoparticles,[219, 220] where two subcrystallites share a {111} facet to form a mirror image of each other. Twinning is occasionally observed in binary systems, such as cubic ZnS and InP NW,[60, 221] both of which have a preferential <111> growth direction. However, report on the synthesis and twinning structure of *fcc* ternary NW is rare;[206] the formation of twinned NW is unrevealed.

In this chapter, we shall present a three-stage synthesis of twinned Zn_2TiO_4 NWs using ZnO NWs as template. Zinc titanate (Zn_2TiO_4) is an inverse spinel, which has been used as a catalyst and pigment in industry. It is one of the leading regenerable catalysts, and has been demonstrated to be a good sorbent for removing sulfur-related compounds at high temperature.[222, 223] As a dielectric material, its physical, electrical and optical properties have been studied for various applications.[218, 224, 225]

7.2 Experimental details

7.2.1 Growth of ZnO nanowire

The ZnO nanowires were synthesized by VPT from ZnO (99.99%, AlfaAesar) and graphite powder (99.99%, Aldrich) (1:1 wt%) on a (111) Si substrate (with a 5 nm Au layer served as catalyst). In brief, a small quartz tube containing the source and Si substrate was inserted into a horizontal quartz tube furnace at 950°C. The furnace was kept at about 1 Torr with a rotary pump, with a constant flow of 150 sccm Ar and 5 sccm

O_2 for 30 min, after which the small quartz tube was pulled out and cooled down to room temperature.

7.2.2 Magnetron sputtering deposition of Ti

The as-synthesized ZnO NWs were then transferred into a vacuum deposition system for Ti deposition by DC magnetron sputtering [226]. The deposition took place at room temperature with a base pressure below 1×10^{-4} Torr, and a constant Ar flow of 40 sccm. The DC voltage used in the DC magnetron sputtering was 450 V, and the sputtering time was 10 min. The film thickness was controlled to be less than the typical thickness of ZnO NW to meet the stoichiometric requirement of spinel phase. After deposition, the color of the substrate changed from light blue to black.

7.2.3 Solid-state reaction and phase transformation

In order to transform the ZnO/Ti core/shell structure into zinc titanate, the sample was then loaded in a program controlled tube furnace. After evacuating the quartz tube to below 0.1 Torr, an optimized three-stage annealing process was performed under precise control of the reaction temperature in vacuum. The furnace was first slowly heated to 800 °C at a rate of 10 °C/min, then maintained for 8 hours, followed by slowly cooling down overnight.

7.3 Results and discussions

7.3.1 SEM and XRD studies on the morphologies and crystal structures

Figure 7.1 (a), (b) and (c) show the SEM images of ZnO NWs, ZnO/Ti core/shell NWs before and after annealing, respectively. The as-grown ZnO NWs shown in Figure 7.1 (a) are randomly aligned, about 40-60 nm thick and 10 μm long. It can be seen clearly that the morphology of the NWs has no change after coating with Ti [Figure 7.1 (b)], except slightly increasing in the diameter. The surface is smooth and the thickness is increased to 70-100 nm. No aggregated Ti particles could be seen in Figure 7.1 (b), indicating a uniform deposition of Ti on the ZnO NWs. After thermal annealing in low vacuum (0.1 Torr) at 800°C for 8 hours, the NWs are bent and curved, with small perturbations observed on the surface [Figure 7.1 (c)]. The XRD patterns in Figure 7.1 (d) illustrate phase changes due to Ti coating and thermal annealing. Curve A shows the as-grown ZnO NWs growing randomly in all directions. All peaks can be indexed to a wurtzite ZnO crystal with lattice constants of a=3.253 Å and c=5.209 Å].[227] Curve B shows that there is no phase transformation after Ti coating but before thermal annealing; no new peak or peak shift is observed. No corresponding Ti peaks could be identified in the spectrum (Curve B). Therefore, either the Ti phase is amorphous or the lattice diffraction signal of crystalline Ti is too low to be detected. Curve C shows the phase transformation of Ti-coated ZnO NWs after thermal annealing. Four peaks at 29.9°, 35.2°, 53.0° and 62.0° indicated by asterisk can be clearly seen, which correspond respectively to the (200), (311) (strongest), (422), and (440) crystalline orientations of the spinel Zn_2TiO_4 *fcc* crystal structure (space group *Fd-3m* with a lattice constant of a=8.460 Å).[228] It is worth mentioning that the atomic ratio of Ti:Zn is 1:2 to form stoichiometric
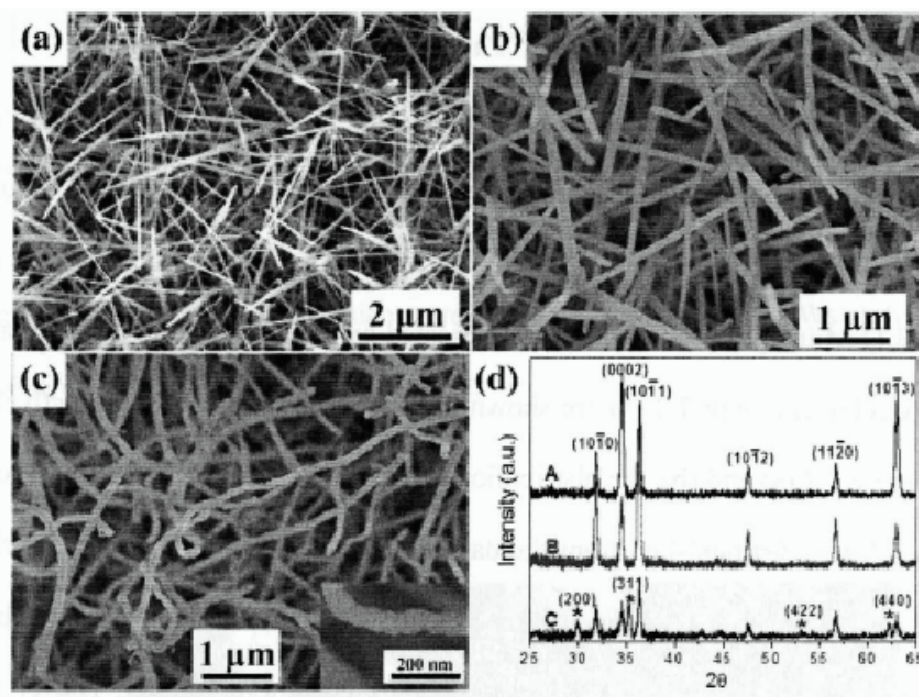
Figure 7.1 SEM images of (a)As grown ZnO NWs, (b) Ti-coated ZnO/Ti

core/shell NW, and (c) Zn_2TiO_4 spinel NWs and high-magnification SEM image

of a Zn_2TiO_4 NW (inset). (d) Corresponding XRD patterns of (a-c), denoted as

curves A, B, C, respectively.

Zn_2TiO_4. We have optimized the sputtering condition to yield maximum quantity of NWs

with the desired Ti:Zn ratio of 1:2. It can be seen from Figure 7.1 (d) that no diffraction

peak from either $ZnTiO_3$ or TiO_2 secondary phase could be found. The residual ZnO

diffractions in curve C, which have been weakened in intensity compared to curves A and

B, originate from the ZnO NWs at the bottom of the sample where no Ti was deposited.

7.3.2 TEM studies on the ZnO/Ti core/shell structure

The obtained NWs were scratched off after Ti coating and thermal annealing to investigate the crystal structures and phase transformation by TEM. Figures 7.2 (a) and (b) show respectively the BF and DF TEM images of a representative Ti-coated ZnO NW. HRTEM images of the ZnO core (indicated by a rectangle) and the Ti phase (indicated by a circle) in Figure 7.2 (a) are shown in Figure 7.2 (c) and (d), respectively. As shown in Figure 7.2 (a) and (b), the distribution of the ZnO and Ti phase (a core/shell structure) can be clearly distinguished from the dark field image. The thickness of Ti shell varies from about 40 nm to a few nanometers from left to right side of the NW. This is reasonable because only half of the NWs were facing the sputtering target. The Ti amorphous layer deposited in this way was not dense, as can be seen from the inhomogeneous contrast. This result agrees with Yu's work,[229] where a purely amorphous Ti film was sputter-deposited on a cooled substrate. It can be seen that the ZnO NW was partially bombarded off by electrons and ions in the plasma, which is a common phenomena in sputtering, resulting in ZnO content fluctuation along the NW. The inset in Figure 7.2 (a) shows the SAED pattern of the Ti-coated ZnO structure. It contains the diffraction pattern of wurtzite ZnO taken along the $[2\bar{1}\,\bar{1}0]$ zone axis and heavily amorphous phase of Ti mixed with small fractions of hexagonal close-packed crystallites, where the three major diffraction rings match Ti $\{10\bar{1}0\}$, $\{10\bar{1}1\}$, and $\{11\bar{2}0\}$. Structurally, ZnO has three typical fast growth directions: $[0001]$, $<2\bar{1}\,\bar{1}0>$ and $<01\bar{1}0>$, where the NWs and nanobelts growing along $[0001]$ and $<01\bar{1}0>$ or $<2\bar{1}\,\bar{1}0>$ directions have hexagonal and rectangular cross-sections, respectively.[38] In this work, the ZnO NWs elongate along the $[01\bar{1}0]$ direction, as revealed by the SAED pattern, which is similar to what we

observed in the nanobelts. The smooth core/shell interfaces shown in Figure 7.2 (c) exhibit distinguishable solid-solid contrast, as pointed out by the arrows in Figure 7.2 (a). HRTEM of the Ti layer deposited at room temperature is shown in Figure 7.2 (d), where the Ti crystallite phase can hardly be seen. It is worth mentioning that a small amount of NWs appeared without Ti coating, which were probably from the ZnO NWs at the bottom of the sample, consistent with the XRD results.
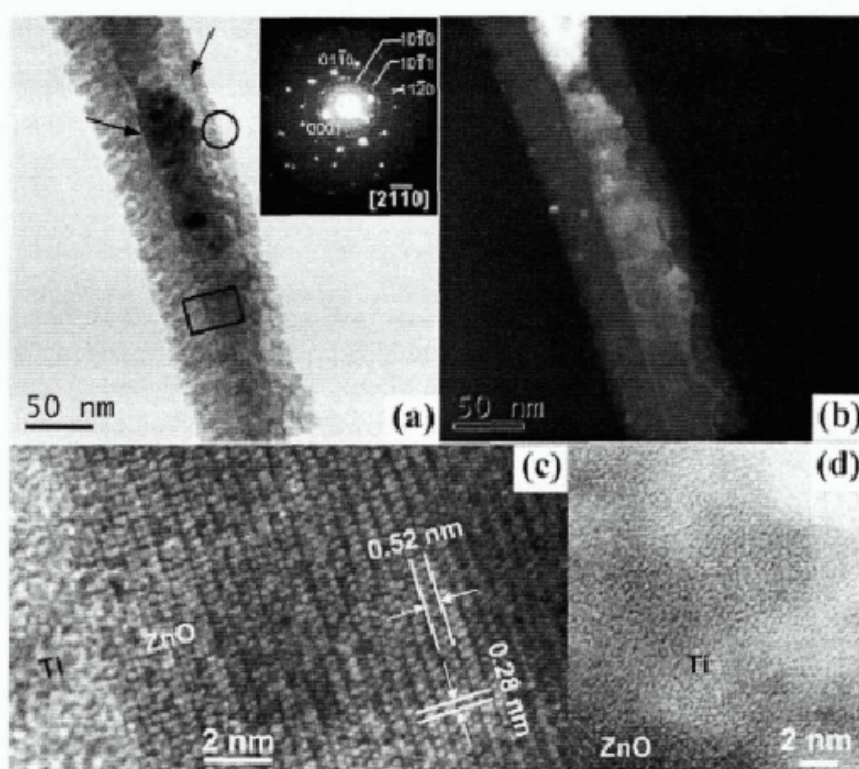
Figure 7.2 (a,b) BF (a) and DF (b) TEM images of a typical amorphous Ti-coated ZnO core/shell NW. Inset shows the SAED pattern of the NW. (c,d) HRTEM images of the single crystal ZnO core (c) and amorphous Ti shell of the region (d) indicated by the rectangle and circle in (a), respectively.

7.3.3 TEM studies on the twinned spinel structure

Thermal annealing at 800°C in low vacuum, triggered solid-state reaction involving diffusion of Ti into the ZnO crystal and their chemical reaction, resulting in the phase transformation from wurtzite ZnO to spinel Zn_2TiO_4. The final product contained a large amount of twinned NWs. Figure 7.3 (a) shows a typical twinned Zn_2TiO_4 spinel projected along the [011] zone axis. It can be seen that the twinned NW is composed of large parallelogram-shaped subcrystallites of tens of nanometers in width. The smallest ones are less than 10 nm wide, which can be defined as the grain transition region between two large grains. The corresponding SAED pattern shown in the inset of Figure 7.3 (a) reveals the (111) twin structure, with the NW growing along [$\bar{1}$ $\bar{1}$ 1] direction, which is consistent with twinned spinel Zn_2SnO_4 reported by Chen *et al.*[206] The twin plane is parallel to ($\bar{1}$ $\bar{1}$ 1) or (11 $\bar{1}$)T, where the subscript "T" denotes twin reflection to distinguish from single crystal. Our twinned NWs present a zigzag feature,[206] which can be attributed to the <111> oriented growth directions of each individual grains. The HRTEM images of the grain and twinned boundary (TB) taken from Figure 7.3 (a) are shown in Figures 7.3 (b) and (c), respectively. Both figures reveal good crystal quality of the NW. The interplanar spacings of 0.49 and 0.42 nm perfectly match the d_{111} and d_{200} spacings of the Zn_2TiO_4 crystal, respectively. The FFT pattern of Figure 7.3 (b) (inset A) is in good agreement with the Zn_2TiO_4 spinel crystal structure taken along [011] zone axis. The simulated HRTEM image [inset B in Figure 7.3 (b)] was obtained from Inorganic Crystal Structure Database (ICSD) #80850 for a sample thickness of 26 nm and a defocus value of 80 nm. The inset C in Figure 7.3 (b) is a schematic diagram (simulation
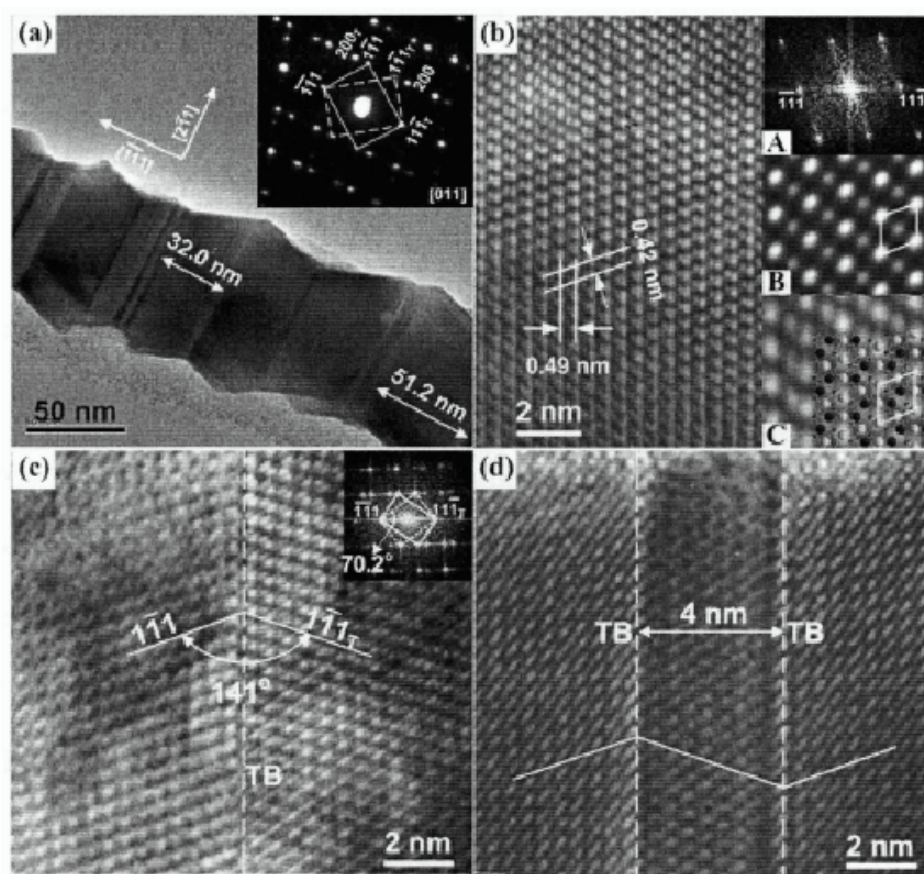
Figure 7.3 (a) Low-magnification TEM image of a typical twinned Zn_2TiO_4 NW.

(b) HRTEM images of a subcrystallite. Inset A shows the corresponding FFT

pattern. Inset B shows a HRTEM simulation image in agreement with the

experimental one. Inset C shows a schematic diagram of the lattice structure

corresponding to enlarged experimental HRTEM image, where blue, purple, and

red dots denote Zn, Zn/Ti (equal site occupation factor), and O, respectively.

(c) HRTEM image of TB between two large subcrystallites and corresponding

FFT patterns as inset. (d) HRTEM image showing the smallest distance between

two TBs that could be found from the NW.

from ICSD #80850) of a possible Zn_2TiO_4 lattice structure projected along [110] axis,

superimposed with the enlarged experimental HRTEM image. Four atoms are in the base

with Zn (1/8, 1/8, 1/8), Zn/Ti (1/2, 1/2, 1/2) (equal site occupation factor), and O (0.260, 0.260, 0.260), which are denoted as blue, purple, and red dots, respectively. Both the simulations of HRTEM image and crystal lattice structure agree well with the experimental HRTEM image, as indicated by the diamond shapes in insets B and C in Figure 7.3 (b). The TB marked by dashed line in Figure 7.3 (c) can be clearly resolved, showing free of misfit or distortion across the boundary. The FFT pattern of the TB [inset in Figure 7.3 (c)] agrees well with the SAED pattern of the twinned NW. The twinning angle cross the boundary is measured to be about 141°, and relative rotational angle from FFT pattern [inset in Figure 7.3 (c)] is about 70.2°, consistent with theoretical values of 141° and 70.5°, respectively. Figure 7.3 (d) shows the smallest grain width observed, which is around 4 nm wide (the two TBs are marked by dashed lines). Lattice distortion cross the boundary could be seen.

Figure 7.4 (a) shows the TEM image of another twinned spinel NW with zone axis tilted by 90° relative to the previous one observed along [011] [Figure 7.4 (a)], where the projected grain images are rectangular-shaped. As a general feature of twinned spinel structure, the NW is elongated along $[\bar{1}\ \bar{1}\ 1]$ direction, whereas both (022) and $(0\ \bar{2}\ \bar{2})$ facets of the NW are 90° away from the TB, with no zigzag morphology or relative grain shift could be observed. The parallel TBs can be clearly seen, and the subcrystallite size distribution is similar to that presented in Figure 7.3 (a). Figure 7.4 (b) is the HRTEM image of the TB taken from the rectangular area in Figure 7.4 (a), and inset A shows the corresponding FFT pattern. The lattice spacing for the $(\bar{1}\ \bar{1}\ 1)$ and (022) planes are 0.49 and 0.30 nm, respectively, in agreement with our previous TEM analysis shown in Figure 7.4 (b) (The lattice spacing of 0.49 nm corresponds to the d_{111} spacing). Inset B shows the
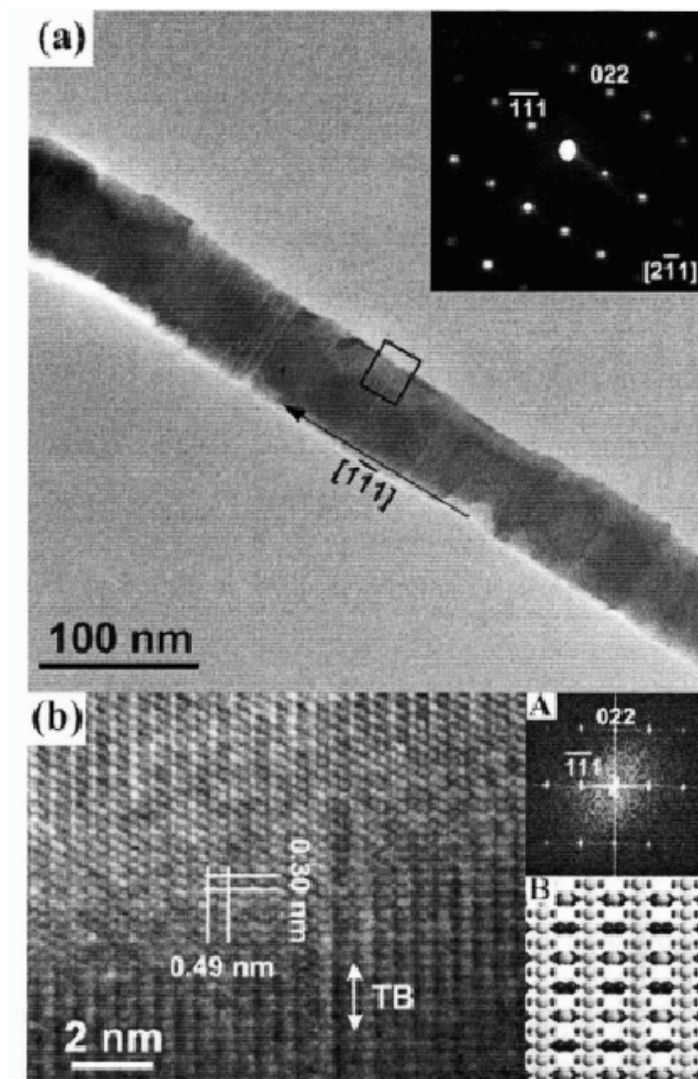
Figure 7.4 (a) Low-magnification TEM image of a Zn_2TiO_4 twining NW

projected along [112] zone axis. Inset shows the corresponding SAED pattern.

(b) HRTEM image of TBs taken from the rectangular selected area in (a). Inset A

shows the corresponding SAED pattern. Inset B shows a schematic diagram of the

lattice structure, where blue, purple, and red dots denote Zn, Zn/Ti (equal site

occupation factor), and O, respectively.

schematic diagram of the enlarged lattice structure of Zn_2TiO_4 projected along the $[2\,\overline{1}\,1]$ direction, and the notation is the same as that of Figure 7.3 (b). It can be seen that the twinned structure feature is absent along the $[2\,\overline{1}\,1]$ zone axis, therefore the TB in HRTEM can only be distinguished from the phase contrast.

7.3.4 Formation mechanism of the twinned Zn_2TiO_4 nanowires

From the chemical point of view, the formation of twinned spinel Zn_2TiO_4 NW is a solid-state reaction process, in which the ZnO NWs act as a template and spatially confine the reaction within them. Figure 7.5 illustrates the formation mechanism of the twinned Zn_2TiO_4 NWs. Firstly, a Ti amorphous layer is deposited on the ZnO NWs [Figure 7.5 (a)]. Upon thermal annealing of the ZnO/Ti core/shell structure at high temperature, Ti may absorb oxygen from both the ambient atmosphere and the solid ZnO to form TiO_x through chemical reaction, as illustrated in Figure 7.5 (b). The amorphous Ti and TiO_x are chemically active at high temperatures,[230] which is supported by the fact that the enthalpies of both TiO_2 (ΔH_{TiO2}= -944 kJ/mol) and TiO (ΔH_{TiO}= -519 kJ/mol) are much smaller than that of ZnO (ΔH_{ZnO}= -350 kJ/mol).[230] In comparison with Fan's work,[211, 212] our TEM analysis showed no voids or tube morphology, therefore the diffusion speed of Ti element is faster than or comparable with those of Zn^{2+} and O^{2-}. As Ti diffuses into ZnO, both Zn^{2+} and O^{2-} cannot remain fixed in their original lattice sites. Eventually, Zn_2TiO_4 spinel crystallites are formed with a preferred orientation along the <111> direction. For a *fcc* structure, the surface energy of different facets follows {111}<{100}< {110},[219] therefore, {111} is the dominant facet that encloses the crystal, which is

(a)   Ti atoms

↓ ↓ ↓ ↓ ↓ ↓ ↓ ↓ ↓ ↓ ↓ ↓

ZnO nanowire

↑ ↑ ↑ ↑ ↑ ↑ ↑ ↑ ↑ ↑ ↑ ↑

Ti atoms

Annealing

(b)   Zn₂TiO₄ subcrystallites

(c)

(d)

Twinned Zn₂TiO₄ nanowire
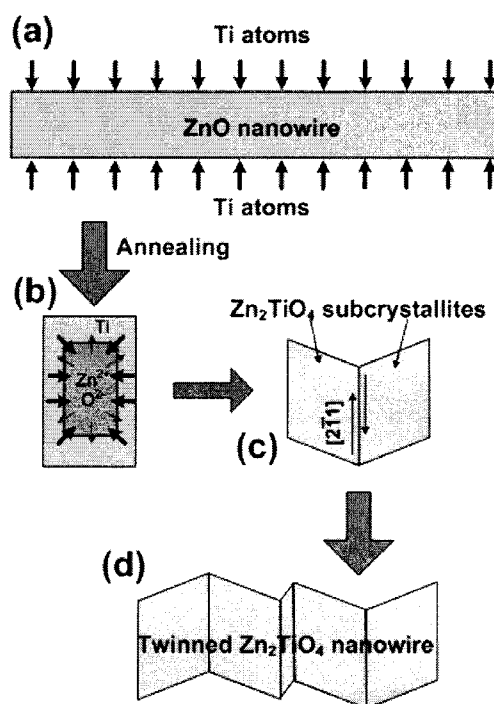
Figure 7.5 Schematic illustration of the formation process of twinned Zn_2TiO_4

NWs. (a) Ti is coated on the surface of the NW. (b) Cross-section of the core/shell

NW showing Ti on the surface diffuses into ZnO. (c) Formation of TB by two

adjacent Zn_2TiO_4 grains with different orientations moving relatively into a

symmetrical arrangement. (d) Formation of the twinned Zn_2TiO_4 NWs is

completed with new Zn_2TiO_4 grains growing from limited space between two

large grains.

consistent with our TEM observations of the twinned Zn_2TiO_4 NW. The twinned crystals

can be easily formed when two adjacent {111} faces meet by a relative shear movement of

the subcrystallites in $<2\bar{1}1>$ direction to produce a symmetrical arrangement, as

illustrated in Figure 7.5 (c). The shear movement is driven by dislocation induced

stress/strain to minimize the overall system energy.[231] This proposed hypothesis is

reasonable because small and individual subcrystallites can be formed easily in the NW due to the content fluctuation of ZnO, as can be seen in Figure 7.2 (a), in contrast to that of Ga_2O_3/ZnO core/shell structure reported by Chang *et al.*[207] Alternatively, the twinned structure can also be formed when new subcrystallites start to grow in a limited space between two existing grains, which most likely happen during the final stage, as illustrated in Figure 7.5 (d).

7.4 Summary

In summary, we have demonstrated a three-step method to synthesize ternary twinned Zn_2TiO_4 NWs. The ZnO NWs used as template were first coated with amorphous Ti to form a ZnO/Ti core/shell structure, followed by annealing at 800° for 8 hours. The ZnO core content appears to be fluctuating along the NW after Ti coating. The final product was (111) twinned Zn_2TiO_4 NWs growing along the $<11\bar{1}>$ direction. The formation of the twinned structure involves a solid-state reaction between Ti and the initial ZnO single crystal, that reduces the overall system energy. It is possible to apply this technique to synthesize NWs of other ternary materials.

Chapter 8 ZnO Nanorod

Homostructure Light-Emitting

Diodes

8.1 Introduction

As shown in Chapter 6, controlled growth of aligned ZnO NWs has been achieved, and the PL of these nanostructures has been enhanced by a simple surface modification technique. In the subsequent stage, the application of ZnO in light-emitting devices based on the success in ZnO NW array fabrication was investigated.

ZnO has attracted much attention for its potential applications in blue- and UV-emitting optoelectronics and high temperature/power transparent electronics. The large binding energy (60 meV) gives it the potential for higher brightness excitonic emission than GaN. In addition, ZnO has a high bonding strength, which makes it a resistant material to high energy radiation. It is also less expensive to grow compared with III-Nitrides, due to its lower required growth temperature, abundant mineral sources of Zn, and commercial availability of high quality single crystal substrates. However, the greatest challenge for applications remains the fabrication of low-resistivity, reliable and stable *p*-type ZnO thin films, and even nanostructures. Like many other II-VI semiconductors, ZnO has asymmetric doping limits. ZnO can be easily doped *n*-type, with the intrinsic ZnO being *n*-type, whereas *p*-type doping still remains a challenge.

Recent success in p-type doping in ZnO has opened a door for its practical applications to optoelectronic devices, such as light-emitting diodes (LEDs), UV lasers, and UV light detectors, which can be an alternative to those based on GaN. Larger-size group V elements, such as P, As, Sb, and Bi have been widely studied as possible p-type dopants for ZnO.[91, 114, 116-118, 120] It was predicted by Limpijumnong et al[114] that under oxygen-rich growth/annealing conditions, a complex mechanism involving a group V atom (e.g. As) and two Zn vacancies (As_{Zn}-$2V_{Zn}$) would have a low formation energy, and behaves as a shallow acceptor with an ionization energy of 150-160 meV. The As_{Zn}-$2V_{Zn}$ complex is formed when an As atom occupies a Zn "antisite" and is decorated with two Zn vacancies. A similar conclusion was made by Lee et al[116] for P. Although both stable n- and p-type ZnO films have been claimed to be grown,[91, 117, 118, 232] there are only a few reports on ZnO homojunction LEDs,[111, 112, 233, 234] and only a few more on heterojunction LEDs.[152, 232, 235-241] The UV and/or blue light emission intensity under forward bias is so far not comparable with those of GaN-based devices, while it was demonstrated by Jeong et al[238] that ZnO NW-inserted heterojunciton LEDs can exhibit improved EL emission and carrier injection efficiency.

In this chapter, we present the fabrication and characterization of stable p-n homojunction ZnO NR array LEDs. The p-n NR diodes were prepared by VPT method followed by As^+ ion implantation. Strong red electroluminescence from these p-n diodes has been observed.

8.2 Experimental details

8.2.1 Growth of aligned nanorods

The ZnO vertical aligned NRs with diameters ranging from 50 to 200 nm and length of up to 5 μm were grown on 1×1.5 cm^2 Si substrates via a simple VPT method in a horizontal tube furnace. The detailed synthesis was described in Section 6.2.1.

8.2.2 As$^+$ ion implantation

The as-grown ZnO NR arrays were annealed and subsequently implanted using VARIAN (E-220) ion implanter with 50 and 180 keV As$^+$ ions at a dose of 10^{15} cm^{-2} perpendicularly to the aligned NRs. The simulated projecting ranges of the implanted ions were 20 and 61.9 nm, and the longitudinal straggling were 8.9 and 24.4 nm for ion energies of 50 and 180 keV, respectively. Annealing of the as-grown and As-implanted ZnO NRs were performed for 2 hours at 750°C under vacuum ($\sim 5 \times 10^{-2}$ Torr), with O$_2$ flow of 50 sccm for both.

8.2.3 Device fabrication

Figure 8.1 is the schematic diagram of the *p*-ZnO:As NRs/*n*-ZnO NRs homojunction LEDs on *n*-ZnO film/*n*-Si substrate. After the As$^+$ ion implantation and thermal annealing, the top layer of the vertically aligned intrinsic ZnO NRs is doped with As$^+$ ions, which is indicated in purple in Figure 8.1. For the bottom contact, the backside of the Si substrate was etched by 2% HF solution to remove the oxide layer, followed by sputtering of a thick Au cathode. Preparation of the Au contact to the ZnO NRs relies on the use of

hydrophobic poly(methyl methacrylate) (PMMA) as an electrically insulating layer. PMMA is commonly used in the field of sensors, coatings, biomaterials etc., due to its good optical transparency, easy fabrication process, temperature resistance etc.[235, 242] The deposition of the insulator was carried out by several cycles of spin-coating a 5mg/ml solution of PMMA diluted in toluene onto the ZnO NRs followed by drying in air. The thickness of the PMMA layer was controlled so that the space between the NRs is homogeneously filled while there is only very thin coverage of PMMA on the top of the NRs.

To further reduce the insulator coverage and improve the Au-ZnO contact, the PMMA was thinned by O_2 plasma etching at a pressure of 10 Pa, where the DC voltage and treatment time were 1.5 kV and 10-15 s, respectively. Then the top surface of exposed ZnO tips and PMMA was patterned with a thin layer of Au (20-30 nm), which was
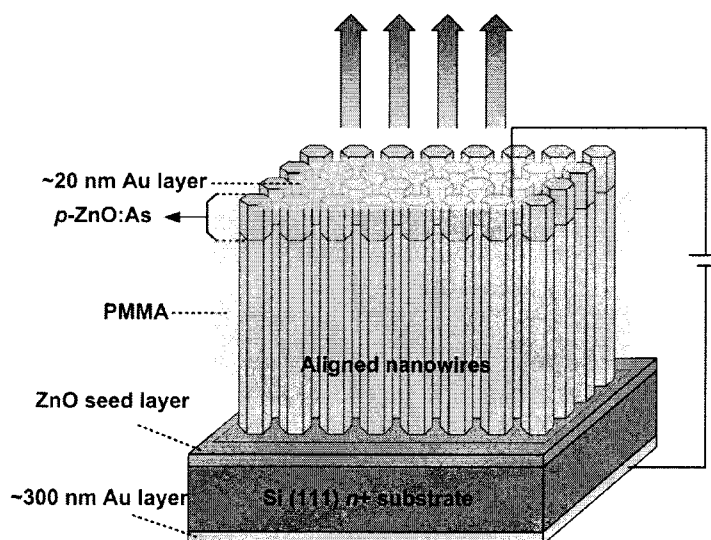
Figure 8.1 Schematic illustration of the p-ZnO:As/n-ZnO NR homojunction device on Si substrate.

sputtered on the top of the PMMA film, serving as the anode contact (Figure 8.1). There is no further coating of other materials to minimize the absorption of the emitted light from the device by this top metal layer.

8.3 Results and discussion

8.3.1 *I-V* characteristics of single nanorod after As-doping

The as-annealed NRs were measured in vacuum by a Zyvex KZ100 Nanoprobing and Nanomanipulator system, where the contact between tungsten probe and ZnO NR was improved by sputtering a thin layer of Au onto the probe. Figure 8.2 (a) shows typical current versus voltage (*I-V*) characteristics of the single vertically aligned NR p-ZnO:As/n-ZnO homojunctions, where the top layers of intrinsic NRs were doped by 180 keV As^{+} ions with the ion dose of 10^{15} cm^{-2} (Curves a and b recorded from different NRs). For comparison, Curve c is the *I-V* characteristics of n-ZnO/n-ZnO, and Curve d is that of a single n-ZnO NR/n-ZnO seed layer/n^{+}-Si heterojunction, both measured from an undoped reference sample. The schematic diagram of the measurement is shown as inset at top left. Figure 8.2 (b) shows the semi-log plots of Curves a and b to clearly resolve both forward (F) and reverse (R) currents. It can be seen that the *I-V* characteristics of single As-doped ZnO NR (curve a and b) show apparent electrical rectifying behavior that is consistent with the formation of a typical p-n junction. The forward current is around two orders higher than the reverse current in the low bias voltage range, with the reverse saturation current in the range of 5-100 nA. The forward turn-on voltage of both Curves a
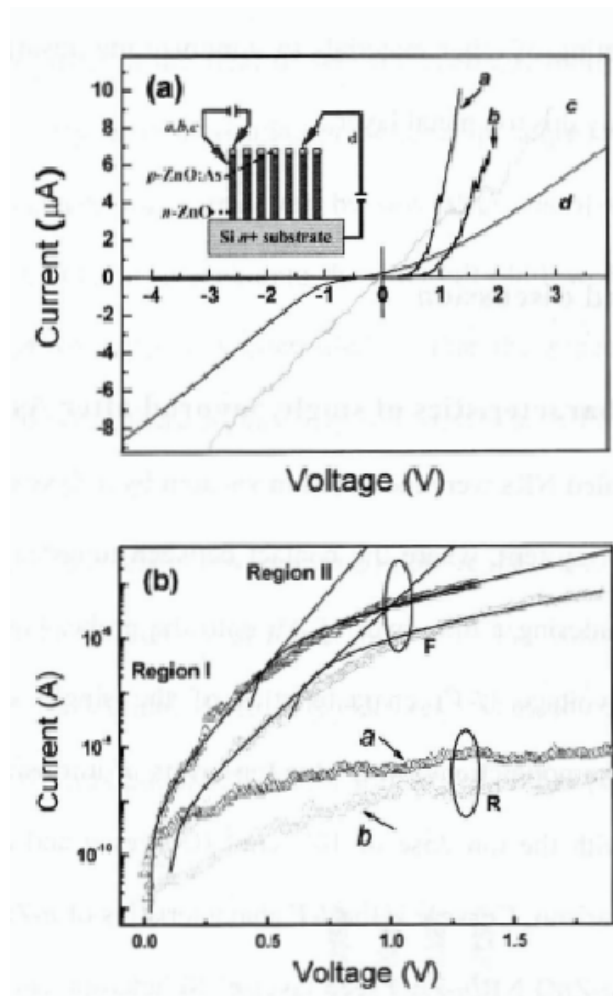
Figure 8.2 (a) Current-voltage characteristics of the single NR probed by a Zyvex nanomanipulator at room temperature, where positive voltage corresponds to the probe at the tip of the NRs. All the tungsten tips were coated by a thin Au film to improve the contact. Curve a and b were measured from the ZnO NR implanted with 180 keV As$^+$ ions with a dose of 10^{15} cm^{-2}. Curve c corresponds to the undoped ZnO NR. Curve d was measured from the undoped NR tip to the n^+-type Si substrate by probing the positive probe on tip of the NR. The inset shows their schematic diagram. (b) Semi-log plot of curves a and b. F denotes forward bias, and R denotes reverse bias.

and b occurs at ~1 V. This single NR I-V characteristic is in agreement with that reported previously for a p-ZnO/n-ZnO film homojunction diode, in which the turn-on voltage commonly appears in the range from 1-3 V.[111] This is remarkably low compared with other wide band-gap materials such as GaN and ZnSe, and even smaller than the direct band-gap energy of ZnO, which could be attributed to the deep-level doping of ZnO. Compared with diffusion doping, which can introduce very high concentrations of dopants into the semiconductor forming linearly graded junction, the ion implantation is able to control dopant dosage into specific region with high precision, forming a more abrupt junction. The I-V characteristics can be expressed by a junction rectifying model, based on the assumption of abrupt junction at the p-n interface:

$$I=I_0\,[\exp(V/nV_t)\text{-}1], \qquad\qquad (8.1)$$

where I_0 is the reverse saturation current, V is the forward-biased voltage, n is the ideality factor, V_t $=kT/e$ is the thermal voltage. When the I-V curve is dominated by an ideal diffusion current, $n=1$; whereas when the I-V curve is dominated by a recombination current, $n=2$. Usually, both mechanisms are at play, and n has a value between 1 and 2. Both semi-log plots of I versus V show two regions in the positive voltage region, as shown in Figure 8.2 (b). The ideality factors n derived from Curve a are 3.9 and 22 for Region I (i.e., V<0.6 V) and Region II (i.e., 0.6<V<1.3V), respectively. The ideality factors n derived from Curve b show small variation from Curve a, which are 3.0 and 16.6 for Region I (i.e., V<0.5 V) and Region II (i.e., 0.5<V<1.8V), respectively. The reverse saturation current I_0 is ~10^{-10} A and 10^{-7} A calculated from Equation 8.1, for Region I and II, respectively. The ideality factor obtained is similar to those observed for bulk ZnO p-n homojunctions reported elsewhere, such as 4.3 for p-ZnO:(N,Al)/n-ZnO:Al, 3-25 for p-

ZnO:As/n-ZnO homojunctions.[111, 117] The derivation from the ideal case (n =1) would be attributed to the rectification in Au/ZnO NR contact (Schottky diode), deep-level-assisted tunneling or parasitic rectifying junctions within the diode[111] and imperfections in forming the abrupt p-n junction by ion implantation.

8.3.2 Morphology of PMMA coated NR sample

Figure 8.3 (a) and (b) show the top- and side-view SEM images of the ZnO NR arrays embedded in the PMMA layer, respectively. Inset shows a higher-magnification SEM image with the sample tilted by 20° for a better view. The synthesis of ZnO NRs resulted in a preferential growth direction along the c-axis of ZnO normal to the substrate surface. The top- and side-view SEM images clearly revealed the general morphology of the ZnO NR arrays grown on the Si substrate, showing uniform distributions in their diameters and lengths. The tip of the NR is flat and hexagonally faceted. It can be seen that the NRs are slightly thicker at top and thinner at bottom [Figure 8.3(b)]. Therefore, ion implantation into the side wall of the NRs is not likely to happen, which helps to confine the As$^+$ ions only in the tip region. A thin layer of the insulator material on the ZnO could be seen in Figure 8.3 (a), where the coating is continuously covering the NRs of different lengths.
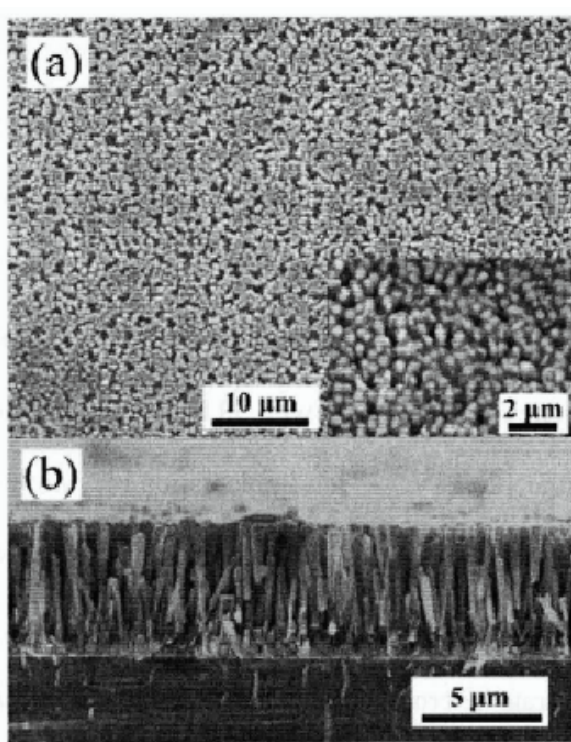
Figure 8.3 (a,b) SEM image of the top view and side view of a ZnO NR sample

coated with thin PMMA film, respectively. Inset in (a) shows the higher-

magnification SEM image of the PMMA film coated NRs tilted by 20 °.

8.3.3 *I-V* characteristics of the devices

Figure 8.4 (a) shows the *I-V* characteristics obtained by sweeping from -10V to 10V

measured by a probe station of the NR-based LED device (Au/*p*-ZnO/*n*-ZnO/*n*-ZnO

film/*n*$^+$-Si/Au, Figure 8.1). All currents are normalized to an area of 1 cm^2. The *I-V*

characteristics of the devices implanted with 50 keV and 180 keV 10^{15} cm^{-2} As$^+$ ions are

indicated by curves *A* and *B*, respectively. The inset shows the *I-V* characteristics of *n*-

ZnO/*n*$^+$-Si substrate heterojunction. Both the curves show an acceptable rectification

behavior, which is similar to the *I-V* characteristics of single NRs shown in Figure 8.2,

probed by nanomanipulator, and the results are reproducible. The turn-on voltages are 2.88 and 0.79 V at a current of 1 mA/cm^2, and the working currents are 3.19, and 49.0 mA/cm^2 at 5V forward bias for Curves *A* and *B*, respectively. It is obvious that the ion energy affects the rectification behavior as a lower reverse breakdown voltage and a lower forward turn-on voltage could be observed for devices implanted with higher ion energy. Compared with devices implanted with 50 keV As$^+$ ions, the lattice damage of the devices introduced by the 180 keV As$^+$ ion implantation may not be fully recovered after thermal annealing, and therefore deep-level-assisted tunneling or other possible leakage current may flow through the junction under reverse bias voltage. It is not surprising that the *n*-ZnO/*n$^+$*-Si substrate heterojunction exhibit weak rectifying *I-V* characteristics, as shown in the inset. The current is two orders higher for 180 keV implanted sample compared to that of the 50 keV As$^+$ implanted one.

The forward biased regions of the devices are further studied by re-plotting Curves *A* and *B* in semi-log scale as shown in Figure 8.4 (b), and three different regions appears, depending on the range of the bias voltage we considered. The fitting results are summarized in Table 8.1. As can be seen in Figure 8.4 (b), for a low bias voltage (Region I), the currents of both devices increase linearly in the region, and the ideality factor of Curve *B* fitted from Equation 8.1 agrees well with that of single NRs (Curves *a* and *b*). However, the reverse saturation currents of devices are much higher than that of single NRs, which can be attributed to imperfection of the NR alignment and Au electrode that deposited on top of spin-coated PMMA. The large ideality factor of Curve *A* compared with Curve *B* indicates derivation from ideal abrupt junction, which might be attributed to low implantation dosage. For Region II, both the *I-V* characteristics deviate far from an
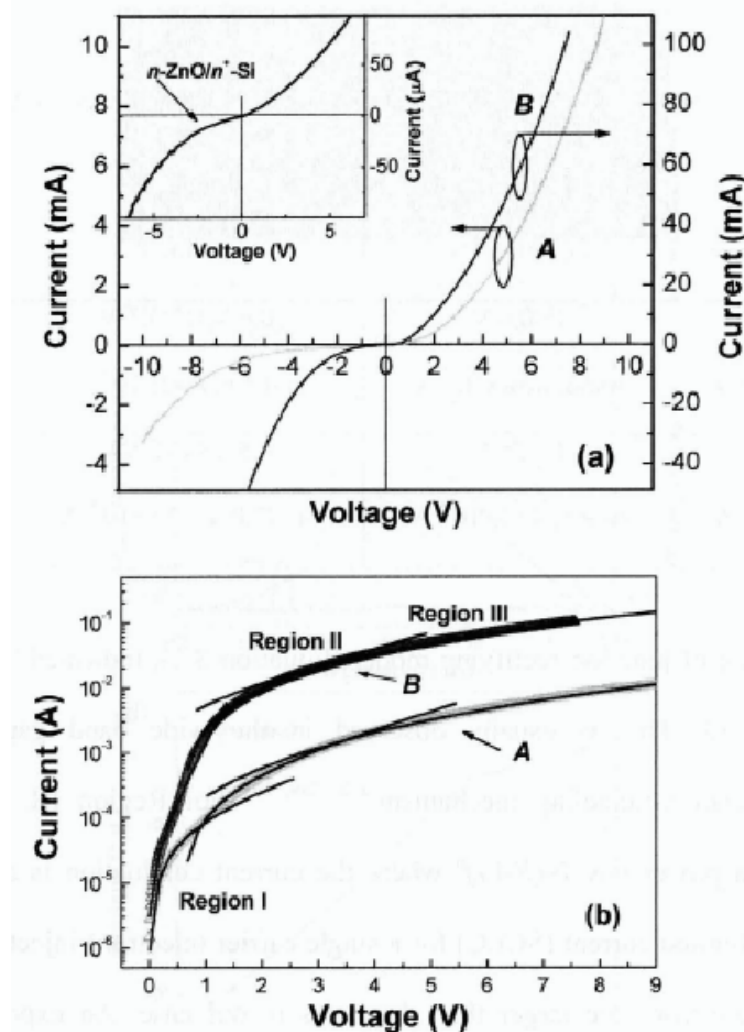
Figure 8.4 (a) Current-voltage characteristics of the devices measured by probing

station implanted with 10^{15} cm^{-2} dose of 50 and 180 keV As^{+} ions for Curves *A*

and *B*, respectively. All current are normalized to area of 1 cm^{2}. The inset shows

the current-voltage characteristics of undoped ZnO NR devices, showing a weak

rectification behavior of the *n*-ZnO/*n*$^{+}$-Si heterojunction. (b) Semi-log plots of

positive voltage regions of curves *c* and *d* shown in (a).

Table 8.1 Three region fitting results of *I-V* characteristics of Curves *c* and *d*.

I-V curve	Region I	Region II	Region III
	Equation 8.1	Equation 8.1	$I \sim (V-V_0)^\beta$
Curve A	$V<0.6$ V	0.6 V$<V<3.5$ V	$V>3.5$ V
	$n=53,\ I_0=8\times10^{-5}$ A	$n=64.6,\ I_0=2\times10^{-4}$ A	$\beta=2.4,\ V_0=-0.93$V
Curve B	$V<0.5$ V	0.5 V$<V<2.5$ V	$V>2.5$ V
	$n=9.5,\ I_0=3\times10^{-5}$ A	$n=77.0,\ I_0=7.8\times10^{-3}$ A	$\beta=2.2,\ V_0=-1.35$V

ideal case of junction rectifying model (Equation 8.1), indicated by large ideality factors around 70. This is usually observed in the wide band gap *p-n* diodes, due to recombination-tunneling mechanism.[232, 239, 243] For Region III, the *I-V* characteristics follow a power law $I \sim (V-V_0)^\beta$ where the current conduction is attributed to the space-charge-limited current (SCLC) for a single carrier (electron) injection since concentration of the electrons are larger than the holes in our case. An exponent greater than 2 is indicative of SCLC mechanism which is a normal phenomenon in the wide band gap semiconductors.[240, 241]

8.3.4 Electroluminescence spectra

As shown in Figure 8.5 (a) and (b), light emitted from both devices is significantly strong and clearly visible in ambient room light, whereas the emission cannot be measured from undoped ZnO NRs. The EL spectra of the ZnO NR homojunction diode recorded at room temperature under various forward injection currents with the ion
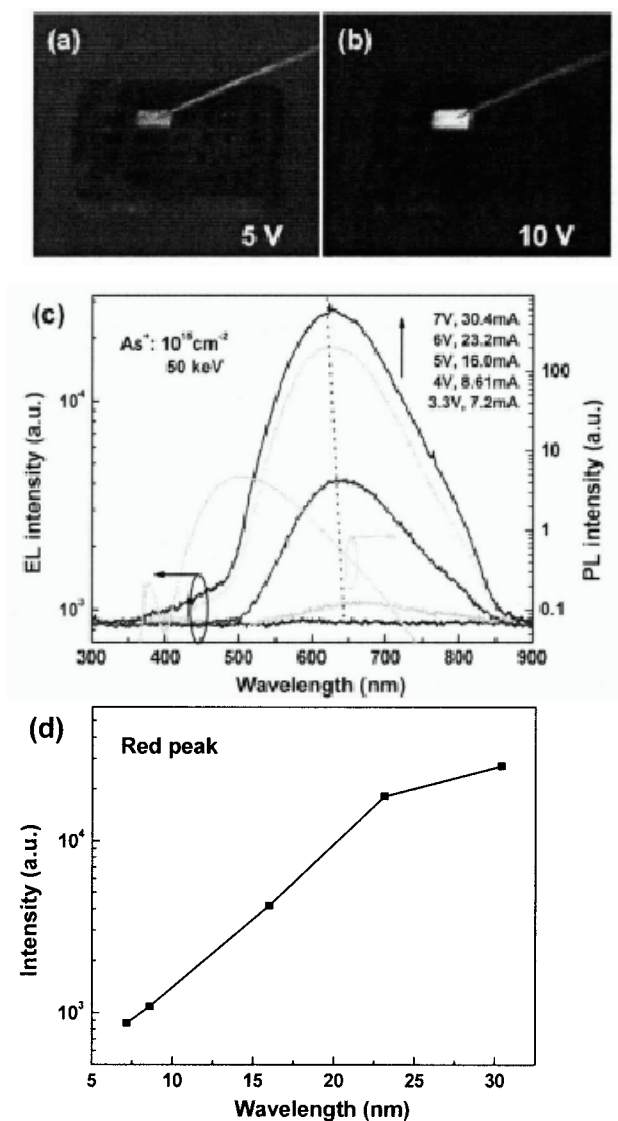
Figure 8.5 (a,b) Photos of the 50 keV, 10^{15} cm^{-2} As$^+$ doped ZnO NR homojunction devices applied with 5 and 10 V forward bias, respectively. (c) Semi-log plot of the EL spectra. The measurement was conducted in ambient air at room temperature, as a function of forward bias voltage. The spectrum was recorded with a resolution of 1 nm and each step was averaged after integration for 1 s. A typical photoluminescence spectrum of the device is also shown in (c) (right Y-axis). (d) The corresponding semi-log plot of the red peak intensity as a function of current.

116

implantation condition of 10^{15} and 50 keV are shown in Figure 8.5 (c). The peak intensities as a function of injection current are depicted in the insets. As shown in Figure 8.5 (c), the spectrum is dominated by a broad red band peaked at ~630 nm. As the applied forward bias voltage increased from 4 to 5 V, the red EL emission showed a drastic increase in its intensity. The blueshift of the emission band with the injection current (from 663 to 627 nm when current injection increased from 8.61 to 30.4 mA) suggests that the luminescence mechanism originated from the donor-acceptor pair recombination.[234] As the injected current increases, electrons and holes will occupy higher energy levels, they recombine and thus emit shorter wavelength light, which induces the blueshift of the visible band peak. A weak luminescence centered at ~390 nm could be observed for applied voltages above 5 V, which is attributed to exciton recombination in ZnO.[235] The device has a low turn-on voltage which is just above the band-gap value (3.35 eV at room temperature). As shown in the inset, the luminescence intensity of red band exponentially increases with injected current up to 6 V forward bias, indicating increased emission efficiency at higher current injection. We believe the good crystal quality of NR prepared by VPT method helps the electron injection from the intrinsic ZnO into the As-doped ZnO. The luminescence intensity approaches saturation with a 7 V forward bias. Unrecoverable device degradation is observed upon 10 V forward bias, which could be attributed to *p-n* junction breakdown and/or creation of dark current path between *i*-ZnO and the Au anode. All the as-grown ZnO NR samples, after ion implantation followed by thermal annealing, as well as PMMA coating, show similar PL spectra (Figure 8.5, right Y axis), which were excited by a 325 nm He-Cd laser. The broad green band emission peaked at ~500 nm is originated from surface defects such as oxygen

vacancies, and a weak peak at ~378 nm is originated from free exciton recombination. It is worth noting that the band shape of both green emission (PL) and red emission (EL) are quite similar. However, the redshift ~130 nm (0.5 eV) indicates the As^+ doping into the ZnO lattice, compared to the PL spectrum of ZnO. It is worth noting that there is no difference in PL spectra before and after ion implantation, because the implanted layer is rather thin and the emission under UV excitation is much weaker than that of undoped ZnO. The differences of PL and EL after ion implantation could be attributed to the different excitation mechanisms and excitation intensities. EL in our devices is more sensitive to the physical structures of the optically active layers, the electrical properties of *n*- and *p*-type conductive regions.

We should note that according to our experimental results, ZnO NRs results to be more advantageous than simple ZnO films and single crystal in forming *p-n* junctions after As^+ ion implantation. In contrast, ion implantation into ZnO films and single crystals did not result in *p-n* diodes with rectifying *I-V* characteristics, but only in a highly conductive *n*-type material. This difference could be attributed to the electronic grade purity and high crystal quality of ZnO NRs.

8.4 Summary

In summary, we have demonstrated a simple method for achieving repeatable *p-n* homojunction ZnO LEDs based on aligned ZnO NR nanostructures. Single As-implanted ZnO NR has been probed and the *I-V* results showed typical rectifying *I-V* characteristics. The exponential increase in luminescence intensity as a function of injection current indicates a high efficiency of the nanostructure-based LED devices.

Chapter 9 CONCLUSIONS AND FUTURE WORK

9.1 Conclusions

In conclusion, two new morphologies of ZnO, microraft with diamond-shaped cross section, and resistor-shaped NW composed of a pair of crystallites, have been fabricated in atmosphere.

By doping the ZnO with Cu, microrafts have been grown. Detailed XRD, SEM, and TEM characterizations show that the microrafts consist of a backbone growing along [$0\bar{1}10$] direction with side branches in parallel, which are diamond-shaped rods, growing along [0001] direction. The copper-doped microrafts show a clear ferromagnetic behavior with a high H_c and small SFD value, which may have potential applications in data storage.

By introducing trace amount of Cu and water into the growth system, RSNWs have been fabricated. Detailed SEM and TEM analysis revealed the novel resistor-shaped morphology of this kind of NWs. The "in series" connection between two NWs could be frequently observed. The RSNWs are growing along ±[0001] directions, and are composed of a pair of crystallites of wurtzite ZnO. The PL spectrum is composed of both strong UV and green emissions, which can be attributed to the high surface-to-volume ratio. The growth mechanisms for both morphologies have been explained.

Based on the controlled growth of NCBs, RNWs, and ANWs, surface modifications on these nanostructures by Ti/Ni-PIII technique with low bias voltages up to 10 kV have been studied for the first time. The ion energy dependent surface modifications on ZnO NCBs have been investigated using HRTEM and temperature-dependent PL. The results show that for NCBs, the surface-originated exciton emission could be completely quenched after 5 kV PIII, and the SX related surface states are located within 5 nm in depth from the surface corresponding to the ion implantation depth of 5 kV Ti-PIII. The UV luminescence enhancement at room temperature has been achieved. The origin of the GB luminescence has been found to be located at a depth that is morphology dependent. For both NCBs and RNWs grown with sufficient oxygen content, the depth is very small, ~0.5 nm, corresponding to the Ni ion implantation depth. However, the GB luminescence origin of ANWs grown at lower oxygen content is much deeper (~ 7 nm) with a complete quenching bias of 10 kV. Quenching of the green band can be attributed to passivation of the surface hole or electron trapping sites (oxygen vacancies) by Ni ions.

The RNWs have been successfully applied as templates to prepare ternary oxide, i.e. Zn_2TiO_4 NWs. Twinned Zn_2TiO_4 spinel NWs have been synthesized from ZnO/Ti core/shell nanostructures through a solid-state reaction of ZnO and Ti conducted at 800°. Detailed TEM analyses have revealed the nature of the ZnO/Ti core/shell structure, as well as the twinned crystalline structure of Zn_2TiO_4 spinel NWs. The Zn_2TiO_4 NWs are composed of subcrystallites about 4-50 nm in width, which are growing along $<11\bar{1}>$ direction. The formation mechanism of this twinned spinel NW has been studied.

The ANWs have been successfully applied in the fabrication of *p-n* homojunction LED devices. Stable and repeatable red EL has been observed from a simple

homojunction diode structure based on ZnO NR arrays, where the *p*-type ZnO on top of the NR was formed by As^+ ion implantation into the as-grown NRs. The *I-V* characterization of single as-grown and As-doped NRs showed linear and good rectification characteristics, respectively, confirming the formation of *p-n* homojunctions by ion implantation. The emission intensity of these LEDs increases exponentially with injected current, suggesting high efficiency of these nanostructure-based LEDs.

9.2 Recommendations for future research

9.2.1 Application of surface modified NWs in optically pumped lasing

As-shown in Chapter 5, the surface modified NWs show enhanced UV luminescence at room temperature. It is also expected that the surface modified NWs can emit UV light at higher temperature compared with un-treated NWs. Efficient lasing effect at high temperature upon optical pumping is also expected.

9.2.2 Application of doped ZnO in spintronics

Diluted magnetic semiconductors (DMS) also referred to as semimagnetic semiconductors, are alloys whose lattices are in part made up of substitutional magnetic atoms. DMS offer the possibility of studying magnetic phenomena in crystals with a simple band structure and they have excellent magneto-optical and transport properties. A key goal in this field is achieving room temperature ferromagnetism in the DMS. Recently, ZnO has been identified as a promising candidate for room temperature spintronics.[171, 172] Band structure calculations suggest that *p*-type ZnO doped with Cr, Fe,

Co, and Ni may be a transparent ferromagnetic. Our work presented in Chapter 3 also demonstrated the ferromagnetism of Cu-doped ZnO microstructures. However, the Cu dose is difficult to vary and doping may not be homogeneous into the nanostructure by a simple VPT method.

As-shown in Chapter 5 and 6, the surface modification by PIII applies only a few kV bias voltages. As the ion energy increases, ion implantation is possible for ZnO NWs, which is a precise way in controlling both ion dosage and implantation depth. It is interesting to investigate ZnO-based DMS with PIII technique in the future research works.

9.2.3 UV LEDs based on ANWs

As-shown in Chapter 8, we have demonstrated a reliable way to fabricate red LEDs based on ZnO NWs. However, reliable UV region homojunction LEDs are yet to be demonstrated. The future research in this direction will focus on fabrication and characterization of UV LEDs based on ZnO *p-n* homojunctions. It is also interesting to demonstrate lasing action of these devices.

APPENDIX I. LIST OF PUBLICATIONS

Journal papers

1. **Y. Yang**, X. W. Sun, B. K. Tay, P. H. T. Cao, J. X. Wang, X. H. Zhang, *"Revealing the surface origin of green band emission from ZnO nanostructures by plasma immersion ion implantation induced quenching,"* J. Appl. Phys. **103**, 064307, 2008.

2. **Y. Yang**, X. W. Sun, B. K. Tay, C. X. Xu, Z. L. Dong, L. Vayssieres, *"On the fabrication of resistor-shaped ZnO nanowires,"* Physica E **40**, 859, 2008.

3. **Y. Yang**, B. K. Tay, X. W. Sun, J. Y. Sze, Z. J. Han, J. X. Wang, X. H. Zhang, Y. B. Li, and S. Zhang, *"Quenching of surface-exciton emission from ZnO nanocombs by plasma immersion ion implantation,"* Appl. Phys. Lett., **91**, 071921, 2007.

4. **Y. Yang**, X. W. Sun, B. K. Tay, J. X. Wang, Z. L. Dong, and H. M. Fan, *"Twinned Zn_2TiO_4 spinel nanowires using ZnO nanowires as a template,"* Adv. Mater, **19**, 1839-1844, 2007.

5. **Y. Yang**, J. X. Wang, X. W. Sun, B. K. Tay, Z. X. Shen, and Y. Z. Zhou, *"Diamond-shaped ZnO microrafts and their optical and magnetic properties,"* Nanotechnology, **18**, 055709, 2007.

6. **Y. Yang**, X. W. Sun, B. J. Chen, C. X. Xu, T. P. Chen, C. Q. Sun, B. K. Tay, and Z. Sun, *"Refractive indices of textured indium tin oxide and zinc oxide thin films,"* Thin Solid Films, **510**, 95, 2006.

7. **Y. Yang**, B. K. Tay, X. W. Sun, H. M. Fan, and Z. X. Shen, *"Photoluminescence and growth mechanism of amorphous silica nanowires by vapor phase transport,"* Physica E, **31**, 218, 2006.

8. X. Li, C. X. Xu, G. P. Zhu, **Y. Yang**, J. P. Liu, X. W. Sun, Y. P. Cui, *"Disc-capped ZnO nanocombs,"* Chinese Phys. Lett. **24**, 3495, 2007.

9. J. X. Wang, X. W. Sun, S. S. Xie, W. Y. Zhou, **Y. Yang**, *"Single-crystal and twinned Zn_2SnO_4 nanowires with axial periodical structures,"* Cryst. Growth. Des. **8**, 707, 2008.

10. C. X. Xu, G. P. Zhu, X. Li, **Y. Yang**, S. T. Tan, X. W. Sun, C. Lincoln, T. A. Smith, *"Growth and spectral analysis of ZnO nanotubes,"* J. Appl. Phys. **103**, 094303, 2008.

11. X. B. Yan, B. K. Tay, **Y. Yang**, W. Y. Ka-Po. *"Fabrication of Three-Dimensional ZnO-Carbon Nanotube (CNT) Hybrids using Self-Assembled CNT Micropatterns as Framework,"* J. Phys. Chem. C. **111**, 17254, 2007.

12. C. Li, **Y. Yang**, X. W. Sun, W. Lei, X. B. Zhang, B. P. Wang, J. X. Wang, B. K. Tay, J. D. Ye, G. Q. Lo, and D. L. Kwong, *"Enhanced field emission from injector-like ZnO nanostructures with minimized screening effect,"* Nanotechnology, **18**, 2007.

13. J. X. Wang, X. W. Sun, S. S. Xie, **Y. Yang**, H. Y. Chen, G. Q. Lo, and D. L. Kwong, *"Preferential growth of SnO_2 triangular nanoparticles on ZnO nanobelts,"* J. Phys. Chem. C, **111**, 7671, 2007.

14. X. B. Yan, Z. J. Han, **Y. Yang**, and B. K. Tay, *"NO_2 gas sensing with polyaniline nanofibers synthesized by a facile aqueous/organic interfacial polymerization,"* Sensor. Actuat. B-Chem, **123**, 107, 2007.

Appendix I. List of Publications

15. J. P. Liu, C. X. Xu, G. P. Zhu, X. Li, Y. P. Cui, **Y. Yang**, and X. W. Sun, *"Hydrothermally grown ZnO nanorods on self-source substrate and their field emission,"* J. Phys. D: Appl. Phys., **40**, 1906, 2007.

16. G. P. Zhu, C. X. Xu, X. F. Wu, **Y. Yang**, X. W. Sun, and Y. P. Cui, *"Zinc oxide nanorods grown by arc discharge,"* J. Electron. Mater., **36**, 494, 2007.

17. X. B. Yan, Z. J. Han, and **Y. Yang**, *"Fabrication of Carbon Nanotube-Polyaniline Composites via Electrostatic Adsorption in Aqueous Colloids,"* J. Phys. Chem. C, **111**, 4125, 2007.

18. A. Wei, X. W. Sun, C. X. Xu, Z. L. Dong, **Y. Yang**, S. T. Tan, and W. Huang, *"Growth mechanism of tubular ZnO formed in aqueous solution,"* Nanotechnology, **17**, 1740, 2006.

19. J. X. Wang, X. W. Sun, **Y. Yang**, H. Huang, Y. C Lee, O. K. Tan, and L. Vayssieres, *"Hydrothermally grown oriented ZnO nanorod arrays for gas sensing applications"*, Nanotechnology, **17**, 4995, 2006.

20. X. B. Yan, B. K. Tay, and **Y. Yang**, *"Dispersing and Functionalizing Multi-walled Carbon Nanotubes in TiO$_2$ Sol,"* J. Phys. Chem. B, **110**, 25844, 2006.

21. X. W. Sun, C. X. Xu, B. J. Chen, and **Y. Yang**, *"Growth and Characterization of Misostructural Zinc Oxide Tubes"*, J. of Metastable and Nanocrystalline Materials **23**, 293 -296, 2005.

Conference papers/abstracts

1. **Y. Yang**, B. K. Tay, X. W. Sun, P. H. T. Cao, J. Y. Sze, S. T. Tan, X. H. Zhang, and H. M. Fan, *"Optical and magnetic properties of ZnO nanowire arrays modified by Ni*

ions," presented at International Conference on Materials for Advanced Technologies (ICMAT), Singapore, 1-6 July 2007.

2. **Y. Yang**, X. W. Sun, C. X. Xu, and B. K. Tay, *"ZnO nanoresistors by vapor phase transport method"*, NanoSingapore 2006: IEEE Conference on Emerging Technologies – Nanoelectronics, Singapore, 10 - 13 Jan 2006.

3. X. W. Sun, C. X. Xu, B. J. Chen, and **Y. Yang**, *"Growth and Characterization of Misostructural Zinc Oxide Tubes"*, the 2nd International Conference on Materials for Advanced Technologies (ICMAT), and the International Union of Materials Research Societies (IUMRS) – International Conference in Asia (ICA) 2003, Singapore, 7 – 12 Dec 2003.

APPENDIX II. BIBLIOGRAPHY

1   C. M. Lieber, *"One-dimensional nanostructures: Chemistry, physics & applications,"* Solid State Commun. **107**, 607 (1998).

2   J. T. Hu, T. W. Odom, C. M. Lieber, *"Chemistry and physics in one dimension: synthesis and properties of nanowires and nanotubes,"* Acc. Chem. Res. **32**, 435 (1999).

3   J. T. Devreese, R. P. Evard, V. E. van Doren, in *Highly Conducting One-dimensional Solids*, New York, **1979**.

4   E. W. Wong, P. E. Sheehan, C. M. Lieber, *"Nanobeam Mechanics: Elasticity, Strength, and Toughness of Nanorods and Nanotubes,"* Science **277**, 1971 (1997).

5   J. D. Holmes, K. P. Johnston, R. C. Doty, B. A. Korgel, *"Control of Thickness and Orientation of Solution-Grown Silicon Nanowires,"* Science **287**, 1471 (2000).

6   L. D. Hicks, M. S. Dresselhaus, *"Thermoelectric figure of merit of a one-dimensional conductor,"* Phys. Rev. B **47**, 16631 (1993).

7   Y. Y. Wu, H. Q. Yan, M. Huang, B. Messer, J. H. Song, P. D. Yang, *"Inorganic Semiconductor Nanowires: Rational Growth, Assembly and Novel Properties,"* Chem. Eur. J **8**, 1260 (2002).

8   J. X. Wang, X. W. Sun, Y. Yang, H. Huang, Y. C. Lee, O. K. Tan, L. Vayssieres, *"Hydrothermally grown oriented ZnO nanorod arrays for gas sensing applications,"* Nanotechnology **17**, 4995 (2006).

9   R. H. Baughman, A. A. Zakhidov, W. A. Hee, *"Carbon nanotubes-the route toward applications,"* Science **297**, 787 (2002).

Appendix II. Bibliography

10   T. A. Taton, *"Bio-nanotechnology: two-way traffic,"* Nature. Mater. **2**, 73 (2003).

11   M. Y. Han, X. H. Gao, J. Z. Su, S. M. Nie, *"Quantum-dot-tagged microbeads for multiplexed optical coding of biomolecules,"* Nat. Biotechnol. **19**, 631 (2001).

12   J. S. Foresi, P. R. Villeneuve, J. Ferrera, E. R. Thoen, G. Steinmeyer, S. Fan, J. D. Joannopoulos, L. C. Kimerling, H. I. Smith, E. P. Ippen, *"Photonic-bandgap microcavities in optical waveguides,"* Nature **390**, 143 (1997).

13   S. Matsui, Y. Ochiai, *"Focused Ion Beam Applications to Solid State Devices,"* Nanotechnology **7**, 247 (1996).

14   C. Vieu, F. Carcenac, A. Pepin, Y. Chen, M. Mejias, A. Lebib, L. M. Ferlazzo, L. Couraud, H. Launois, *"Electron beam lithography: resolution limits and applications,"* Appl. Surf. Sci. **164**, 111 (2000).

15   J. A. Dagata, *"Device Fabrication by Scanned Probe Oxidation,"* Science **270**, 1625 (1995).

16   S. Hong, J. Zhu, C. A. Mirkin, *"Multiple Ink Nanolithography: Toward a Multiple-Pen Nano-Plotter,"* Science **286**, 523 (1999).

17   C. M. Lieber, *"The incredible shrinking circuit - Researchers have built nanotransistors and nanowires. Now they just need to find a way to put them all together "* Sci. Am. **285**, 58 (2001).

18   J. R. Heath, P. J. Kuekes, G. S. Snider, R. S. Williams, *"A defect-tolerant computer architecture: opportunities for nanotechnology,"* Science **280**, 1716 (1998).

19   Y. N. Xia, J. A. Rogers, K. E. Paul, G. M. Whitesides, *"Unconventional methods for fabricating and patterning nanostructures,"* Chem. Rev. **99**, 1823 (1999).

20   Y. N. Xia, P. D. Yang, Y. G. Sun, Y. Y. Wu, B. Mayers, B. Gates, Y. D. Yin, F. Kim, H. Q. Yan, *"One-dimensinal Nanostructures: Synthesis, Characterization and Applications,"* Adv. Mater. **15**, 353 (2003).

21   R. S. Wagner, W. C. Ellis, *"Vapor-liquid-solid mechanism of single crystal growth,"* Appl. Phys. Lett. **4**, 89 (1964).

22   E. I. Givargizov, in *Highly Anisotropic Crystals*, D. Reidel, Dordrecht, The Netherlands, **1987**.

23   G. Z. Cao, in *Nanostructures & Nanomaterials: Synthesis, Properties & Applications*, Imperial College Press, London, **2004**, 433.

24   W. A. Tiller, in *The Science of Crystallization: Microscopic Interfacial Phenomena*, Chambridge University Press, New York, **1991**.

25   Z. R. Dai, Z. W. Pan, Z. L. Wang, *"Novel nanostructures of functional oxides synthesized by thermal evaporation,"* Adv. Funct. Mater. **13**, 9 (2003).

26   S. Vaddiraju, H. Chandrasekaran, M. K. Sunkara, *"Vapor phase synthesis of tungsten nanowires,"* J. Am. Chem. Soc. **125**, 10792 (2003).

27   Y. W. Wang, L. D. Zhang, G. W. Meng, C. H. Liang, G. Z. Wang, S. H. Sun, *"Zn nanobelts: a new quasi one-dimensional metal nanostructure,"* Chem. Commun., 2632 (2001).

28   Y.-J. Hsu, S.-Y. Lu, *"Vapor-solid growth of Sn nanowires: growth mechanism and superconductivity,"* J. Phys. Chem. B **109**, 4398 (2005).

29   C. Liu, Z. Hu, Q. Wu, X. Z. Wang, Y. Chen, H. Sang, J. M. Zhi, S. Z. Deng, M. S. Xu, *"Vapor-solid growth and chatacterization of aluminum nitride nanocones,"* J. Am. Chem. Soc. **127**, 1318 (2005).

30   X. H. Ji, S. P. Lau, S. F. Yu, H. Y. Yang, T. S. Herng, A. Sedhain, J. Y. Lin, H. X. Jiang, K. S. Teng, J. S. Chen, *"Ultraviolet photoluminescence from ferromagnetic Fe-doped AlN nanorods,"* Appl. Phys. Lett. **90**, 193118 (2007).

31   T. Xie, Y. Lin, G. S. Wu, X. Y. Yuan, Z. Jiang, C. H. Ye, G. W. Meng, L. D. Zhang, *"AlN serrated nanoribbons synthesized by chloride assisted vapor-solid route,"* Inorg. Chem. Commun. **7**, 545 (2004).

32   M. C. Johnson, C. J. Lee, E. D. Bourret-Courchesne, S. L. Konsek, S. Aloni, W. Q. Han, A. Zettl, *"Growth and morphology of 0.80 eV photoemitting indium nitride nanowires,"* Appl. Phys. Lett. **85**, 5670 (2004).

33   W. F. Liu, C. Jia, C. G. Jin, L. Z. Yao, W. L. Cai, X. G. Li, *"Growth mechanism and photoluminescence of CdS nanobelts on Si substrate,"* J. Cryst. Growth **269**, 304 (2004).

34   D. Moore, Y. Ding, Z. L. Wang, *"Hierarchical structured nanohelices of ZnS,"* Angew. Chem. Int. Ed. **45**, 5150 (2006).

35   Z. W. Wang, L. L. Daemen, Y. S. Zhao, C. S. Zha, R. T. Downs, X. D. Wang, Z. L. Wang, R. J. Hemley, *"Morphology-tuned wurtzite-type ZnS nanobelts,"* Nat. Mater. **4**, 922 (2005).

36   R. Wu, Y. Pan, G. Yang, M. Gao, L. Wu, J. Chen, R. Zhai, J. Lin, *"Twinned SiC zigzag nanoneedles,"* J. Phys. Chem. C **111**, 6233 (2007).

37   X. Y. Kong, Y. Ding, R. Yang, Z. L. Wang, *"Single-crystal nanorings formed by epitaxial self-coiling of polar nanobelts,"* Science **303**, 1348 (2004).

38   Z. L. Wang, *"Zinc oxide nanostructures: growth, properties and applications,"* J. Phys.: Condens. Matter **16**, R829 (2004).

39   U. S. Chen, Y. L. Chueh, S. H. Lai, L. J. Chou, H. C. Shih, *"Synthesis and characterization of self-catalyzed CuO nanorods on Cu/TaN/Si assembly using vacuum-arc Cu deposition and vapor-solid reaction,"* J. Vac. Sci. Technol. B **24**, 139 (2006).

40   K. H. Lee, S. W. Lee, R. R. Vanfleet, W. Sigmund, *"Amorphous silica nanowires grown by the vapor-solid mechanism,"* Chem. Phys. Lett. **376**, 498 (2003).

41   Y. L. Chueh, M. W. Lai, J. Q. Liang, L. J. Chou, Z. L. Wang, *"Systematic study of the growth of aligned arrays of a-Fe_2O_3 and Fe_3O_4 nanowires by a vapor-solid process,"* Adv. Funct. Mater. **16**, 2243 (2006).

42   J. M. Wu, H. C. Shih, W. T. Wu, Y. K. Tseng, I. C. Chen, *"Thermal evaporation growth and the luminescence property of TiO_2 nanowires,"* J. Cryst. Growth **281**, 384 (2005).

43   Y. X. Liang, S. Q. Li, L. Nie, Y. G. Wang, T. H. Wang, *"In situ synthesis of In_2O_3 nanowires with different diameters from indium film,"* Appl. Phys. Lett. **88**, 193119 (2006).

44   W. Lu, C. M. Lieber, *"Semiconductor nanowires,"* J. Phys. D: Appl. Phys. **39**, R387 (2006).

45   M. Kirkham, X. D. Wang, Z. L. Wang, R. L. Snyder, *"Solid Au nanoparticles as a catalyst for growing aligned ZnO nanowires: a new understanding of the vapour-liquid-solid process,"* Nanotechnology **18**, 365304 (2007).

46   J. G. Lu, P. C. Chang, Z. Y. Fan, *"Quasi-one-dimensional metal oxide materials - Synthesis, properties and applications,"* Mat. Sci. Eng. R **52**, 49 (2006).

47   J. Westwater, D. P. Gosain, S. Tomiya, S. Usui, H. Ruda, *"Growth of silicon nanowires via gold/silane vapor-liquid-solid reaction,"* J. vac. Sci. Technol. B **15**, 554 (1997).

48   R. Q. Zhang, Y. Lifshitz, S. T. Lee, *"Oxide-assisted growth of semiconducting nanowires,"* Adv. Mater. **15**, 635 (2003).

49   W. G. Miao, Y. Wu, H. P. Zhou, *"Morphologies and growth mechanisms of aluminium nitride whiskers,"* J. Mater. Sci. **32**, 1969 (1997).

50   J. Zhang, X. S. Peng, X. F. Wang, Y. W. Wang, L. D. Zhang, *"Micro-Raman investigation of GaN nanowires prepared by direct reaction Ga with NH3,"* Chem. Phys. Lett. **345**, 372 (2001).

51   C. C. Chen, C. C. Yeh, C. H. Chen, M. Y. Yu, H. L. Liu, J. J. Wu, K. H. Chen, L. C. Chen, J. Y. Peng, Y. F. Chen, *"Catalytic growth and characterization of gallium nitride nanowires,"* J. Am. Chem. Soc. **123**, 2791 (2001).

52   S. Vaddiraju, A. Mohite, A. Chin, M. Meyyappan, G. Sumanasekera, B. W. Alphenaar, M. K. Sunkara, *"Mechanisms of 1D crystal growth in reactive vapor transport: Indium nitride nanowires,"* Nano Lett. **5**, 1625 (2005).

53   W. S. Shi, Y. F. Zheng, N. Wang, C. S. Lee, S. T. Lee, *"Synthesis and microstructure of gallium phosphide nanowires,"* J. vac. Sci. Technol. B **19**, 1115 (2001).

54   X. F. Duan, C. M. Lieber, *"General synthesis of compound semiconductor nanowires,"* Adv. Mater. **12**, 298 (2000).

55   W. S. Shi, Y. F. Zheng, N. Wang, C. S. Lee, S. T. Lee, *"A general synthetic route to III-V compound semiconductor nanowires,"* Adv. Mater. **13**, 591 (2001).

56   T. Shimada, K. Hiruma, M. Shirai, M. Yazawa, K. Haraguchi, T. Sato, M. Matsui, T. Katsuyama, *"Size, position and direction control on GaAs and InAs nanowhisker growth,"* Superlattice. Microst. **24**, 453 (1998).

57   S. Bhunia, T. Kawamura, Y. Watanabe, S. Fujikawa, K. Tokushima, *"Metalorganic vapor-phase epitaxial growth and characterization of vertical InP nanowires,"* Appl. Phys. Lett. **83**, 3371 (2003).

58   M. Yazawa, M. Koguchi, A. Muto, K. Hiruma, *"Semiconductor Nanowhiskers,"* Adv. Mater. **5**, 577 (1993).

59   Y. Jiang, W. J. Zhang, J. S. Jie, X. M. Meng, J. A. Zapien, S. T. Lee, *"Homoepitaxial growth and lasing properties of ZnS nanowire and nanoribbon arrays,"* Adv. Mater. **18**, 1527 (2006).

60   Y. Hao, G. Meng, Z. L. Wang, C. Ye, L. Zhang, *"Periodically Twinned Nanowires and Polytypic Nanobelts of ZnS: The Role of Mass Diffusion in Vapor-Liquid-Solid Growth,"* Nano Lett. **6**, 1650 (2006).

61   H. Fu, H. Li, W. Jie, L. Yang, *"The growth and characterization of ZnSe nanoneedles by a simple chemical vapor deposition method,"* J. Cryst. Growth **289**, 440 (2006).

62   S. Kar, S. Chaudhuri, *"Shape selective growth of CdS one-dimensional nanostructures by a thermal evaporation process,"* J. Phys. Chem. B **110**, 4542 (2006).

63   R. Solanki, J. Huo, J. L. Freeouf, *"Atomic layer deposition of ZnSe/CdSe superlattice nanowires,"* Appl. Phys. Lett. **81**, 3864 (2002).

64   X. D. Wang, C. J. Summers, Z. L. Wang, *"Large-scale hexagonal-patterned growth of aligned ZnO nanorods for nano-optoelectronics and nanosensor arrays,"* Nano. Lett. **4**, 423 (2004).

65   M. C. Johnson, S. Aloni, D. E. McCready, E. D. Bourret-Courchesne, *"Controlled vapor-liquid-solid growth of indium, gallium, and tin oxide nanowires via chemical vapor transport,"* Cryst. Growth. Des. **6**, 1936 (2006).

66   J. X. Wang, X. W. Sun, S. S. Xie, Y. Yang, H. Y. Chen, G. Q. Lo, D. L. Kwong, *"Preferential growth of SnO_2 triangular nanoparticles on ZnO nanobelts,"* J. Phys. Chem. C **111**, 7671 (2007).

67   J. X. Wang, S. S. Xie, W. Zhou, *"Growth of binary oxide nanowires,"* MRS Bull **32**, 123 (2007).

68   K. Nagashima, T. Yanagida, H. Tanaka, T. Kawai, *"Control of magnesium oxide nanowire morphologies by ambient temperature,"* Appl. Phys. Lett. **90**, 233103 (2007).

69   M. Zhao, X. L. Chen, W. J. Wang, Y. J. Ma, Y. P. Xu, H. Z. Zhao, *"Self-catalyzed growth of magnesium oxide nanorods,"* Mater. Lett. **60**, 2017 (2006).

70   Z. D. Xiao, L. D. Zhang, G. W. Meng, X. K. Tian, H. B. Zeng, M. Fang, *"High-density, aligned SiO_2 nanowire arrays: microscopic imaging of the unique growth style and their ultraviolet light emission properties,"* J. Phys. Chem. B **110**, 15724 (2006).

71   Y. Yang, B. K. Tay, X. W. Sun, H. M. Fan, Z. X. Shen, *"Photoluminescence and growth mechanism of amorphous silica nanowires by vapor phase transport,"* Physica E **31**, 218 (2006).

72   J. Q. Hu, Y. Jiang, X. M. Meng, C. S. Lee, S. T. Lee, *"Temperature-dependent growth of germanium oxide and silicon oxide based nanostructures, aligned silicon oxide nanowire assemblies, and silicon oxide microtubes,"* Small **1**, 429 (2005).

73   V. Valcarcel, A. Souto, F. Guitian, *"Development of single-crystal a-Al$_2$O$_3$ fibers by vapor-liquid-solid deposition (VLS) from aluminum and powdered silica,"* Adv. Mater. **10**, 138 (1998).

74   Y. Wu, P. Yang, *"Direct Observation of Vapor-Liquid-Solid Nanowire Growth,"* J. Am. Chem. Soc. **123**, 3165 (2001).

75   S. Kodambaka, J. Tersoff, M. C. Reuter, F. M. Ross, *"Diameter-independent kinetics in the vapor-liquid-solid growth of Si nanowires,"* Phys. Rev. Lett. **96**, 096105 (2006).

76   X. Sun, B. Yu, G. Ng, T. D. Nguyen, M. Meyyappan, *"III-VI compound semiconductor indium selenide (In$_2$Se$_3$) nanowires: synthesis and characterization,"* Appl. Phys. Lett. **89**, 233121 (2006).

77   B. S. Kang, S. J. Pearton, F. Ren, *"Low temperature (< 100 degrees C) patterned growth of ZnO nanorod arrays on Si,"* Appl. Phys. Lett. **90**, 083104 (2007).

78   R. C. Furneaux, W. R. Rigby, A. P. Davidson, *"The Formation of Controlled-Porosity Membranes from Anodically Oxidized Aluminum,"* Nature **337**, 147 (1989).

79   C. Schonenberger, B. M. I. vanderZande, L. G. J. Fokkink, M. Henny, C. Schmid, M. Kruger, A. Bachtold, R. Huber, H. Birk, U. Staufer, *"Template synthesis of nanowires in porous polycarbonate membranes: Electrochemistry and morphology,"* J. Phys. Chem. B **101**, 5497 (1997).

80   K. S. Shankar, A. K. Raychaudhuri, *"Fabrication of nanowires of multicomponent oxides: Review of recent advances,"* Mat. Sci. Eng. C-Bio. S. **25**, 738 (2005).

81   M. M. M. Bilek, P. Evans, D. R. McKenzie, D. G. McCulloch, H. Zreiqat, C. R. Howlett, *"Metal ion implantation using a filtered cathodic vacuum arc,"* J. Appl. Phys. **87**, 4198 (2000).

82   J. Pelletier, A. Anders, *"Plasma-blased ion implantation and deposition: A review of physics, technology, and applications,"* IEEE T. Plasma. Sci. **33**, 1944 (2005).

83   P. K. Chu, S. Qin, C. Chan, N. W. Cheung, L. A. Larson, *"Plasma immersion ion implantation - A fledgling technique for semiconductor processing,"* Mat. Sci. Eng. R **17**, 207 (1996).

84   J. R. Conrad, *"Plasma Source Ion-Implantation - a New Approach to Ion-Beam Modification of Materials,"* Mater. Sci. Eng. A **116**, 197 (1989).

85   X. Y. Liu, X. B. Zhao, R. K. Y. Fu, J. P. Y. Ho, C. X. Ding, P. K. Chu, *"Plasma-treated nanostructured TiO_2 surface supporting biomimetic growth of apatite,"* Biomaterials **26**, 6143 (2005).

86   C. M. Chen, in *Polymer Surface Modification and Characterization*, Hanser Gardner, Cincinnati, **1994**.

87   J. Y. Sze, B. K. Tay, C. I. Pakes, D. N. Jamieson, S. Prawer, *"Conducting Ni nanoparticles in an ion-modified polymer,"* J. Appl. Phys. **98**, 066101 (2005).

88   Z. L. Wang, X. Y. Kong, Y. Ding, P. X. Gao, W. L. Hughes, R. Yang, Y. Zhang, *"Semiconducting and piezoelectric oxide nanostructures induced by polar surfaces,"* Adv. Funct. Mater. **14**, 943 (2004).

89   C. J. Lee, T. J. Lee, S. C. Lyu, Y. Zhang, H. Ruh, H. J. Lee, *"Field emission from well-aligned zinc oxide nanowires grown at low temperature,"* Appl. Phys. Lett. **81**, 3648 (2002).

90   C. X. Xu, X. W. Sun, *"Field emission from zinc oxide nanopins,"* Appl. Phys. Lett. **83**, 3806 (2003).

91   U. Ozgur, Y. I. Alivov, C. Liu, A. Teke, M. A. Reshchikov, S. Dogan, V. Avrutin, S. J. Cho, H. Morkoc, *"A comprehensive review of ZnO materials and devices,"* J. Appl. Phys. **98**, 041301 (2005).

92   Q. H. Li, Q. Wan, Y. X. Liang, T. H. Wang, *"Electronic transport through individual ZnO nanowires,"* Appl. Phys. Lett. **84**, 4556 (2004).

93   M. H. Huang, S. Mao, H. Feick, H. Q. Yan, Y. Y. Wu, H. Kind, E. Weber, R. Russo, P. D. Yang, *"Room-temperature ultraviolet nanowire nanolasers,"* Science **292**, 1897 (2001).

94   C. X. Xu, X. W. Sun, C. Yuen, B. J. Chen, S. F. Yu, Z. L. Dong, *"Ultraviolet amplified spontaneous emission from self-organized network of zinc oxide nanofibers,"* Appl. Phys. Lett. **86**, 011118 (2005).

95   S. P. Lau, H. Y. Yang, S. F. Yu, H. D. Li, M. Tanemura, T. Okita, H. Hatano, H. H. Hng, *"Laser action in ZnO nanoneedles selectively grown on silicon and plastic substrate,"* Appl. Phys. Lett. **87**, 013104 (2005).

96   N. B. Chen, C. H. Sui, *"Recent progress in research on $MgxZn_{1-x}O$ alloys,"* Mat. Sci. Eng. B-Solid **126**, 16 (2006).

97   T. Makino, Y. Segawa, M. Kawasaki, A. Ohtomo, R. Shiroki, K. Tamura, T. Yasuda, H. Koinuma, *"Band gap engineering based on MgxZn$_{1-x}$O and CdyZn$_{1-y}$O ternary alloy films,"* Appl. Phys. Lett. **78**, 1237 (2001).

98   S. V. Bhat, F. L. Deepak, *"Tuning the bandgap of ZnO by substitution with Mn^{2+}, Co^{2+} and Ni^{2+},"* Solid State Commun. **135**, 345 (2005).

99   R. Janisch, P. Gopal, N. A. Spaldin, *"Transition metal-doped TiO$_2$ and ZnO - present status of the field,"* J. Phys.: Condens. Matter **17**, R657 (2005).

100   J. X. Wang, X. W. Sun, A. Wei, Y. Lei, X. P. Cai, C. M. Li, Z. L. Dong, *"Zinc oxide nanocomb biosensor for glucose detection,"* Appl. Phys. Lett. **88**, 233106 (2006).

101   C. Klingshirn, *"ZnO: Material, physics and applications,"* ChemPhysChem **8**, 782 (2007).

102   T. Nann, J. Schneider, *"Origin of permanent electric dipole moments in wurtzite nanocrystals,"* Chem. Phys. Lett. **384**, 150 (2004).

103   P. N. Keating, *"First- and second-order dipole moments of homopolar crystals,"* Phys. Rev. **140**, A369 (1965).

104   K. Vanheusden, W. L. Warren, C. H. Seager, D. R. Tallant, J. A. Voigt, B. E. Gnade, *"Mechanisms behind green photoluminescence in ZnO phosphor powders,"* J. Appl. Phys. **79**, 7983 (1996).

105   S. J. Pearton, D. P. Norton, K. Ip, Y. W. Heo, Y. Steiner, *"Recent progress in processing and properties of ZnO,"* Prog. Mater. Sci. **50**, 293 (2005).

106   Z. Y. Zhang, C. H. Jin, X. L. Liang, Q. Chen, L. M. Peng, *"Current-voltage characteristics and parameter retrieval of semiconducting nanowires,"* Appl. Phys. Lett. **88**, 073102 (2006).

107   A. Wood, M. Giersig, M. Hilgendorff, A. Vilas-Campos, L. M. Liz-Marzan, P. Mulvaney, *"Size effects in ZnO: The cluster to quantum dot transition,"* Aust. J. Chem. **56**, 1051 (2003).

108   M. Goppert, F. Gehbauer, M. Hetterich, J. Munzel, D. Queck, C. Klingshirn, *"Infrared-optical properties of undoped and gallium doped ZnO,"* J. Lumin. **72-4**, 430 (1997).

109   M. Joseph, H. Tabata, T. Kawai, *"p-type electrical conduction in ZnO thin films by Ga and N codoping,"* Jpn. J. Appl. Phys. **38**, L1205 (1999).

110   T. Yamamoto, H. Katayama-Yoshida, *"Solution using a codoping method to unipolarity for the fabrication of p-type ZnO,"* Jpn. J. Appl. Phys. **38**, L166 (1999).

111   J. G. Lu, Z. Z. Ye, G. D. Yuan, Y. J. Zeng, F. Zhuge, L. P. Zhu, B. H. Zhao, S. B. Zhang, *"Electrical characterization of ZnO-based homojunctions,"* Appl. Phys. Lett. **89**, 053501 (2006).

112   A. Tsukazaki, A. Ohtomo, T. Onuma, M. Ohtani, T. Makino, M. Sumiya, K. Ohtani, S. F. Chichibu, S. Fuke, Y. Segawa, H. Ohno, H. Koinuma, M. Kawasaki, *"Repeated temperature modulation epitaxy for p-type doping and light-emitting diode based on ZnO,"* Nature. Mater. **4**, 42 (2005).

113   U. Wahl, E. Rita, J. G. Correia, A. C. Marques, E. Alves, J. C. Soares, *"Direct evidence for As as a Zn-site impurity in ZnO,"* Phys. Rev. Lett. **95**, 215503 (2005).

114   S. Limpijumnong, S. B. Zhang, S. H. Wei, C. H. Park, *"Doping by large-size-mismatched impurities: The microscopic origin of arsenic- or antimony-doped p-type zinc oxide,"* Phys. Rev. Lett. **92**, 155504 (2004).

Appendix II. Bibliography

115   C. Yuen, S. F. Yu, E. S. P. Leong, S. P. Lau, K. Pita, H. Y. Yang, T. P. Chen, *"Room temperature deposition of p-type arsenic doped ZnO polycrystalline films by laser-assist filtered cathodic vacuum arc technique,"* J. Appl. Phys. **101**, 094905 (2007).

116   W.-J. Lee, J. Kang, K. J. Chang, *"Defect properties and p-type doping efficiency in phosphorus-doped ZnO,"* Phys. Rev. B **73**, 024117 (2006).

117   Y. R. Ryu, T. S. Lee, J. H. Leem, H. W. White, *"Fabrication of homostructural ZnO p-n junctions and ohmic contacts to arsenic-doped p-type ZnO,"* Appl. Phys. Lett. **83**, 4032 (2003).

118   A. Allenic, W. Guo, Y. Chen, M. B. Katz, G. Zhao, Y. Che, Z. Hu, B. Liu, S. B. Zhang, X. Pan, *"Amphoteric Phosphorus Doping for Stable p-Type ZnO,"* Adv. Mater. **19**, 3333 (2007).

119   L. K. Van Vugt, S. Ruhle, D. Vanmaekelbergh, *"Phase-correlated nondirectional laser emission from the end facets of a ZnO nanowire,"* Nano Lett. **6**, 2707 (2006).

120   T. S. Jeong, M. S. Han, C. J. Youn, Y. S. Park, *"Raman scattering and photoluminescence of As ion-implanted ZnO single crystal,"* J. Appl. Phys. **96**, 175 (2004).

121   D. J. Sirbuly, M. Law, H. Q. Yan, P. D. Yang, *"Semiconductor nanowires for subwavelength photonics integration,"* J. Phys. Chem. B **109**, 15190 (2005).

122   R. L. Hoffman, B. J. Norris, J. F. Wager, *"ZnO-based transparent thin-film transistors,"* Appl. Phys. Lett. **82**, 733 (2003).

123   A. Teke, U. Ozgur, S. Dogan, X. Gu, H. Morkoc, B. Nemeth, J. Nause, H. O. Everitt, *"Excitonic fine structure and recombination dynamics in single-crystalline ZnO,"* Phys. Rev. B **70**, 195207 (2004).

124   A. P. Roth, J. B. Webb, D. F. Williams, *"Band-Gap Narrowing in Heavily Defect-Doped ZnO,"* Phys. Rev. B **25**, 7836 (1982).

125   P. D. Yang, H. Q. Yan, S. Mao, R. Russo, J. Johnson, R. Saykally, N. Morris, J. Pham, R. R. He, H. J. Choi, *"Controlled growth of ZnO nanowires and their optical properties,"* Adv. Funct. Mater. **12**, 323 (2002).

126   J. Grabowska, A. Meaney, K. K. Nanda, J. P. Mosnier, M. O. Henry, J. R. Duclere, E. McGlynn, *"Surface excitonic emission and quenching effects in ZnO nanowire/nanowall systems: Limiting effects on device potential,"* Phys. Rev. B **71**, 115439 (2005).

127   M. H. Huang, Y. Y. Wu, H. Feick, N. Tran, E. Weber, P. D. Yang, *"Catalytic growth of zinc oxide nanowires by vapor transport,"* Adv. Mater. **13**, 113 (2001).

128   N. E. Hsu, W. K. Hung, Y. F. Chen, *"Origin of defect emission identified by polarized luminescence from aligned ZnO nanorods,"* J. Appl. Phys. **96**, 4671 (2004).

129   K. Vanheusden, C. H. Seager, W. L. Warren, D. R. Tallant, J. A. Voigt, *"Correlation between photoluminescence and oxygen vacancies in ZnO phosphors,"* Appl. Phys. Lett. **68**, 403 (1996).

130   S. L. Shi, G. Q. Li, S. J. Xu, Y. Zhao, G. H. Chen, *"Green luminescence band in ZnO: Fine structures, electron-phonon coupling, and temperature effect,"* J. Phys. Chem. B **110**, 10475 (2006).

131   S. C. Lyn, Y. Zhang, H. Ruh, H. J. Lee, H. W. Shim, E. K. Suh, C. J. Lee, *"Low temperature growth and photoluminescence of well-aligned zinc oxide nanowires,"* Chem. Phys. Lett. **2002**, 134 (2002).

132   B. L. Gao, Y. Xiong, S. J. Xiong, *"Collective mode and peak splitting in phonon sidebands from interaction of degenerate exciton states with longitudinal optical phonons,"* Phys. Rev. B **74**, 235102 (2006).

133   I. Shalish, H. Temkin, V. Narayanamurti, *"Size-dependent surface luminescence in ZnO nanowires,"* Phys. Rev. B **69**, 245401 (2004).

134   A. van Dijken, E. A. Meulenkamp, D. Vanmaekelbergh, A. Meijerink, *"Identification of the transition responsible for the visible emission in ZnO using quantum size effects,"* J. Lumin. **90**, 123 (2000).

135   A. van Dijken, E. A. Meulenkamp, D. Vanmaekelbergh, A. Meijerink, *"The kinetics of the radiative and nonradiative processes in nanocrystalline ZnO particles upon photoexcitation,"* J. Phys. Chem. B **104**, 1715 (2000).

136   C. H. Liu, J. A. Zapien, Y. Yao, X. M. Meng, C. S. Lee, S. S. Fan, Y. Lifshitz, S. T. Lee, *"High-density, ordered ultraviolet light-emitting ZnO nanowire arrays,"* Adv. Mater. **15**, 838 (2003).

137   Y. Yang, J. X. Wang, X. W. Sun, B. K. Tay, Z. X. Shen, Y. Z. Zhou, *"Diamond-shaped ZnO microrafts and their optical and magnetic properties,"* Nanotechnology **18**, 055709 (2007).

138   L. Wischmeier, T. Voss, S. Börner, W. Schade, *"Comparison of the optical properties of as-grown ensembles and single ZnO nanowires,"* Appl. Phys. A: Mater. Sci. Process. **84**, 111 (2006).

139   L. Wischmeier, T. Voss, I. Ruckmann, J. Gutowski, A. C. Mofor, A. Bakin, A. Waag, *"Dynamics of surface-excitonic emission in ZnO nanowires,"* Phys. Rev. B **74**, 195333 (2006).

140   T. Voss, C. Bekeny, L. Wischmeier, H. Gafsi, S. Borner, W. Schade, A. C. Mofor, A. Bakin, A. Waag, *"Influence of exciton-phonon coupling on the energy position of the near-band-edge photoluminescence of ZnO nanowires,"* Appl. Phys. Lett. **89**, 182107 (2006).

141   M. Ichimiya, T. Horii, T. Hirai, Y. Sawada, M. Minamiguchi, N. Ohno, M. Ashida, T. Itoh, *"Nano-scale distribution of ZnO free exciton luminescence in ZnO:Zn microcrystals and its modification under electron beam excitation,"* J. Phys.: Condens. Matter. **18**, 1967 (2006).

142   X. H. Zhang, S. J. Chua, A. M. Yong, H. D. Li, S. F. Yu, S. P. Lau, *"Exciton related stimulated emission in ZnO polycrystalline thin film deposited by filtered cathodic vacuum arc technique,"* Appl. Phys. Lett. **88**, 191112 (2006).

143   W. M. Kowk, A. B. Djurisic, Y. H. Leung, D. Li, K. H. Tam, D. L. Phillips, W. K. Chan, *"Influence of annealing on stimulated emission in ZnO nanorods,"* Appl. Phys. Lett. **89**, 183112 (2006).

144   Q. Zhao, X. Y. Xu, X. F. Song, X. Z. Zhang, D. P. Yu, C. P. Li, L. Guo, *"Enhanced field emission from ZnO nanorods via thermal annealing in oxygen,"* Appl. Phys. Lett. **88**, 033102 (2006).

145   A. B. Djurisic, Y. H. Leung, *"Optical properties of ZnO nanostructures,"* Small **2**, 944 (2006).

146   E. S. P. Leong, S. F. Yu, *"UV random lasing action in $p\text{-}SiC(4H)/i\text{-}ZnO\text{-}SiO_2$ nanocomposite/n-ZnO : Al heterojunction diodes,"* Adv. Mater. **18**, 1685 (2006).

147   H. Y. Yang, S. P. Lau, S. F. Yu, A. P. Abiyasa, M. Tanemura, T. Okita, H. Hatano, *"High-temperature random lasing in ZnO nanoneedles,"* Appl. Phys. Lett. **89**, 011103 (2006).

148   J. F. Ziegler, J. P. Biersach, U. Littmark, in *The Stopping and Ranges of Ions in Solids*, Pergamon, New York, **1985**, See also www. srim.org.

149   http://en.wikipedia.org/wiki/Scanning_electron_microscope

150   http://en.wikipedia.org/wiki/Transmission_electron_microscope

151   http://en.wikipedia.org/wiki/X-ray_photoelectron_spectroscopy

152   W. I. Park, G. C. Yi, *"Electroluminescence in n-ZnO nanorod arrays vertically grown on p-GaN,"* Adv. Mater. **16**, 87 (2004).

153   P. C. Chang, Z. Y. Fan, D. W. Wang, W. Y. Tseng, W. A. Chiou, J. Hong, J. G. Lu, *"ZnO nanowires synthesized by vapor trapping CVD method,"* Chem. Mater. **16**, 5133 (2004).

154   B. D. Yao, Y. F. Chan, N. Wang, *"Formation of ZnO nanostructures by a simple way of thermal evaporation,"* Appl. Phys. Lett. **81**, 757 (2002).

155   J. H. Park, H. J. Choi, Y. J. Choi, S. H. Sohn, J. G. Park, *"Ultrawide ZnO nanosheets,"* J. Mater. Chem. **14**, 35 (2004).

156   X. H. Zhang, S. Y. Xie, Z. Y. Jiang, X. Zhang, Z. Q. Tian, Z. X. Xie, R. B. Huang, L. S. Zhang, *"Rational design and fabrication of ZnO nanotbes from nanowire templates in a microwave plasma system,"* J. Phys. Chem. B **107**, 10114 (2003).

157   Y. J. Xing, Z. H. Xi, Z. Q. Xue, X. D. Zhang, J. H. Song, R. M. Wang, J. Xu, Y. Song, S. L. Zhang, D. P. Yu, *"Optical properties of the ZnO nanotubes synthesized via vapor phase growth,"* Appl. Phys. Lett. **81**, 1689 (2003).

158   X. H. Kong, X. M. Sun, X. L. Li, Y. D. Li, *"Catalytic growth of ZnO nanotubes,"* Mater. Chem. Phys. **82**, 997 (2003).

159   Z. W. Pan, Z. R. Dai, Z. L. Wang, *"Nanobelts of semiconducting oxides,"* Science **291**, 1947 (2001).

160   H. B. Huang, S. G. Yang, J. F. Gong, H. W. Liu, J. H. Duan, X. N. Zhao, R. Zhang, Y. L. Liu, Y. C. Liu, *"Controllable assembly of aligned ZnO nanowires/belts arrays,"* J. Phys. Chem. B **109**, 20746 (2005).

161   C. X. Xu, X. W. Sun, B. J. Chen, *"Field emission from gallium-doped zinc oxide nanofiber array,"* Appl. Phys. Lett. **84**, 1540 (2004).

162   J. Y. Lao, J. Y. Huang, D. Z. Wang, Z. F. Ren, D. Steeves, B. Kimball, W. Porter, *"ZnO nanowalls,"* Appl. Phys. A **78**, 539 (2004).

163   P. X. Gao, Z. L. Wang, *"Mesoporous polyhedral cages and shells formed by textured self-assembly of ZnO nanocrystals,"* J. Am. Chem. Soc. **125**, 11299 (2003).

164   C. X. Xu, X. W. Sun, Z. L. Dong, M. B. Yu, *"Self-organized nanocomb of ZnO fabricated by Au-catalyzed vapor-phase transport,"* J. Cryst. Growth **270**, 498 (2004).

165   W. I. Park, D. H. Kim, S. W. Jung, G. C. Yi, *"Metalorganic vapor-phase epitaxial growth of vertically well-aligned ZnO nanorods,"* Appl. Phys. Lett. **80**, 4232 (2002).

166   M. S. Mo, J. C. Yu, L. Z. Zhang, S. K. A. Li, *"Self-assembly of ZnO nanorods and nanosheets into hollow microchemispheres and microspheres,"* Adv. Mater. **17**, 756 (2005).

167   C. Baratto, G. Sberveglieri, A. Onischuk, B. Caruso, S. D. Stasio, *"Low temperature selective NO2 sensors by nanostructured fibres of ZnO,"* Sens. Actuators B **100**, 261 (2004).

145

168   M. J. Zheng, L. D. Zhang, G. H. Li, W. Z. Shen, *"Fabrication and optical properties of large-scale uniform zinc oxide nanowire arrays by one-step electrochemical deposition technique,"* Chem. Phys. Lett. **363**, 123 (2002).

169   K. Yu, Y. Zhang, L. Luo, W. Wang, Z. Zhu, J. Wang, Y. Cui, H. Ma, W. Lu, *"Growth and optical properties of quadrangular zinc oxide nanorods on copper filled porous Si,"* Appl. Phys. A **79**, 443 (2004).

170   X. D. Wang, J. H. Song, Z. L. Wang, *"Single-crystal nanocastles of ZnO,"* Chem. Phys. Lett. **424**, 86 (2006).

171   H. Ohno, *"Semiconductors - Toward Functional Spintronics,"* Science **291**, 840 (2001).

172   S. J. Pearton, W. H. Heo, M. Ivill, D. P. Norton, T. Steiner, *"Dilute magnetic semiconducting oxides,"* Semicond. Sci. Tech. **19**, R59 (2004).

173   S. J. Pearton, D. P. Norton, K. Ip, Y. W. Heo, T. Steiner, *"Recent advances in processing of ZnO,"* J. Vac. Sci. Technol. B **22**, 932 (2004).

174   C. H. Chien, S. H. Chiou, G. Y. Guo, Y. D. Yao, *"Electronic structure and magnetic moments of 3d transition metal-doped ZnO,"* J. Magn. Magn. Mater. **282**, 275 (2004).

175   T. S. Herng, S. P. Lau, S. F. Yu, H. Y. Yang, X. H. Ji, J. S. Chen, N. Yasui, H. Inaba, *"Origin of room temperature ferromagnetism in ZnO : Cu films,"* J. Appl. Phys. **99**, 086101 (2006).

176   D. B. Buchholz, R. P. H. Chang, J. H. Song, J. B. Ketterson, *"Room-temperature ferromagnetism in Cu-doped ZnO thin films,"* Appl. Phys. Lett. **87**, 082504 (2005).

Appendix II. Bibliography

177   H. J. Lee, B. S. Kim, C. R. Cho, S. Y. Jeong, *"A study of magnetic and optical properties of Cu-doped ZnO,"* Phys. Status Solidi B-Basic Res. **241**, 1533 (2004).

178   X. H. Kong, Z. L. Wang, *"Spontaneous polarization-induced nanohelixes, nanosprings, and nanorings of piezoelectric nanobelts,"* Nano. Lett. **3**, 1625 (2003).

179   T. C. Damen, S. P. S. Porto, B. Tell, *"Raman effect in zinc oxide,"* Phys. Rev. **142**, 570 (1966).

180   C. Nundesmann, N. Ashkenov, M. Schubert, D. Spemann, T. Butz, E. M. Kaidashev, M. Lorenz, M. Grundmann, *"Raman scattering in ZnO thin films doped with Fe, Sb, Al, Ga, and Li,"* Appl. Phys. Lett. **83**, 1974 (2003).

181   R. H. Callender, S. S. Sussman, M. Selders, R. K. Chang, *"Dispersion of Raman cross section in CdS and ZnO over a wide energy range,"* Phys. Rev. B **7**, 3788 (1973).

182   V. Srikant, D. R. Clarke, *"On the optical band gap of zinc oxide,"* J. Appl. Phys. **83**, 5447 (1998).

183   C. X. Xu, X. W. Sun, Z. L. Dong, M. B. Yu, T. D. My, X. H. Zhang, *"Zinc oxide nanowires and nanorods fabricated by vapour-phase transport at low temperature,"* Nanotechnology **15**, 839 (2004).

184   R. Triboulet, J. M. N'Tep, M. Barbe, P. Lemasson, I. Mora-Sero, V. Munoz, *"Some fundamentals of the vapor and solution growth of ZnSe and ZnO,"* J. Cryst. Growth **199**, 968 (1999).

185   Y. T. Tian, G. M. Meng, G. Z. Wang, F. Phillipp, S. H. Sun, L. D. Zhang, *"Step-shaped bismuth nanowires with metal-semiconductor junction characteristics,"* Nanotechnology **17**, 1041 (2006).

186   C. Ruster, T. Borzenko, C. Gould, G. Schmidt, L. W. Molenkamp, X. Liu, T. J. Wojtowicz, J. K. Furdyna, Z. G. Yu, M. E. Flatte, *"Very large magnetoresistance in lateral ferromagnetic (Ga,Mn)As wires with nanoconstrictions,"* Phys. Rev. Lett. **91**, 216602 (2003).

187   C. Papadopoulos, A. Rakitin, J. Li, A. S. Vedeneev, J. M. Xu, *"Electronic transport in Y-junction carbon nanotubes,"* Phys. Rev. Lett. **85**, 3476 (2000).

188   W. D. Zhang, *"Growth of ZnO nanowires on modified well-aligned carbon nanotube arrays,"* Nanotechnology **17**, 1036 (2006).

189   B. Meyer, *"First-principles study of the polar O-terminated ZnO surface in thermodynamic equilibrium with oxygen and hydrogen,"* Phys. Rev. B **69**, 045416 (2004).

190   R. Haugsrud, *"The influence of water vapor on the oxidation of copper at intermediate temperatures,"* J. Electrochem. Soc. **149**, B14 (2002).

191   T. Fujikawa, T. Yoshikawa, *"Hydrothermal reaction of copper and water,"* Jpn. J. Appl. Phys. **40**, 1522 (2001).

192   S. Xu, B. K. Tay, H. S. Tan, L. Zhong, Y. Q. Tu, S. R. P. Silva, W. I. Milne, *"Properties of carbon ion deposited tetrahedral amorphous carbon films as a function of ion energy,"* J. Appl. Phys. **79**, 7234 (1996).

193   C. Ronning, P. X. Gao, Y. Ding, Z. L. Wang, D. Schwen, *"Manganese-doped ZnO nanobelts for spintronics,"* Appl. Phys. Lett. **84**, 783 (2004).

194   Y. Yang, B. K. Tay, X. W. Sun, J. Y. Sze, Z. J. Han, J. X. Wang, X. H. Zhang, Y. B. Li, S. Zhang, *"Quenching of surface-exciton emission from ZnO nanocombs by plasma immersion ion implantation,"* Appl. Phys. Lett. **91**, 071921 (2007).

195   X. Liu, X. H. Wu, H. Cao, R. P. H. Chang, *"Growth mechanism and properties of ZnO nanorods synthesized by plasma-enhanced chemical vapor deposition,"* J. Appl. Phys. **95**, 3141 (2004).

196   J. H. Li, D. X. Zhao, X. Q. Meng, Z. Z. Zhang, J. Y. Zhang, D. Z. Shen, Y. M. Lu, X. W. Fan, *"Enhanced Ultraviolet Emission from ZnS-Coated ZnO Nanowires Fabricated by Self-Assembling Method "* J. Phys. Chem. B **110**, 14685 (2006).

197   J. F. Li, L. Z. Yao, C. H. Ye, C. M. Mo, W. L. Cai, Y. Zhang, L. D. Zhang, *"Photoluminescence enhancement of ZnO nanocrystallites with BN capsules,"* J. Cryst. Growth **223**, 535 (2001).

198   L. Guo, S. H. Yang, C. L. Yang, P. Yu, J. N. Wang, W. K. Ge, G. K. L. Wong, *"Highly monodisperse polymer-capped ZnO nanoparticles: Preparation and optical properties,"* Appl. Phys. Lett. **76**, 2901 (2000).

199   Q. Li, S. J. Xu, M. H. Xie, S. Y. Tong, *"A model for steady-state luminescence of localized-state ensemble,"* Europhys. Lett. **71**, 994 (2005).

200   C. S. Han, J. Jun, H. Kim, *"The depth of depletion layer and the height of energy barrier on ZnO under hydrogen,"* Appl. Surf. Sci. **175**, 567 (2001).

201   J. X. Wang, X. W. Sun, H. Huang, Y. C. Lee, O. K. Tan, M. B. Yu, G. Q. Lo, D. L. Kwong, *"A two-step hydrothermally grown ZnO microtube array for CO gas sensing,"* Appl. Phys. A **88**, 611 (2007).

202   C. C. Li, Z. F. Du, L. M. Li, H. C. Yu, Q. Wan, T. H. Wang, *"Surface-depletion controlled gas sensing of ZnO nanorods grown at room temperature,"* Appl. Phys. Lett. **91**, 032101 (2007).

203   R. R. He, M. Law, R. Fan, F. Kim, P. D. Yang, *"Functional bimorph composite nanotapes,"* Nano Lett. **2**, 1109 (2002).

204   B. O. Dabbousi, J. RodriguezViejo, F. V. Mikulec, J. R. Heine, H. Mattoussi, R. Ober, K. F. Jensen, M. G. Bawendi, *"(CdSe)ZnS core-shell quantum dots: Synthesis and characterization of a size series of highly luminescent nanocrystallites,"* J. Phys. Chem. B **101**, 9463 (1997).

205   J. S. Jie, G. Z. Wang, X. H. Han, J. P. Fang, Q. X. Yu, Y. Liao, B. Xu, Q. T. Wang, J. G. Hou, *"Growth of Ternary Oxide Nanowires by Gold-Catalyzed Vapor-Phase Evaporation,"* J. Phys. Chem. B **108**, 8249 (2004).

206   H. Y. Chen, J. X. Wang, H. C. Yu, H. X. Yang, S. S. Xie, J. Q. Li, *"Transmission electron microscopy study of pseudoperiodically twinned Zn_2SnO_4 nanowires,"* J. Phys. Chem. B **109**, 2573 (2005).

207   K. W. Chang, J. J. Wu, *"Formation of well-aligned $ZnGa_2O_4$ nanowires from Ga_2O_3/ZnO core-shell nanowires via a Ga_2O_3/$ZnGa_2O_4$ epitaxial relationship,"* J. Phys. Chem. B **109**, 13572 (2005).

208   J. X. Wang, S. S. Xie, H. J. Yuan, X. Q. Yan, D. F. Liu, Y. Gao, Z. P. Zhou, L. Song, L. F. Liu, X. W. Zhao, X. Y. Dou, W. Y. Zhou, G. Wang, *"Synthesis, structure, and photoluminescence of Zn_2SnO_4 single-crystal nanobelts and nanorings,"* Solid State Commun. **131**, 435 (2004).

209   D. L. Wang, C. M. Lieber, *"Inorganic materials - Nanocrystals branch out,"* Nat. Mater. **2**, 355 (2003).

210   M. S. Gudiksen, L. J. Lauhon, J. Wang, D. C. Smith, C. M. Lieber, *"Growth of nanowire superlattice structures for nanoscale photonics and electronics,"* Nature **415**, 617 (2002).

211   H. J. Fan, M. Knez, R. Scholz, K. Nielsch, E. Pippel, D. Hesse, U. Gosele, M. Zacharias, *"Single-crystalline MgAl2O4 spinel nanotubes using a reactive and removable MgO nanowire template,"* Nanotechnology **17**, 5157 (2006).

212   H. J. Fan, M. Knez, R. Scholz, K. Nielsch, E. Pippel, D. Hesse, M. Zacharias, U. Gosele, *"Monocrystalline spinel nanotube fabrication based on the Kirkendall effect,"* Nat. Mater. **5**, 627 (2006).

213   Y. J. Li, M. Y. Lu, C. W. Wang, K. M. Li, L. J. Chen, *"ZnGa$_2$O$_4$ nanotubes with sharp cathodoluminescence peak,"* Appl. Phys. Lett. **88**, 143102 (2006).

214   J. X. Wang, S. S. Xie, Y. Gao, X. Q. Yan, D. F. Liu, H. J. Yuan, Z. P. Zhou, L. Song, L. F. Liu, W. Y. Zhou, G. Wang, *"Growth and characterization of axially periodic Zn2SnO4 (ZTO) nanostructures,"* J. Cryst. Growth **267**, 177 (2004).

215   S. K. Manik, P. Bose, S. K. Pradhan, *"Microstructure characterization and phase transformation kinetics of ball-milled prepared nanocrystalline Zn2TiO4 by Rietveld method,"* Mater. Chem. Phys. **82**, 837 (2003).

216   Z. T. Zhang, A. J. Rondinone, J. X. Ma, J. Shen, S. Dai, *"Morphologically templated growth of aligned spinel CoFe2O4 nanorods,"* Adv. Mater. **17**, 1415 (2005).

217   D. Hesse, H. Bethge, *"Solid state reactions for the epitaxial growth of spinel films,"* J. Cryst. Growth **65**, 69 (1983).

218   Z. W. Wang, S. K. Saxena, C. S. Zha, *"In situ x-ray diffraction and Raman spectroscopy of pressure-induced phase transformation in spinel Zn2TiO4,"* Phys. Rev. B **66**, 024103 (2002).

219   Z. L. Wang, M. B. Mohamed, S. Link, M. A. El-Sayed, *"Crystallographic facets and shapes of gold nanorods of different aspect ratios,"* Surf. Sci. **440**, L809 (1999).

220   Z. R. Dai, S. Shouheng, Z. L. Wang, *"Phase transformation, coalescence, and twinning of monodisperse FePt nanocrystals,"* Nano Lett. **1**, 443 (2001).

221   G. Shen, Y. Bando, B. Liu, C. Tang, D. Golberg, *"Unconventional Zigzag Indium Phosphide Single-Crystalline and Twinned Nanowires,"* J. Phys. Chem. B **110**, 20129 (2006).

222   K. Jothimurugesan, S. K. Gangwal, *"Regeneration of zinc titanate H2S sorbents,"* Ind. Eng. Chem. Res. **37**, 1929 (1998).

223   M. Pineda, J. L. G. Fierro, J. M. Palacios, C. Cilleruelo, E. Garcia, J. V. Ibarra, *"Characterization of zinc oxide and zinc ferrite doped with Ti or Cu as sorbents for hot gas desulphurization,"* Appl. Surf. Sci. **119**, 1 (1997).

224   S. K. Manik, S. K. Pradhan, *"Preparation of nanocrystalline microwave dielectric Zn_2TiO_4 and $ZnTiO_3$ mixture and X-ray microstructure characterization by Rietveld method,"* Physica E **33**, 69 (2006).

225   A. C. Chaves, S. J. G. Lima, R. Araujo, M. Maurera, E. Longo, P. S. Pizani, L. G. P. Simoes, L. E. B. Soledade, A. G. Souza, I. M. G. dos Santos, *"Photoluminescence in disordered Zn2TiO4,"* J. Solid State Chem. **179**, 985 (2006).

Appendix II. Bibliography

226   Y. Yang, X. W. Sun, B. J. Chen, C. X. Xu, T. P. Chen, C. Q. Sun, B. K. Tay, Z. Sun, *"Refractive indices of textured indium tin oxide and zinc oxide thin films,"* Thin Solid Films **510**, 95 (2006).

227   Joint Committee on Powder Diffraction Standards (JCPDS) Card No. 80-0075.

228   JCPDS Card No. 86-0156.

229   R. C. Yu, W. K. Wang, *"Formation of Ti amorphous films deposited on liquid nitrogen-cooled substrates by ion-beam sputtering,"* Thin Solid Films **302**, 108 (1997).

230   H. K. Kim, S. H. Han, T. Y. Seong, W. K. Choi, *"Electrical and structural properties of Ti/Au ohmic contacts to n-ZnO,"* J. Electrochem. Soc. **148**, G114 (2001).

231   S. B. Chakrabortty, E. A. Starke, Jr., *"Deformation twinning of Cu$_3$Au,"* Acta Metallurgica **23**, 63 (1975).

232   M. Dutta, D. Basak, *"p-ZnO/n-Si heterojunction: Sol-gel fabrication, photoresponse properties, and transport mechanism,"* Appl. Phys. Lett. **92**, 212112 (2008).

233   Y. R. Ryu, T. S. Lee, J. A. Lubguban, H. W. White, B. J. Kim, Y. S. Park, C. J. Youn, *"Next generation of oxide photonic devices: ZnO-based ultraviolet light emitting diodes,"* Appl. Phys. Lett. **88**, 241108 (2006).

234   W. Liu, S. L. Gu, J. D. Ye, S. M. Zhu, S. M. Liu, X. Zhou, R. Zhang, Y. Shi, Y. D. Zheng, Y. Hang, C. L. Zhang, *"Blue-yellow ZnO homostructural light-emitting diode realized by metalorganic chemical vapor deposition technique,"* Appl. Phys. Lett. **88**, 092101 (2006).

235   J. M. Bao, M. A. Zimmler, F. Capasso, X. W. Wang, Z. F. Ren, *"Broadband ZnO single-nanowire light-emitting diode,"* Nano Lett. **6**, 1719 (2006).

236   R. Konenkamp, R. C. Word, M. Godinez, *"Ultraviolet electroluminescence from ZnO/polymer heterojunction light-emitting diodes,"* Nano Lett. **5**, 2005 (2005).

237   J. Zhong, H. Chen, G. Saraf, Y. Lu, C. K. Choi, J. J. Song, D. M. Mackie, H. Shen, *"Integrated ZnO nanotips on GaN light emitting diodes for enhanced emission efficiency,"* Appl. Phys. Lett. **90**, 203515 (2007).

238   M. C. Jeong, B. Y. Oh, M. H. Ham, S. W. Lee, J. M. Myoung, *"ZnO-Nanowire-Inserted GaN/ZnO heterojunction light-emitting diodes,"* Small **3**, 568 (2007).

239   J. D. Ye, S. L. Gu, S. M. Zhu, W. Liu, S. M. Liu, R. Zhang, Y. Shi, Y. D. Zheng, *"Electroluminescent and transport mechanisms of n-ZnO/p-Si heterojunctions,"* Appl. Phys. Lett. **88**, 182112 (2006).

240   R. Ghosh, D. Basak, *"Electrical and ultraviolet photoresponse properties of quasialigned ZnO nanowires/p-Si heterojunction,"* Appl. Phys. Lett. **90**, 243106 (2007).

241   Y. I. Alivov, J. E. Van Nostrand, D. C. Look, M. V. Chukichev, B. M. Ataev, *"Observation of 430 nm electroluminescence from ZnO/GaN heterojunction light-emitting diodes,"* Appl. Phys. Lett. **83**, 2943 (2003).

242   Y. M. Shen, L. Pang, Y. Fainman, M. Griswold, S. Yang, L. V. Butov, L. J. Sham, *"Photoluminescence spectral switching of single CdSe/ZnS colloidal nanocrystals in poly(methyl methacrylate),"* Phys. Rev. B **76**, 085312 (2007).

243   J. B. Fedison, T. P. Chow, H. Lu, I. B. Bhat, *"Electrical characteristics of magnesium-doped gallium nitride junction diodes,"* Appl. Phys. Lett. **72**, 2841 (1998).